國立交通大學

光電工程學系博士班

博士論文

新穎矽量子點薄膜應用於太陽能電池之開發

Development of Novel Si Quantum Dot Thin Films for Solar Cells Application

博士生：郭光揚

指導教授：李柏璁　教授

中華民國一百零二年八月

新穎矽量子點薄膜應用於太陽能電池之開發

Development of Novel Si Quantum Dot Thin Films for Solar Cells Application

研究生：**郭光揚** Student：Kuang-Yang Kuo

指導教授：**李柏璁** Advisor：Po-Tsung Lee

國立交通大學

光電工程學系博士班

博士論文

A Thesis

Submitted to Department of Photonics,

College of Electrical Engineering and Computer Science

National Chiao Tung University

in partial Fulfillment of the Requirements

for the Degree of Doctor of Philosophy

in

Electro-Optical Engineering

Aug. 2013

Hsinchu, Taiwan, Republic of China

中華民國一百零二年八月

新穎矽量子點薄膜應用於太陽能電池之開發

學生：郭光揚

指導教授：李柏璁　博士

國立交通大學光電工程學系博士班

摘　要

『溫室效應』與**『能源危機』**乃攸關未來人類生存的兩大重要議題，永續再生能源加速發展已刻不容緩，而太陽能電池(Solar Cell, SC)一直被視為極具潛力的再生能源之一。於考量電池效率、成本和壽命等關鍵因素下，矽基SC仍是最具有優勢可達到普及化的電池種類；為了達到高效率低成本(第三代SC)矽基SC，開發具有**多重能隙**的多接面元件結構以**有效減低光損耗**是不可或缺的要件。

有鑒於矽量子點的獨特光學特性，我們提出並開發**『漸變矽過多氧化矽多層膜』**與**『氧化鋅矩陣材料整合』**，期望能在保有矽量子點特性下，同時克服目前應用於SC所遭遇的**載子傳輸效益明顯受限的瓶頸**，以製作出更具應用潛力的新穎矽量子點薄膜。此篇論文首先即介紹SC的重要性和發展現況，與目前矽量子點應用於SC的優勢與挑戰，並提出我們的研究目的且簡介此研究過程中的相關製程與分析儀器。

為製作出**超高密度矽量子點薄膜**，我們捨棄傳統的[二氧化矽/矽過多氧化矽]多層膜結構，改以**『漸變矽過多氧化矽多層膜』**做為新沉積結構；實驗結果顯示，藉由週期性矽氧原子濃度差異分佈，可使矽過多原子於退火過程中自組織形成超高密度且均勻尺寸的奈米結晶矽量子點，此外，該新結構亦大幅提升矽量子點薄膜的**光吸收係數**與**電傳輸效益**，證明利用此新結構，可有效**縮短矽量子點間距**，以大幅提升矽量子點薄膜的**光伏特性**。

為形成**更佳的載子傳輸機制**，我們亦開發**『氧化鋅矩陣材料整合』**，因氧化鋅薄膜除具備**直接寬能隙半導體**特性之外，更罕見地同時擁有**高透明度**和**高可調電性**等優勢，故相當適合做為矽量子點矩陣材料並應用於SC；實驗結果指出，

針對該矽量子點埋入式氧化鋅薄膜，除在長與短波長波段皆可分別保有氧化鋅的高光穿透與高光吸收特性之外，中波長波段亦具有來自矽量子點的光吸收與光激發光特性，證實來自矽量子點貢獻的**光學次能隙形成**；此外，相較於使用傳統矽相關介電矩陣材料，該矽量子點薄膜具有更高的導電度，且其載子主要**經由氧化鋅矩陣傳輸**而非傳統的量子點間穿隧效應傳輸，此經矩陣傳輸機制將可大幅提升矽量子點薄膜的載子傳輸效益，未來亦可更提升矽量子點應用於 SC 的優勢。

因此，此篇論文中，藉由分別開發**新沉積結構**與**新矩陣材料**，我們成功製作出更具潛力且更適合整合於矽基 SC 的**新穎矽量子點薄膜**，而根據此研究成果，我們更深信未來若能成功整合此新穎矽量子點薄膜，將可有利於矽基 SC 的發展，並加速邁向**第三代 SC** 的目標。

Development of Novel Si Quantum Dot Thin Films for Solar Cells Application

Student: Kuang-Yang Kuo

Advisor：Dr. Po-Tsung Lee

Department of Photonics
National Chiao Tung University

Abstract

In order to resolve the critical issues of **"Green House Effect"** and **"Energy Crisis"** for humanity's future, the accelerated developments of renewable energies are necessary. Among all of the renewable energies, solar cells (SCs) are highly considered as the most potential one. To ponder these key factors of efficiency, cost, and lifetime, undoubtedly, the Si-based SCs have the most advantages on popularized developments in the future. However, to successfully achieve high efficiency and low cost, also called **the third generation SC**, the tandem Si-based SCs with multi-bandgap is required to efficiently reduce the mismatched photon energy loss.

Based on the unique properties of Si quantum dot (QD), we propose to develop the novel Si QD thin films by utilizing a **gradient Si-rich oxide multilayer (GSRO-ML) structure** and integrating with **ZnO matrix material** to overcome the bottlenecks of the **largely limited carrier transport efficiency** in the Si-based SCs integrating Si QDs. In the beginning of this dissertation, we talk about the importance and recent developments of SCs, and then, the advantages and challenges of SCs integrating Si QDs are discussed. After that, our motivations, fabrication process, and apparatus are also introduced in details.

To achieve **the formation of super-high density Si QD thin films**, we forsake the traditional [SiO_2/SRO]-ML structure and develop a new one, GSRO-ML. In our results, by utilizing the periodical variations in Si/O atomic concentration during

deposition, the Si QDs with super-high density and good size control can be self-assembled from the uniform aggregations of Si-rich atoms during annealing. Besides, the considerable enhancements on photovoltaic properties are also obtained by using a GSRO-ML structure due to the improved carrier transport efficiency and larger optical absorption coefficient.

To obtain **the better carrier transport path for the Si QD thin films**, we also develop a new matrix material, ZnO, because it has many desirable features, such as **wide and direct bandgap**, **high transparency**, and **highly tunable electrical properties**. In our results, though embedded with Si QDs, the optical properties of ZnO thin film can be preserved in the long- and short-wavelength ranges. In the middle-wavelength range, the significantly enhanced light absorption and the unusual PL emission peak, owing to embedding Si QDs, are observed. These results represent the **sub-bandgap formation** in ZnO thin film by utilizing Si QDs while maintaining the essential optical properties of ZnO matrix. In the electrical properties, the Si QD embedded ZnO thin film reveals the **significantly higher conductivity** than that using SiO_2 matrix material. Besides, the **carriers transport mainly via ZnO matrix**, not through Si QDs, is clearly observed. This unique transport mechanism differing from those using the traditional Si-based dielectric matrix materials has great potential on leading to the **much better carrier transport efficiency** and **electrical properties** for SC applications.

In this dissertation, we had demonstrated the proposed novel Si QD thin films, **utilizing a GSRO-ML structure** and **integrating with ZnO matrix material**, are more suitable and advantageous for the Si-based SCs integrating Si QDs. Therefore, the high-efficiency Si-based SCs integrating Si QDs can be most definitely expected using the novel Si QD thin films.

Acknowledgements

首先，要特別感謝我的指導教授-李柏璁 教授，這些年在實驗和研究上給我許多寶貴建議與發揮空間，以及在報告技巧、期刊寫作與思考邏輯各方面的諸多指導，經過這幾年的歷練後，能力著實增進不少，非常感謝李教授這些年不辭辛勞的教誨，也很慶幸自己能來到交大，來到李教授的實驗室。

在實驗執行上，感謝這幾年合作過的學弟妹們-書維、文齡、品睿、權政與佑政，因為有你們的盡心盡力，不僅讓實驗與計畫皆得以順利執行，也幫我分攤不少儀器管理上的負擔；感謝學長們-Dr.盧贊文與 Dr.張資岳在我博班期間提供許多建議與協助，以及浪人品佐於部份實驗上的支援，公務員家揚的定期刺激，拼命三郎佳裕於儀器管理上的協助；也感謝已經畢業的學弟妹們-逸華、欣育、怡先、韋德、宜恆、又瑋、鈞隆、君源、立勛、雋崴、哲堯與小朱哥等，以及實驗室充滿朝氣的生力軍-坤達、家瑞、擇恩與聖諺以及新生們，讓我在交大博士班充滿許多難忘回憶，也替我的學生生涯畫下一個非常漂亮的句點。

在研究經費上，要感謝國科會-能源國家型整合計畫(計畫編號: NSC 98-3114-E-009-004-CC2 與 NSC 99-2120-M-009-009)，以及國立交通大學的綠色能源中心與特色計畫所提供的計畫經費，讓我的博班研究工作能順利進行。

最後，我更要特別感謝我的家人，諒解我這些年來的執著，讓我在整個求學的漫漫長路上沒有過多的經濟壓力，且總是適時的關心，你們依舊是我最堅強的後盾！另外，我的好朋友們-威浤、信智、宗諭、翊翔、宇倫、廣騰、應文、文賢與若軒等等，感謝你們總是在我最需要幫助的時候，二話不說的伸出雙手雙腳，情義相挺，真的是太夠朋友了！

在此，對於這一路上曾經幫助過我的貴人們，獻上最誠摯的謝意，沒有你們，沒有今天的我！

郭光揚

2013/09/09

Table of Contents

Figure Captions

Chapter 1

Chapter 2

Chapter 3

Chapter 4

Chapter 5

Appendix

Table Captions

Chapter 3

Chapter 4

Chapter 1

Introduction of Si Quantum Dot (QD) Thin Films for Solar Cells Application

1-1 Background of Solar Cells

Recently, in order to resolve the critical issues of “Green House Effect” and “Energy Crisis” for humanity’s future, the demands on the non-renewable resources, for examples, coil, coal, and natural gas, are necessary to be largely reduced in the near-future. Hence, it’s very important to accelerate the developments on the renewable energies, such as solar cell (SC), solar thermal energy, biomass energy, wind power, and hydropower. Fig. 1-1 shows an illustration for the development of the global energy mix (~2100) predicted by German Solar Industry Association [1]. It clearly indicates the energies created by SCs will be the most important source after 2050 because of the large area and long duration of solar irradiation on the earth. Therefore, the popularized development of SCs can efficiently improve the critical issues of “Green House Effect” and “Energy Crisis” in the future.

Fig. 1-2(a) shows the predicted market shares 2015 for the main kinds of SCs by EuPD Research [2], it clearly indicates the Si-based SCs, involving the c-Si bulk and Si thin film SCs, will still occupy the highest market share for 82 % in 2015. Besides, the content of Si element in the earth’s crust is the largest material among all kinds of SCs, shown as Fig. 1-2(b) [3]. Hence, the Si-based SCs have many advantageous on the popularized development in the future. The newly-updated best research-cell efficiencies (~2013) recorded by National Renewable Energy Laboratory (NREL) are also shown in Fig. 1-3 [4], so far, the conversion efficiencies of the Si-based SC are still significantly limited by the energy loss mechanisms [5]. Therefore, to efficiently reduce the energy loss in the Si-based SCs is needed to further enhance the SCs' performances.

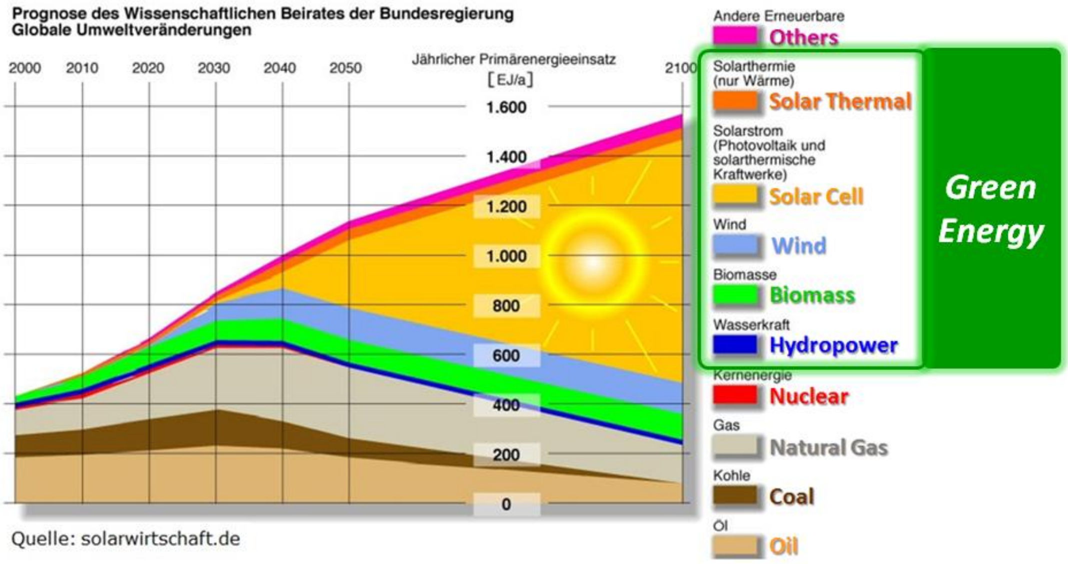

Fig. 1-1: Prediction for the development of the global energy mix (~2100). [1]

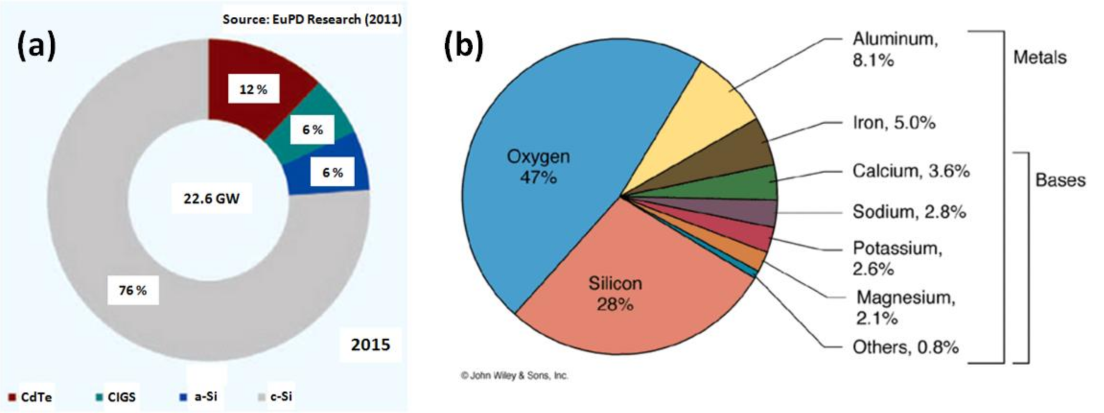

Fig. 1-2: (a) Prediction of the market shares 2015 for the main kinds of SCs. [2] (b) Composition of the main elements in the earth's crust. [3]

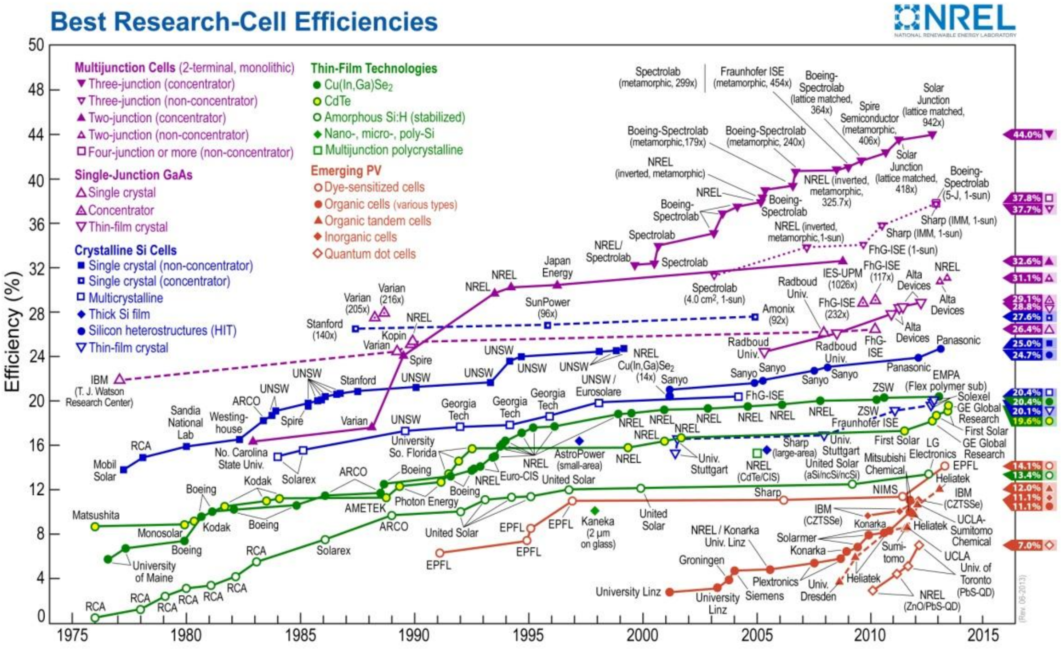

Fig. 1-3: Best research-cell efficiencies recorded by NREL (~2013). [5]

Based on efficiency and cost, the SCs can be briefly classified to three generations, shown as Fig. 1-4 [5]. The first generation SCs have the high efficiency but high cost, such as single- and poly-crystalline Si bulk SCs; and the second generation ones possess the low cost but low efficiency, such as organic and dye-sensitized (DSSC) SCs. And so far, the third generation SCs with high efficiency and low cost are still unsuccessfully developed, however, the tandem SCs with multi-bandgap are highly expected due to the great potentials on the mismatched photon energy loss improvements [5].

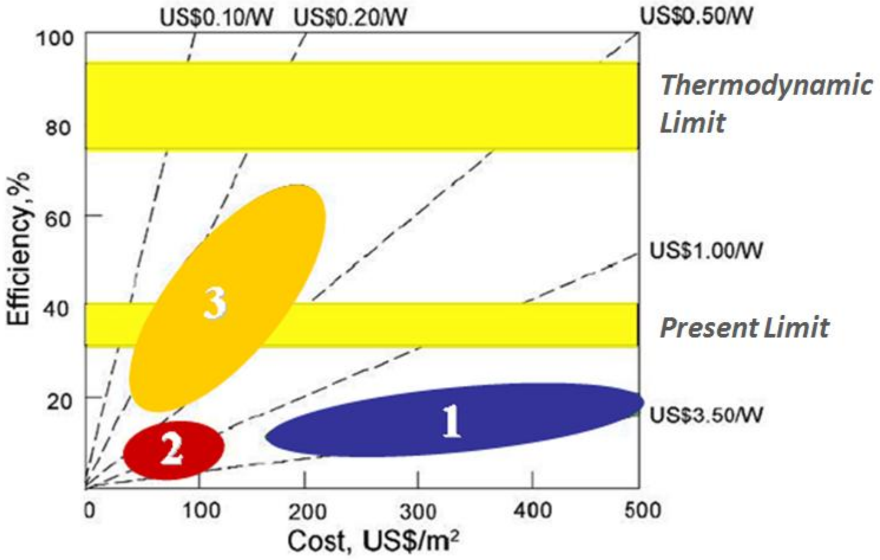

Fig. 1-4: Efficiency versus cost for three generations of SCs. [5]

1-2 Solar Cells Integrating Si QD Thin Films

1-2.1 Energy Loss Mechanisms

So far, the performances of SCs with single-bandgap are mainly limited by five kinds of energy loss mechanisms, including the over-high photon energy loss, junction loss, recombination loss, metal-semiconductor contact loss, and over-low photon energy loss [5], as shown in Fig. 1-5. The difference of photon absorption between SCs with single- and multi-bandgap is also shown in Fig. 1-6 [5]. Better than with single-bandgap, the SCs with multi-bandgap can efficiently improve the over-high and over-low photon energy losses and significantly enhance cells' performances. As the solar irradiation energies are widely distributed in a large wavelength range, shown as Fig. 1-7 [6], the mismatched photon energy loss will largely degrade the performances of SCs with single-bandgap. Hence, the SCs with multi-bandgap are more potential for the third-generation SCs development than that with single-bandgap.

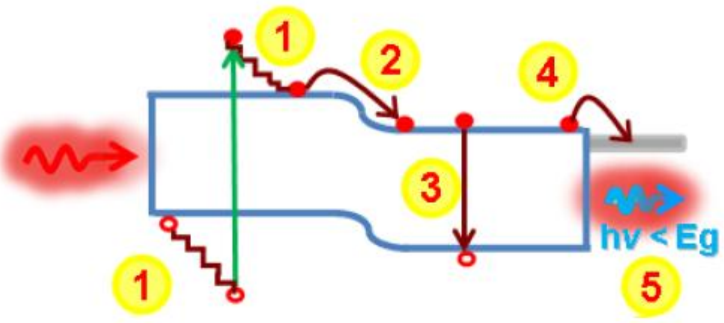

Fig. 1-5: Main energy loss mechanisms in SCs with single bandgap, including the (1) over-high photon energy loss, (2) junction loss, (3) recombination loss, (4) metal-semiconductor contact loss, and (5) over-low photon energy loss.

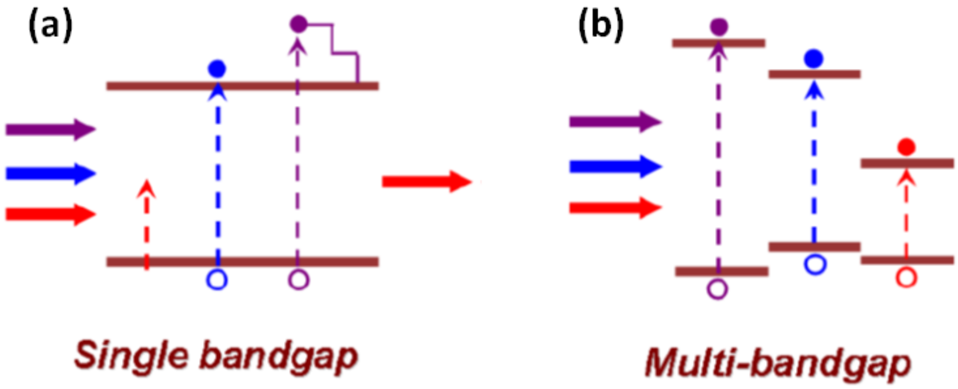

Fig. 1-6: Difference of photon absorption between SCs with (a) single- and (b)multi-bandgap.

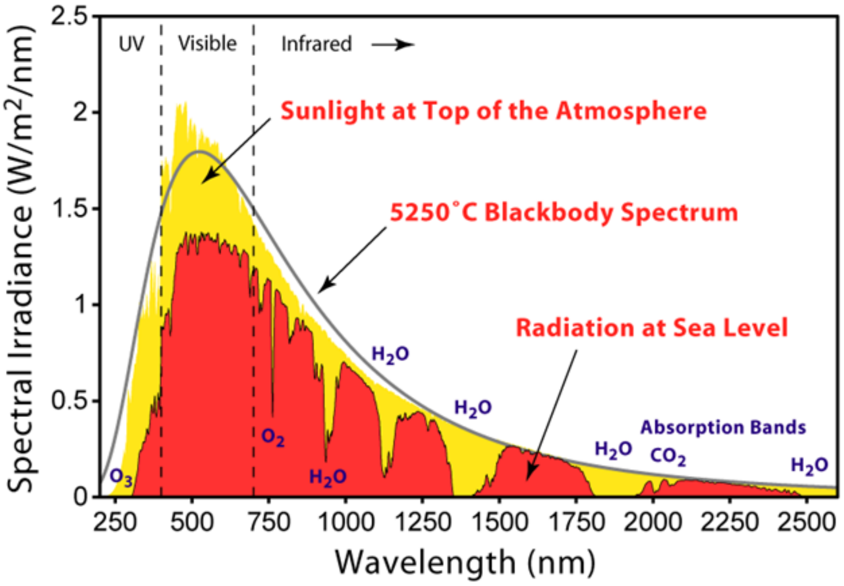

Fig. 1-7: Solar irradiance spectrum above atmosphere and at surface. [6]

1-2.2 Advantages of Using Si QD

In order to efficiently reduce the mismatched photon energy loss in the Si-based SCs, the Si QD thin films have been extensively studied owing to their many unique characteristics such as highly-tunable bandgap and better optical properties [7-9]. The Si-based dielectric materials, such as SiO_2 and Si_3N_4, are commonly used as the matrix materials due to their simple process, high transparency, and significantly larger bandgap than c-Si material [10, 11]. Fig. 1-8 shows the band diagrams of Si QDs embedded in a wide bandgap matrix material under different QD sizes. According to quantum confinement (QC) effect, the allowed energy levels in the valance and conduction bands will be discrete, and such results can make the effective bandgap of Si QDs ($E_{g,QD}$) being larger than that of c-Si ($E_{g,c\text{-}Si}$) material. So far, it had been demonstrated that the $E_{g,QD}$ can be largely tuned from near c-Si (1.1 eV) to obviously higher than a-Si (1.7 eV) materials [12, 13]. Hence, Si QDs have great potentials on bandgap engineering for the mismatched photon energy loss improvements in the Si-based SCs.

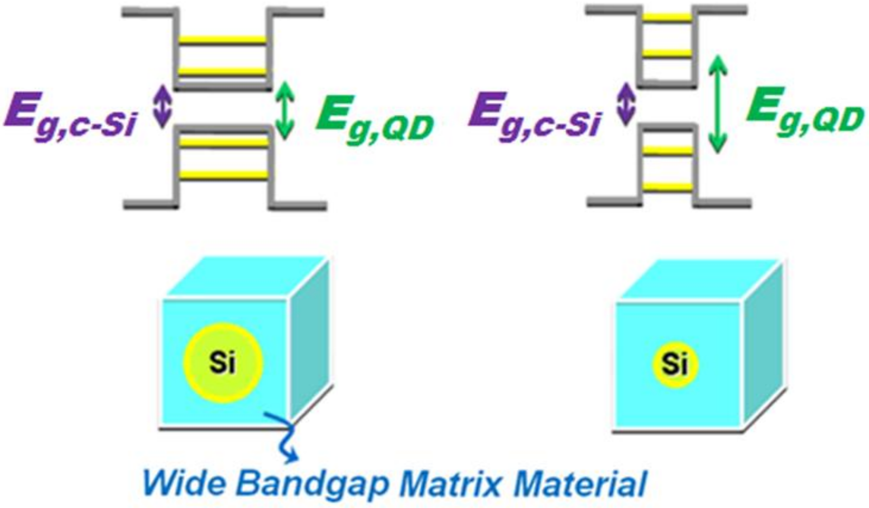

Fig. 1-8: Illustration of band diagrams for Si QDs embedded in a wide bandgap matrix material under different QD sizes.

Fig. 1-9 shows an illustration of a possible design for an all Si-based tandem SC integrating Si QDs with different QD sizes. By integrating various QD sizes, the mismatched photon energy loss can be efficiently reduced, and the cell's performance can also be significantly enhanced. Therefore, the third generation Si-based SCs with high efficiency and low cost can be highly expected by integrating Si QDs.

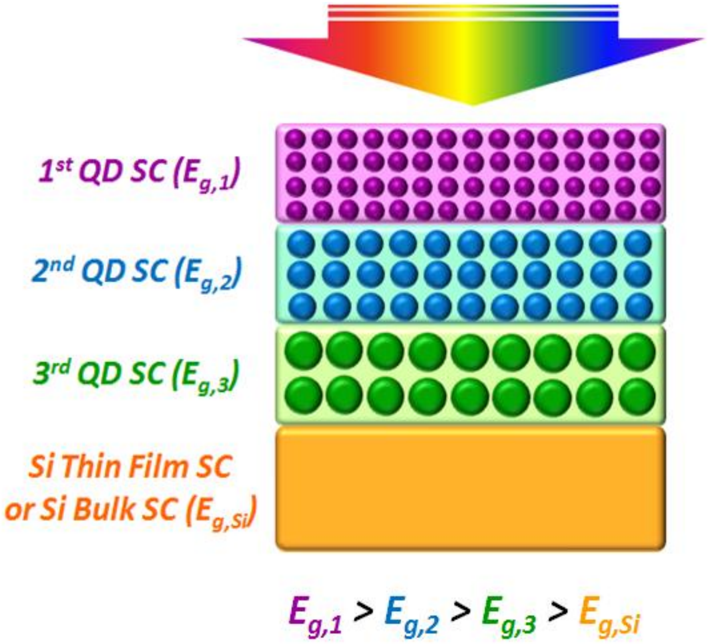

Fig. 1-9: Illustration of a possible design for an all Si-based tandem SC integrating Si QDs with different QD sizes.

1-2.3 Literatures Review

In 2006, M. A. Green at al. firstly proposes the idea of integrating Si QDs with Si-based SCs for the third generation SCs [10, 14]. They fabricate the Si QD thin films by radio-frequency (RF) co-sputtering and post-annealing methods, shown as Fig. 1-10. The Si QD embedded SiO_2 thin films are deposited by a [silicon dioxide/silicon-rich oxide] multilayer ([SiO_2/SRO]-ML) structure. During annealing, the excess Si atoms separate out and crystallize in the SRO layers, and Si QDs are formed and confined in the SRO layers. From transmission electron microscope

(TEM) images, shown as Fig. 1-11, the nano-crystalline Si QDs are clearly observed in the Si-rich nitride (SRN) layers [13]. Based on photoluminescence (PL) spectra analysis, the $E_{g,QD}$ can be obtained. The measured PL peak energies from M. A. Green's and others' results as a function of QD size are shown in Fig. 1-12 [13]. It clearly indicates the $E_{g,QD}$ can be modified even larger than that of amorphous Si material (~1.7 eV) by tuning the QD size. Hence, it demonstrates that the bandgap engineering is really a feasible idea by utilizing the Si QDs.

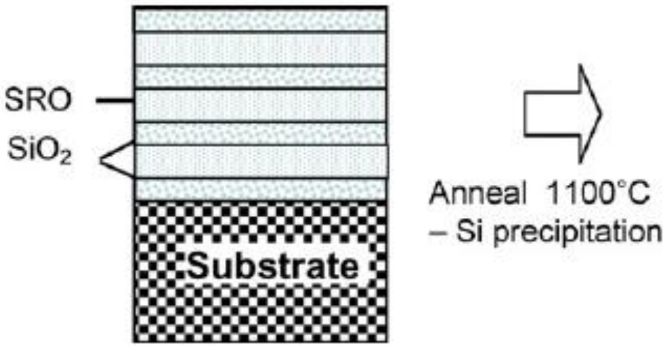

Fig. 1-10: Illustration of the fabrication process for the Si QD thin films using a [SiO_2/SRO]-ML structure**.** [13]

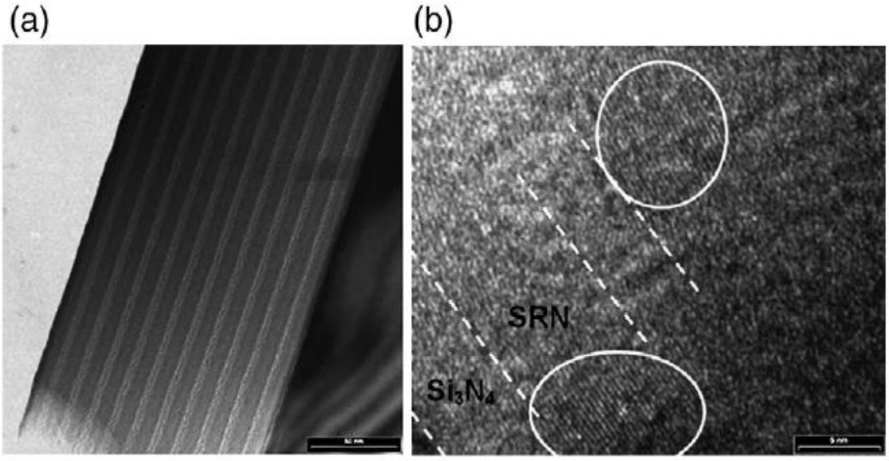

Fig. 1-11: (a) Low and (b) high magnification TEM images of the Si QD thin films using a Si_3N_4 matrix material. [13]

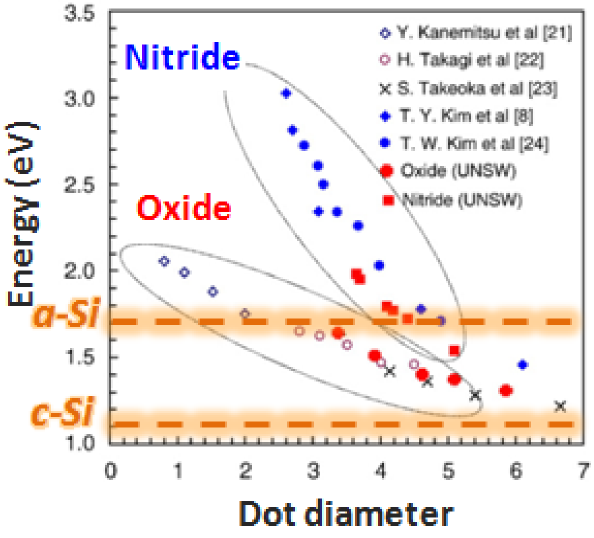

Fig. 1-12: Bandgap energy versus QD size using SiO_2 and Si_3N_4 matrix materials from different groups' works. [13]

In 2008, M. A. Green et al. also experimentally demonstrates the feasibility of SCs integrating Si QDs [15, 16]. They fabricate the n-type Si QDs embedded SiO_2 thin films on p-type c-Si wafer, as shown in Fig. 1-13. The n-type Si QD thin film is consisted of 15 or 25 bilayers of SiO_2 and P-doped (0.23 at. %) Si QDs with a SiO_2 thickness of 1 or 2 nm. The nominal diameters of the Si QDs are 3, 4, 5 and 8 nm. The SC with 3 nm of Si QDs has the highest efficiency, with open-circuit voltage (V_{oc}) of 556 mV, short-circuit current (J_{sc}) of 29.8 mA/cm^2, fill factor (F. F.) of 63.8%, and conversion efficiency of 10.6%. The internal quantum efficiency (IQE) of the fabricated SCs and corresponding absorption spectra of the Si QD thin films are shown in Fig. 1-14, the well-matched relation is clearly observed. The thicker the SRO layer, the larger the QDs' size, which results in a smaller effective bandgap. These results indicate that the conversion efficiency of the fabricated hetero-junction SCs is indeed enhanced by integrating with Si QDs.

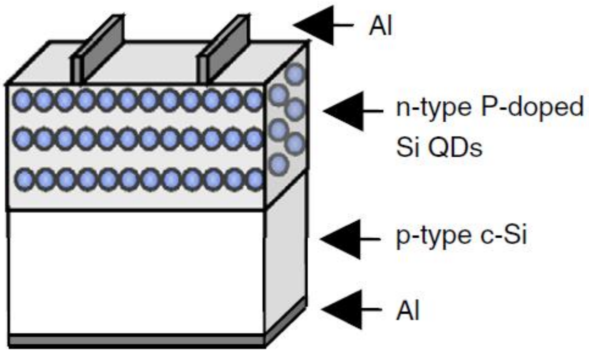

Fig. 1-13: Illustration of a n-type Si QDs/p-type c-Si SC. [16]

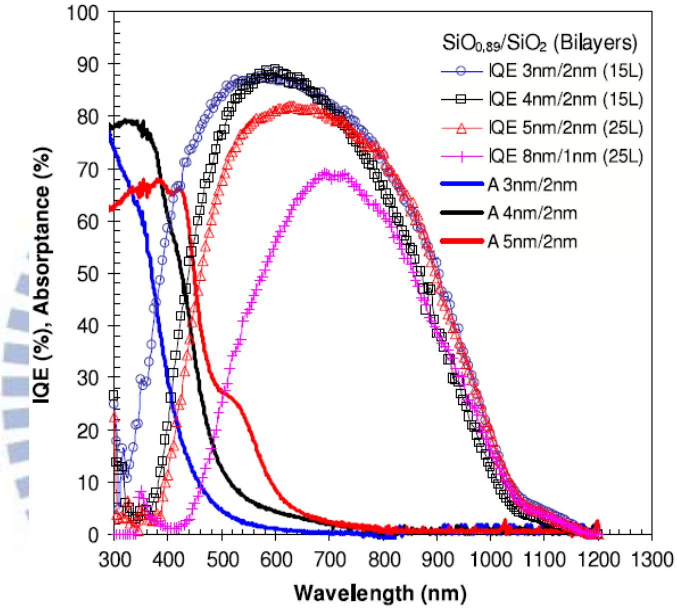

Fig. 1-14: Internal quantum efficiency (IQE) and corresponding absorption spectra of the fabricated n-type Si QDs/p-type c-Si SCs. [16]

Since a large difference of the conversion efficiency between the experimental result and the theoretical calculation result is observed [17], in 2009, M. A. Green et al. publish more results focusing on the Si QD uniformity, interfacial defects, built-in electrical field, etc, in order to find out the roots for this discrepancy and try to optimize this structure for higher conversion efficiency [18-20]. More results for this development are also reported by different groups after 2010. For example, S. H. Hong et al. studied the size-dependent photovoltaic (PV) properties and developed the higher efficiency SCs integrating Si QDs by optimizing the B-doped concentration [21]. However, the results reported by M. A. Green et al. for the all Si QD thin film SCs indicate that the contributions of photo-generated carriers from QDs are apparently limited because of the naturally high-resistance property of the Si-based dielectric matrix materials [22, 23]. Therefore, more advanced and detailed studies are still necessary to solve the various issues involved using the Si-based dielectric matrices.

1-3 Applications on Other Optoelectronic Devices

Except for SCs application, Si QDs have also been extensively studied and integrated into various opto-electronic devices such as light-emitting diodes (LEDs) [24, 25], photodetectors [26], and nonvolatile memory device [27]. For example, LEDs with multi-color light emission properties using Si QDs had been successfully developed by Prof. G. R. Lin et al. [24, 25], and Prof. J. M. Shieh et al. had also integrated Si QDs into near-infrared field-effect transistor photo-detectors by using a metal-oxide-semiconductor (MOS) device structure [26] and nonvolatile memory devices by using a nanosecond laser spike annealing method [27]. Hence, they had exhibited the feasibility and shown the great potential for optoelectronic devices integrating Si QDs.

1-4 Motivation for Solar Cells Application

To summarize the key issues for SCs integrating Si QDs, the Si QD thin films require uniform QD size [21, 28], heavily-doped concentration [21], and smaller QD separation [28-30], that is, higher QD density, or a more suitable matrix material. So far, the Si QD thin films are commonly deposited by a silicon-rich oxide single-layer (SRO-SL) or a [silicon dioxide/silicon-rich oxide] multilayer ([SiO_2/SRO]-ML) structure. The SRO-SL structure is an easy and quick deposition process for the Si QD thin films, however, it is hard to well control the QD size and uniformity and efficiently reduce the QD separation [31, 32]. Although the [SiO_2/SRO]-ML structure promises the QD size control and separation reduction, shown as Fig. 1-15, the minimum thickness of 2 nm for the SiO_2 barrier layers is required to prevent the excess Si atoms in SRO active layers from over-diffusing [11], which will still degrade the carrier transport efficiency [28-30]. Hence, significantly smaller QD separation or other more suitable matrix materials [33] are indispensable for the Si-based SCs development integrating Si QDs.

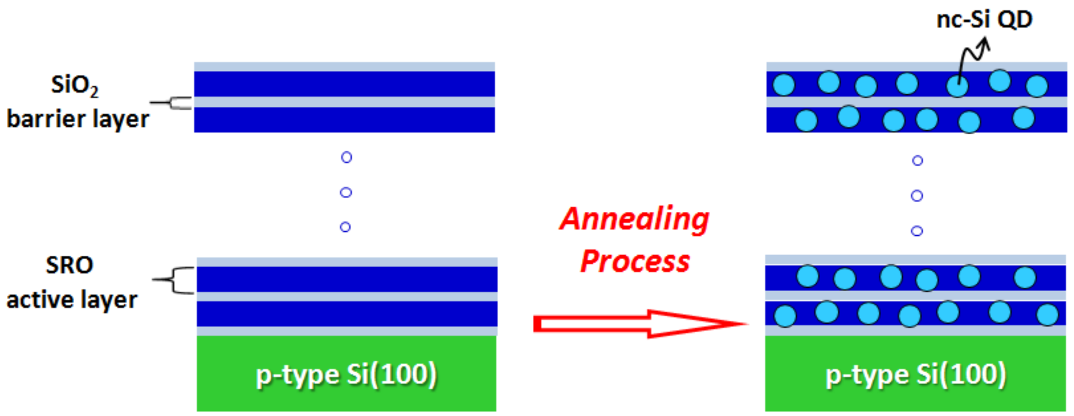

Fig. 1-15: Illustration of the Si QD thin film fabricated by using a [SiO_2/SRO]-ML deposition structure.

1-4.1 Si QD Thin Films Utilizing a Gradient Si-rich Oxide Multilayer (GSRO-ML) Structure

In order to further enhance the carrier transport efficiency, more QD separation reduction is required to significantly increase the carrier tunneling probability [28-30]. Fig. 1-16 shows an illustration of the carrier transport process for the Si QD thin films fabricated by using the traditional [SiO_2/SRO]-ML and novel deposition structures. The red lines mean the main carrier transport paths in both structures, and the thicker lines represent the larger tunneling probability. It indicates when the Si QD thin films with good QD size control and further QD separation reduction are successfully developed, the carrier tunneling probability will be significantly increased due to a narrower barrier width formation. Hence, a novel deposition structure, leading to the good QD size control and further QD separation reduction, can be very helpful for the Si-based SCs integrating Si QDs.

In this study, we propose to develop a novel deposition structure, gradient Si-rich oxide multilayer (GSRO-ML), for the Si QD thin films with good QD size control and QD separation minimization by co-sputtering deposition and high-temperature annealing methods, as shown in Fig. 1-17. Each GSRO period is composed of a highly SRO layer sandwiched between gradient SRO layers. In this proposed structure, the Si-rich atoms are anticipated to self-assemble and take the highly SRO regions as the crystallized centers during annealing due to the significant difference of Si/O composition, and the further reduced QD separation, also means the higher QD density, is expected to be formed after annealing.

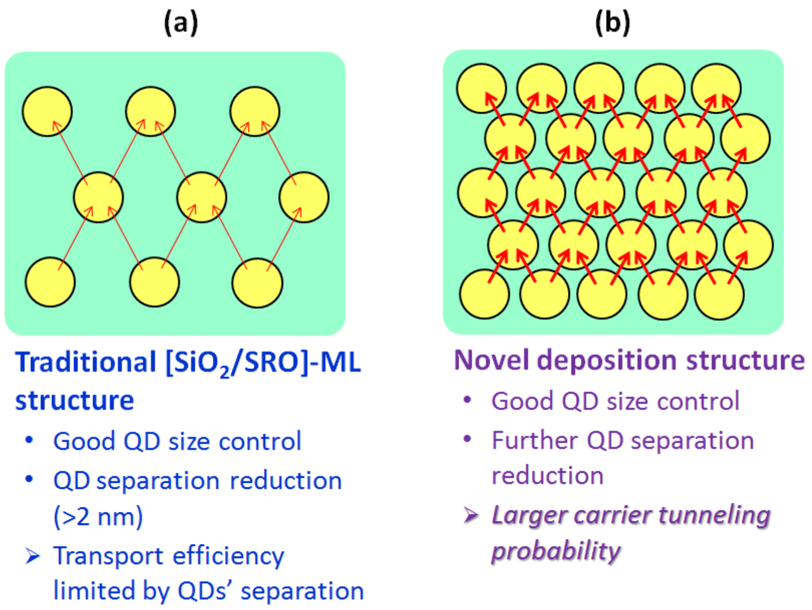

Fig. 1-16: Illustrations of the main carrier transport process in the Si QD thin films fabricated by using the (a) traditional [SiO_2/SRO]-ML and (b) novel deposition structures. The thicker lines in (b) than that in (a) represent the larger tunneling probability obtained.

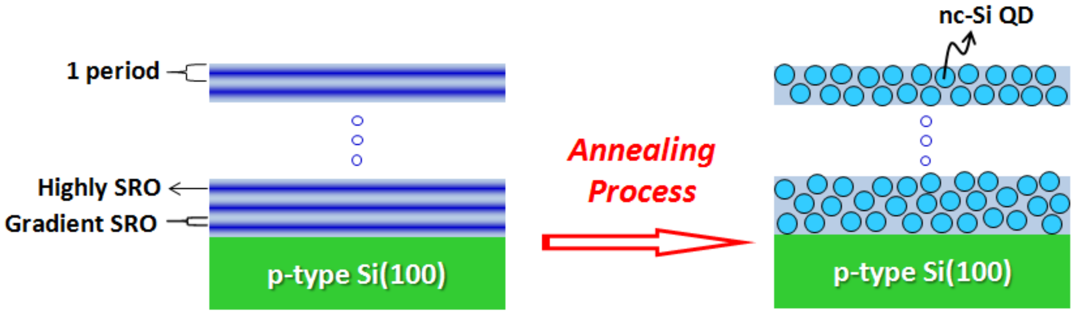

Fig. 1-17: Illustration of the Si QD thin film fabricated by using our proposed GSRO-ML deposition structure.

1-4.2 Si QD Thin Films Utilizing ZnO Matrix Material

In addition to develop the GSRO-ML deposition structure for the Si QD thin films using the Si-based dielectric matrix materials, we also focus on developing a novel and more suitable matrix material since the characteristics of matrix material can obviously influence the electro-optical properties of the Si QD thin films. Fig. 1-18 shows an illustration of the carrier transport process in the Si QD thin films utilizing the insulated and semi-conductive matrix materials. Being different from tunneling through QDs by using an insulated matrix material, more efficient transport paths may be contributed from using a semi-conductive matrix material for the Si QD thin films. Hence, we propose to embed Si QDs into ZnO thin films because ZnO has many desirable features to function as Si QDs' matrix material, such as wide (~3.3 eV) and direct bandgap, high transparency, and highly tunable electrical properties [34]. And so far, only few materials can simultaneously possess these properties. Hence, ZnO can serve as the Si QDs' matrix material for bandgap engineering, reduce the optical loss from matrix's absorption, and efficiently enhance the carrier transport efficiency. Undoubtedly, there are many advantages to embed Si QDs in ZnO thin films for SCs application.

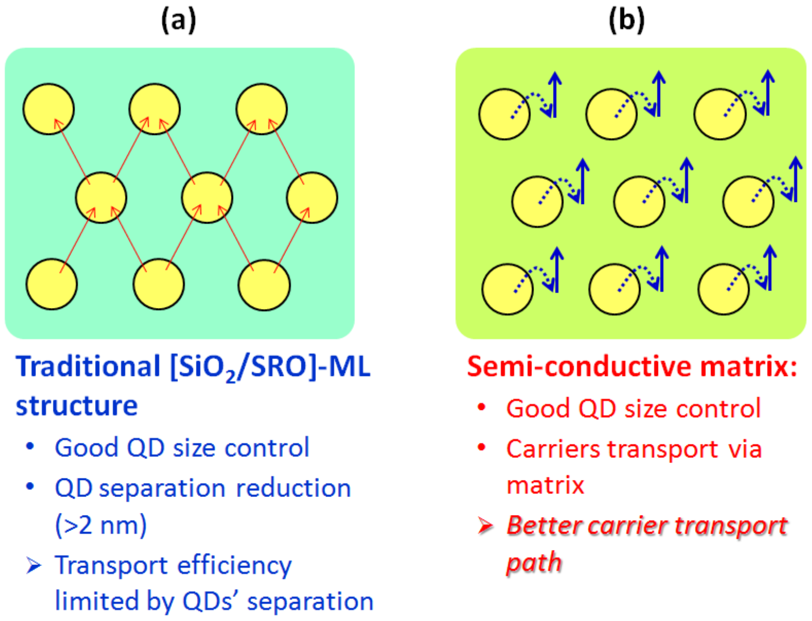

Fig. 1-18: Illustration of the main carrier transport process for Si QDs embedded in an (a) insulated or (b) semi-conductive matrix material. The lines with different colors represent the different carrier transport paths.

1-5 Summary

The third generation SCs with high efficiency and low cost plays the indispensible roles for popularized developments. Si QD has the good ability on bandgap engineering to efficiently improve the mismatched photon energy loss, hence, the Si-based SCs integrating Si QDs can possess great potential on being as the third generation SCs. However, so far, the carrier transport efficiencies are still significantly limited by using the Si-based dielectric matrix materials due to their naturally high resistance properties. In this study, we propose to develop the novel Si QD thin films by utilizing a GSRO-ML deposition structure for further QD separation reduction and integrating with ZnO matrix material for better carrier transport path. The apparatus, sample fabrication, and characteristics for our proposed novel Si QD thin films are investigated and discussed in next chapters.

Chapter 2

Experimental Apparatus

In this chapter, the experimental apparatus for our samples fabrication and characteristics measurement for the novel Si QD thin films are introduced in detail and shown below.

2-1 Apparatus for Sample Fabrication

2-1.1 Wet-bench and Ultrasonic Cleaner

The Si(100) wafers and fused quartzes were used as substrates and cleaned in the wet bench before deposition, as shown in Fig. 2-1(a). The Si wafers were cleaned by a standard Radio Corporation of America (RCA) process to efficiently remove the organic contaminants (organic clean), the thin oxide layer (oxide strip), and the ionic contamination (ionic clean) [35, 36]. The fused quartzes were cleaned by an ultrasonic cleaner, shown as Fig. 2-1(b), the acetone, alcohol, and DI waters were in turn used as the cleaning solvents during ultrasonic oscillation process for 10 minutes individually [37].

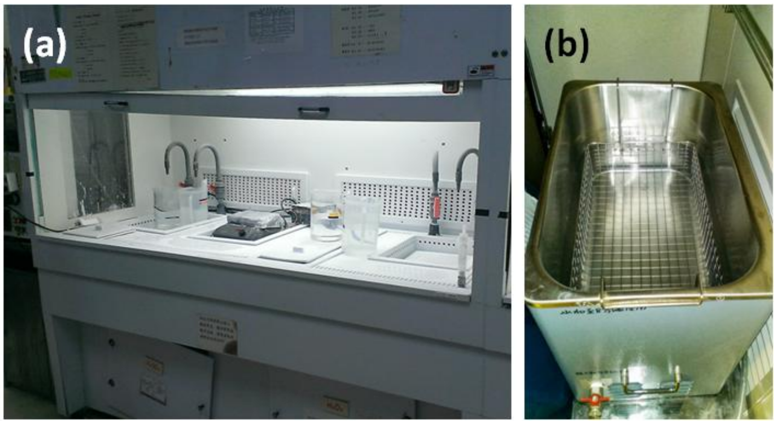

Fig. 2-1: Images of the (a) wet-bench and (b) ultrasonic cleaner.

2-1.2 Radio-Frequency Magnetron Co-Sputtering System

The Si QD thin films were deposited by using a radio-frequency (RF) magnetron co-sputtering system, the outside image is shown in Fig. 2-2(a). There are two chambers in this sputtering system including the sputtering and loading ones. The films deposition process is made in the sputtering chamber; the loading chamber is designed for quick sample transportation under keeping the high vacuum in the sputtering chamber. The inside image of this sputtering chamber is also shown in Fig. 2-2(b), it's mainly composed of one sample lift arm, one sample rotation stage, four sputtering guns, and two shutters. The sample lift arm is installed for the sample transportation process between the sputtering and loading chambers. The sample holder is put on the sample rotation stage, which rotates at 15 r.p.m. during sputtering for uniform film deposition. The four sputtering guns are designed for the requirement of different sputtering materials during deposition. The two shutters are set up for the sample protection when the sputtering material is changed. In addition, the base pressure of this sputtering system was controlled at a high vacuum range of $<5\times10^{-7}$ torr for the good film quality obtained. Fig. 2-3 shows an illustration of the sputtering deposition process. In this study, the n-type Si QD embedded SiO_2 thin films were deposited by co-sputtering the P-doped Si and pure SiO_2 materials, and the Si QD embedded ZnO thin films were obtained by sputtering the intrinsic Si and ZnO materials individually.

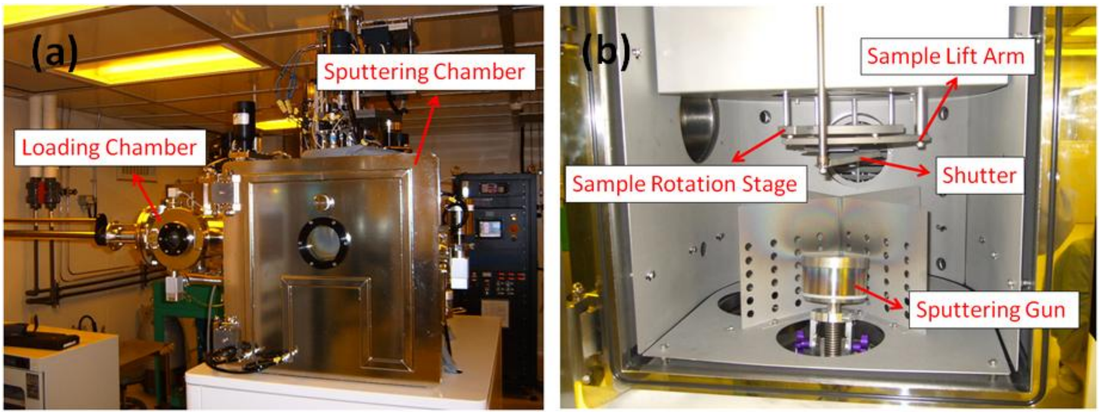

Fig. 2-2: (a) Outside and (b) inside images of the RF magnetron co-sputtering system.

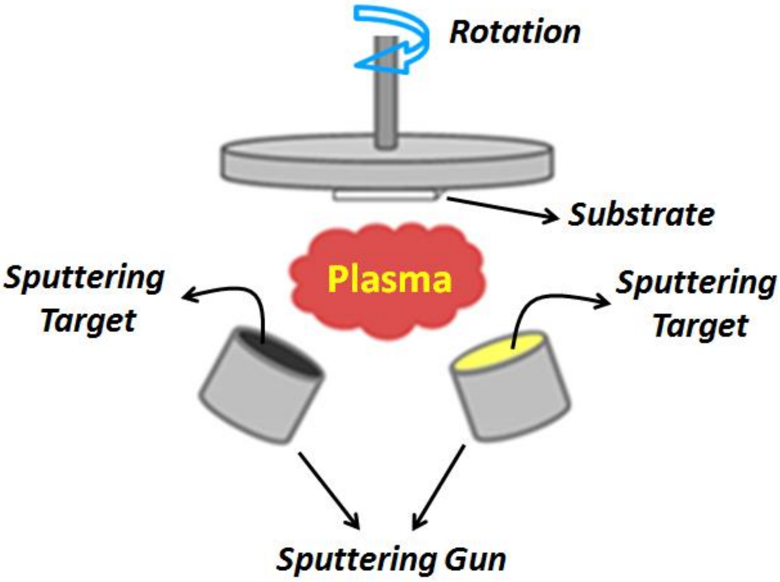

Fig. 2-3: Illustration of a sputtering deposition process.

2-1.3 Furnace Annealing System

In order to obtain the nano-crystalline Si QDs formation, the as-deposited multilayer thin films were annealed by furnace annealing (FA). The images of the FA system and its main components, such as the proportional-integral-derivative (PID) temperature auto-controller, mass flow controller (MFC), heating chamber, mechanical pump, and entrance and exit of gas, are shown in Fig. 2-4. In this FA system, the temperature is auto-controlled by the PID temperature controller, and the maximum temperature is allowed at 1100℃. There are four kinds of high purity gases can be used, including N_2, Ar, O_2, and H_2+N_2, besides, the annealing process in vacuum for $<5\times10^{-3}$ torr is also workable by using the mechanical pump. An illustration of the FA process is shown in Fig. 2-5. A large flowing rate of N_2 gas was performed to efficiently decrease the reactions with air during annealing. By utilizing this FA system, the Si QD thin films with good crystalline quality can be obtained after annealing.

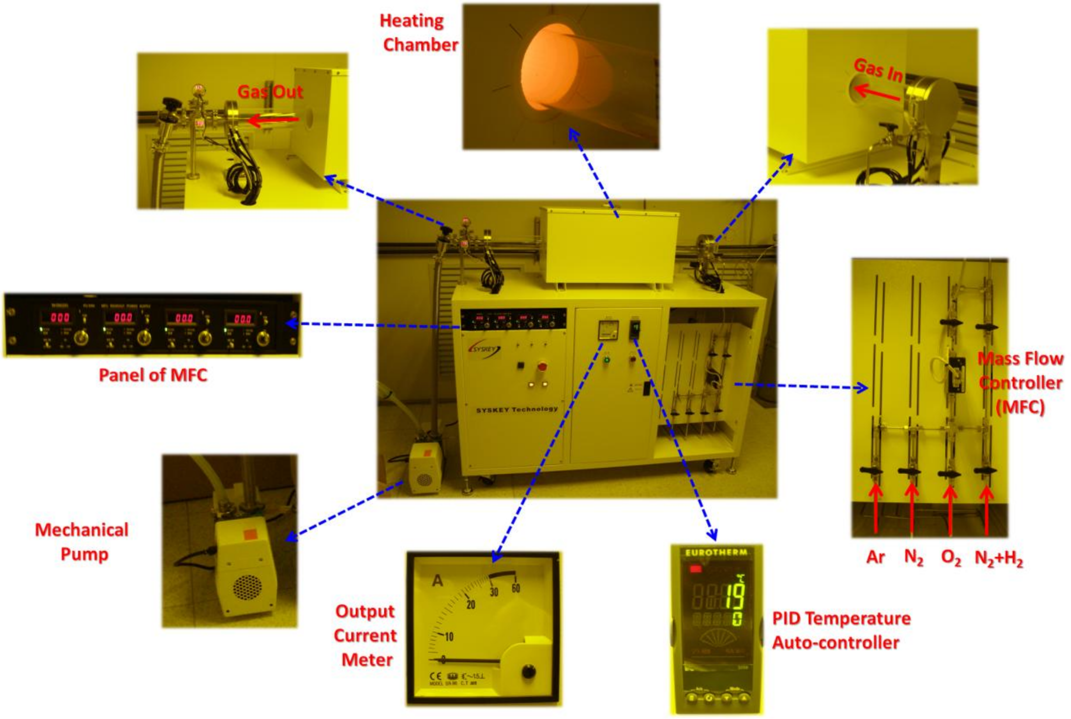

Fig. 2-4: Images of the furnace annealing system and its main components.

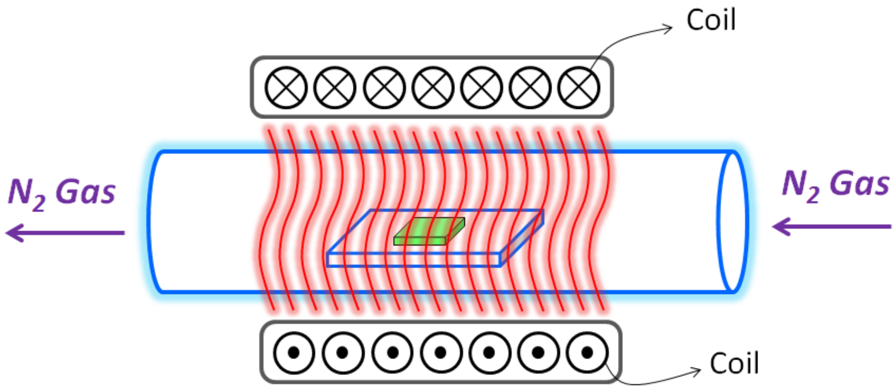

Fig. 2-5: Illustration of a furnace annealing process.

2-1.4 Reactive Ion Etching System

For electrical properties measurements, the annealed samples for the Si QD embedded SiO_2 thin films were etched by reactive ion etching (RIE) process with CHF_3 and O_2 gases to remove the top SiO_2 layers formed during annealing. The RIE process was made by a SAMCO RIE200L system, which is supported from Nano Facility Center (NFC) in National Chiao Tung University (NCTU), shown as Fig. 2-6. An illustration of a RIE system and its etching process is shown in Fig. 2-7, it's consisted of two electrodes (1 and 4) that create an electric field (3) meant to accelerate ions (2) toward the surface of the samples (5) [38]. The chemically reactive plasma is generated under low pressure by an electromagnetic field. Then, the high-energy ions from the plasma attack the sample surface and react with it, and the material on the sample surface will be removed during etching process [38].

Fig. 2-6: Image of the reactive ion etching system (RIE200L, SAMCO).

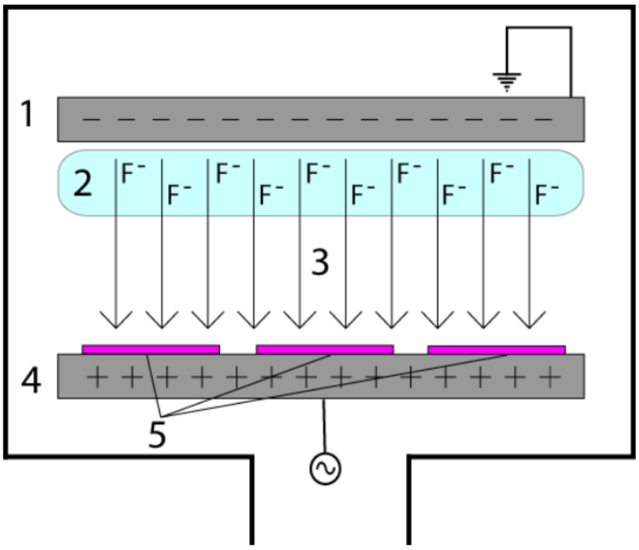

Fig. 2-7: Illustration of a reactive ion etching process. ((1) and (4): two electrodes, (2): F^- ions, (3): electric field, (5): samples) [38]

2-1.5 Thermal Evaporator

For electrical properties measurements, the Al or Ni electrode layer with 100 nm thickness was deposited on the top and bottom surfaces of samples at room-temperature by thermal evaporator, shown as Fig. 2-8. The thermal evaporation process is also illustrated in Fig. 2-9 [39]. In this study, the base pressure during thermal evaporation was controlled at $<4\times10^{-6}$ torr. After electrode layers deposition, the samples were heated at 200℃ in N_2 environment for 20 minutes to form the good ohmic contact.

Fig. 2-8: Image of the thermal evaporator.

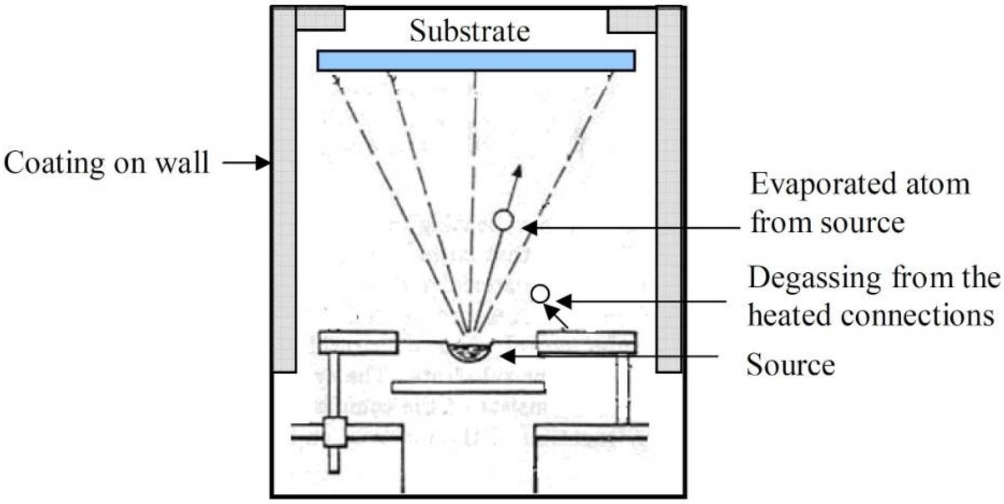

Fig. 2-9: Illustration of a thermal evaporation process. [39]

2-2 Apparatus for Characterization Measurement

2-2.1 Micro-Raman Spectroscopy

The Raman spectra were measured by using a high-resolution confocal micro-Raman spectroscopy (Horiba LabRam HR) with a 488 nm diode-pumped solid-state laser, as shown in Fig. 2-10, it’s supported from Prof. Kien-Wen Sun’s laboratory at Centre of Nanoscience and Technology (CNST) in National Chiao Tung University (NCTU). An illustration of a micro-Raman spectroscopy and its measurement process are also shown in Fig. 2-11 [40].

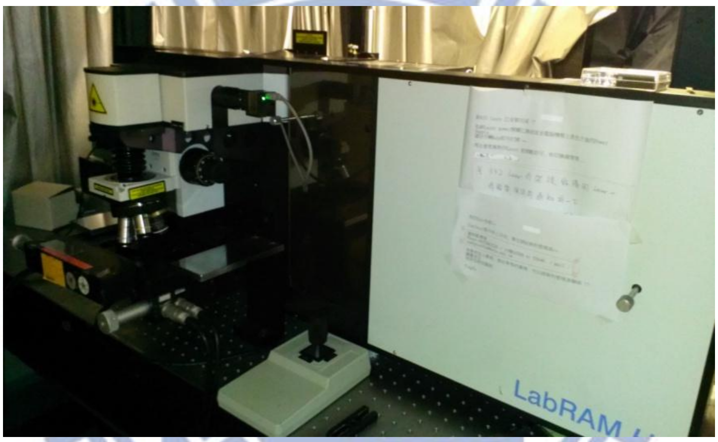

Fig. 2-10: Image of the micro-Raman and micro-photoluminescence (PL) spectroscopy (Horiba LabRam HR).

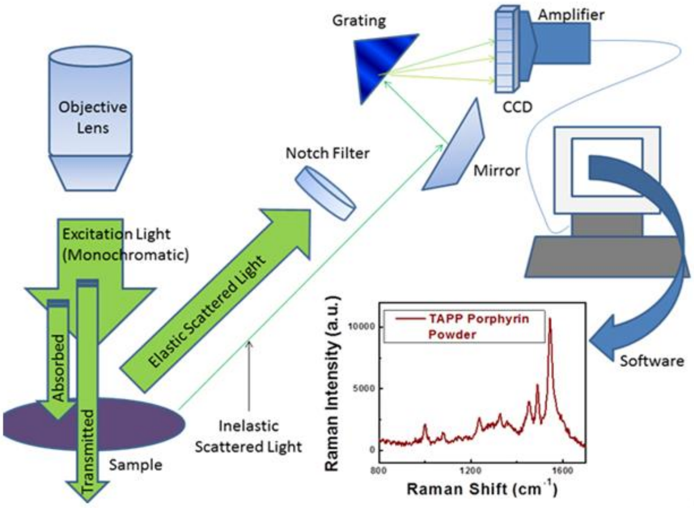

Fig. 2-11: Illustration of a micro-Raman spectroscopy system and its measurement process. [40]

2-2.2 Micro-Photoluminescence Spectroscopy

The micro-photoluminescence (PL) spectra were measured by a Horiba LabRam HR, which is the same with the micro-Raman spectra measurements, and a 488 nm diode-pumped solid-state laser was also used as the excitation source. An illustration of a micro-PL spectroscopy is also shown in Fig. 2-12 [41].

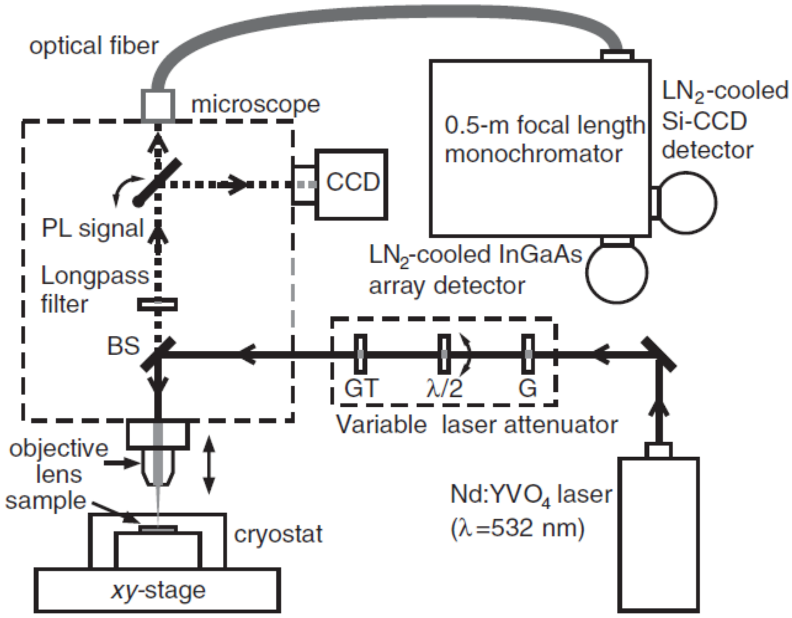

Fig. 2-12: Illustration of a micro-PL spectroscopy system. [41]

2-2.3 X-Ray Diffractometer

The X-ray diffraction (XRD) patterns were examined by a high-resolution X-ray diffractometer (Bede, D1) with Cu K_α radiation, as shown in Fig. 2-13; it’s supported from Centre of Nanoscience and Technology (CNST) in National Chiao Tung University (NCTU). In this study, the grazing incident X-ray diffraction (GIXRD) method, illustrated as Fig. 2-14, was used as the scan mode for the crystallization examinations of thin films [42]. During XRD measurements, the incident angle and the integration time were fixed at 0.5° and 2 seconds respectively.

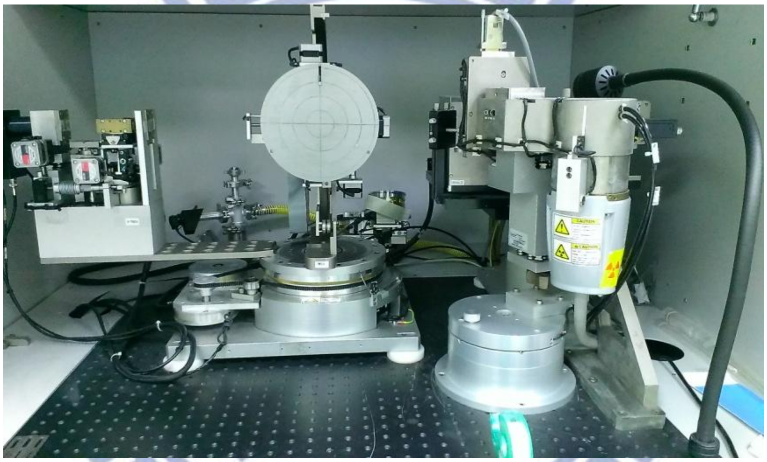

Fig. 2-13: Image of the X-ray diffractometer (Bede D1).

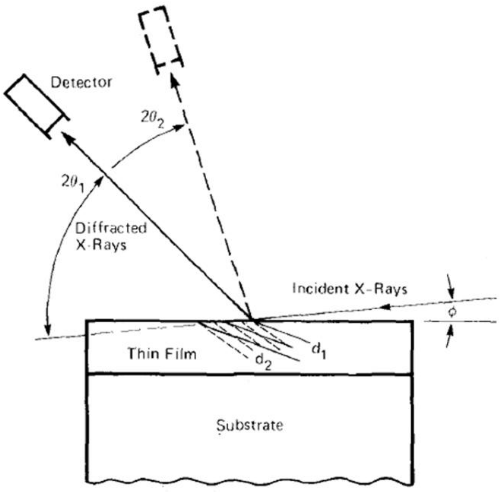

Fig. 2-14: Illustration of the grazing incident X-ray diffraction method. [42]

2-2.4 Ultraviolet/Visible/Near-Infrared Spectroscopy

The optical transmission and reflection spectra were obtained using a variable-angle ultraviolet/visible/near-infrared (UV-VIS-NIR) spectroscopy (Hitachi U-4100) with an integrating sphere inner-coated by $BaSO_4$, as shown in Fig. 2-15, which is supported from Centre of Nanoscience and Technology (CNST) in National Chiao Tung University (NCTU). The measurement process of UV/VIS/NIR spectra is also illustrated in Fig. 2-16 [43].

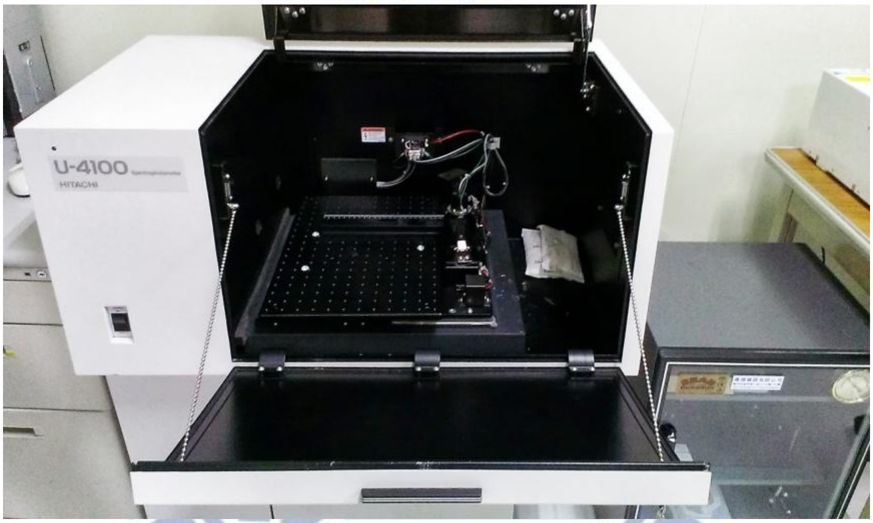

Fig. 2-15: Image of the ultraviolet/visible/near-infrared spectroscopy (Hitachi U-4100).

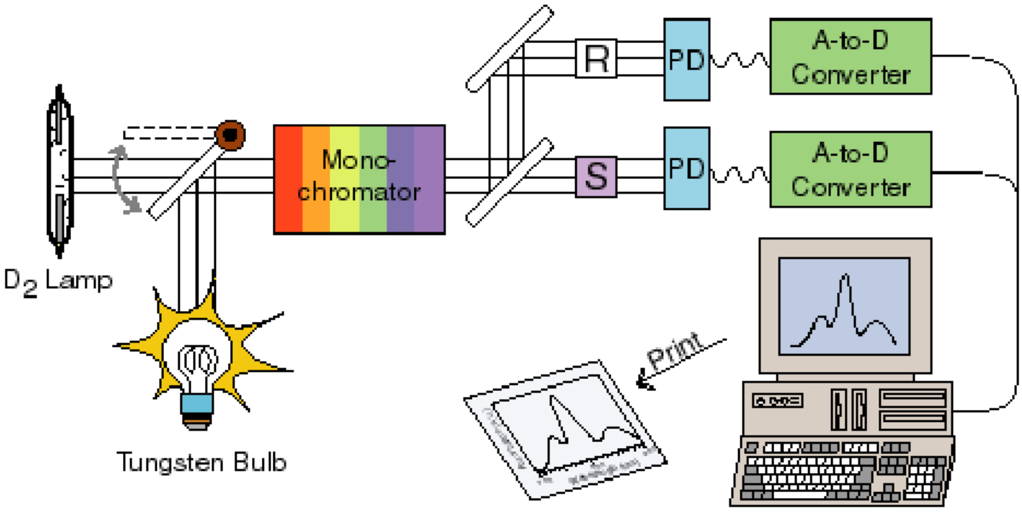

Fig. 2-16: Illustration of an ultraviolet/visible/near-infrared spectroscopy. [43]

2-2.5 Atomic Force Microscope

The surface morphologies were analyzed by a Digital Instrument D3100 atomic force microscope (AFM) shown as Fig. 2-17, it's supported from Centre of Nanoscience and Technology (CNST) in National Chiao Tung University (NCTU). The detection of AFM images was designed as a beam deflection method, as shown in Fig. 2-18 [44], and the morphologies were scanned in a tapping mode.

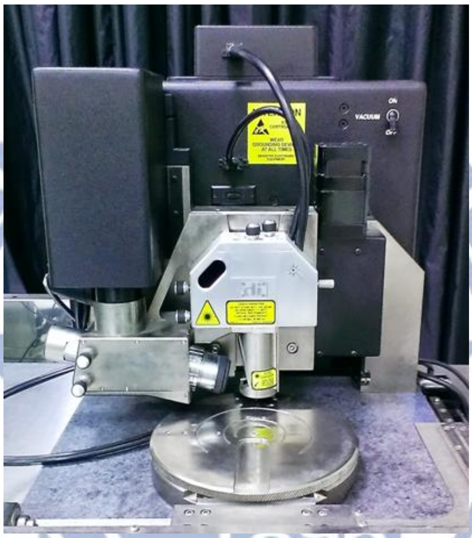

Fig. 2-17: Image of the atomic force microscope (D3100).

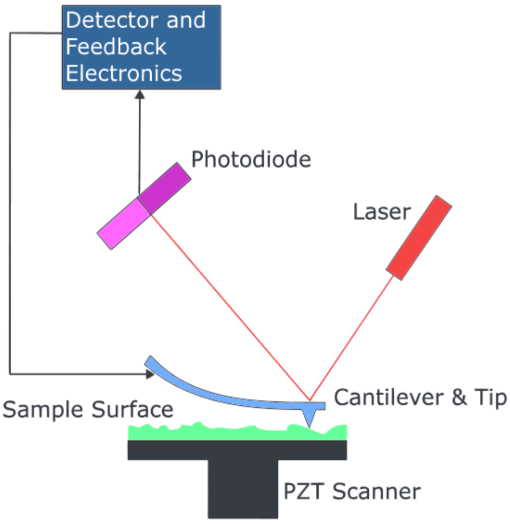

Fig. 2-18: Illustration of an atomic force microscope using a beam deflection detection method. [44]

2-2.6 Transmission Electron Microscope

The high-resolution transmission electron microscope (TEM) images were observed by a JEOL JEM-2010F TEM, as shown in Fig. 2-19, which is supported from National Nano Device Laboratories (NDL). An illustration of a TEM system with basic optical components is also illustrated in Fig. 2-20 [45]. The samples for TEM images were prepared by the conventional method, including the cutting, grinding, polishing, dimpling, and ion milling processes and thinned down to electron transparency using a precision ion polishing system (Gatan 691) shown as Fig. 2-21.

Fig. 2-19: Image of the transmission electron microscope (JEOL JEM-2010F).

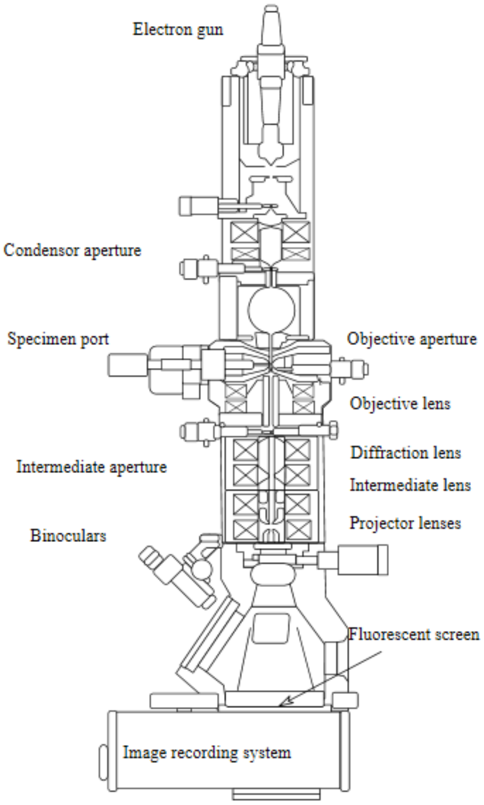

Fig. 2-20: Illustration of a transmission electron microscope. [45]

Fig. 2-21: Image of the precision ion polishing system (Gatan 691).

2-2.7 Semiconductor Device Measurement System

The dark and light current-voltage (I-V) curves were measured by a semiconductor device measurement system shown as Fig. 2-22. Fig. 2-23 also shows the magnified images of the main components in this measurement system, it mainly involves an Agilent E5270B precision measurement mainframe, a measurement station, and a halogen light source. In the light I-V curves, an illumination with power density of ~1 mW/cm^2 from the light source was used for the examinations of photoresponsive properties.

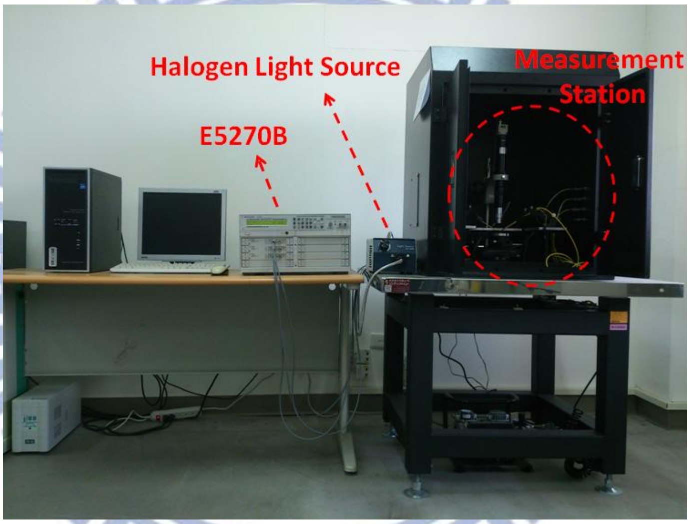

Fig. 2-22: Image of the semiconductor device measurement system.

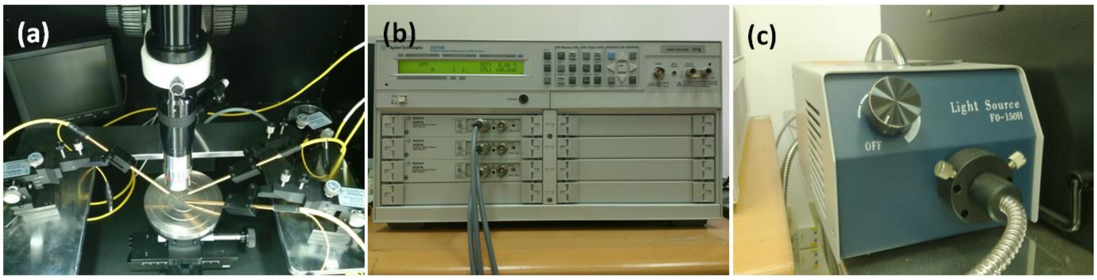

Fig. 2-23: Images of the main components of the semiconductor device measurement system: (a) measurement station, (b) Agilent E5270B precision measurement mainframe, and (c) halogen light source.

2-2.8 Solar Simulator Measurement System

The performances of our fabricated solar cells (Discussed in Appendix) were measured under one sun condition (Class A, AM1.5G) by a solar simulator measurement system (Newport), as shown in Fig. 2-24, which is supported from Prof. Pei-Chen Yu’s laboratory at Institute of Electro-Optical Engineering in National Chiao Tung University (NCTU). An illustration of the solar simulator measurement system is also illustrated in Fig. 2-25.

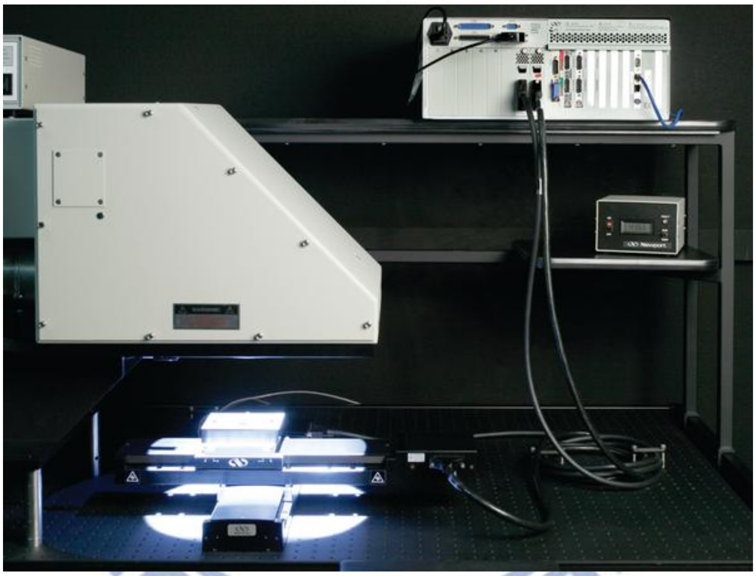

Fig. 2-24: Image of the solar simulator measurement system (Newport).

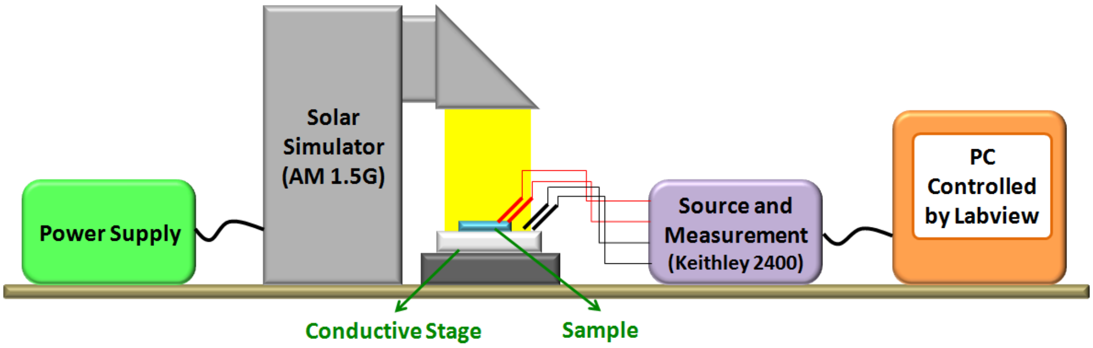

Fig. 2-25: Illustration of the solar simulator measurement system.

2-2.9 Quantum Efficiency Measurement System

The quantum efficiency (QE) spectra of our fabricated solar cells (Discussed in Appendix) were examined by a QE measurement system (Hitachi QE-3000) shown as Fig. 2-26, which is supported from Centre of Nanoscience and Technology (CNST) in National Chiao Tung University (NCTU). The measurement process for a QE system is also illustrated in Fig. 2-27 [46].

Fig. 2-26: Image of the quantum efficiency measurement system (Hitachi QE-3000).

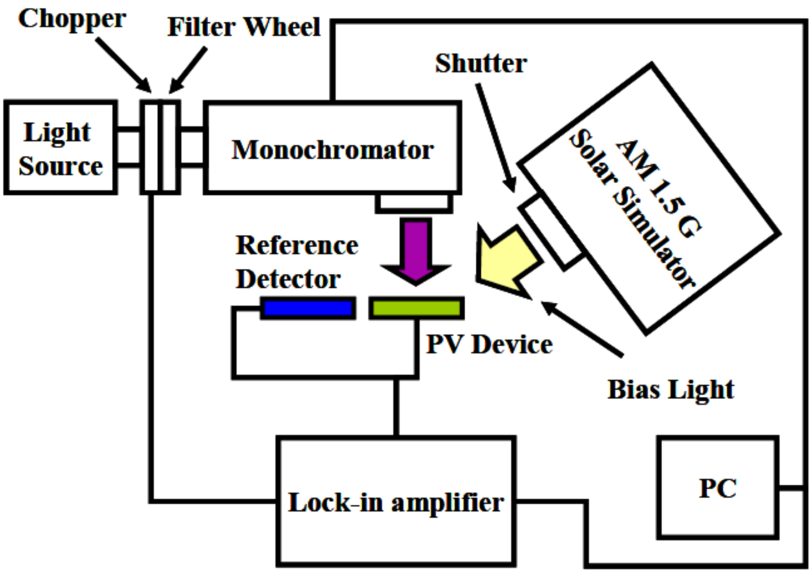

Fig. 2-27: Illustration of a quantum efficiency measurement system. [46]

Chapter 3

Si QD Thin Films Utilizing a Gradient Si-rich Oxide Multilayer (GSRO-ML) Structure

In chapter 3, a novel deposition structure, gradient Si-rich oxide multilayer (GSRO-ML), was developed to further reduce QD separation for the Si QD embedded SiO_2 thin films. Comparisons in the nano-structural, optical and electrical, and photovoltaic (PV) properties between the Si QD thin films utilizing the commonly-used [SiO_2/SRO]-ML structure and our proposed GSRO-ML structure were investigated and discussed.

3-1 Sample Fabrication

The n-type GSRO-ML thin films were deposited on p-type Si(100) wafers with 1~10 ohm-cm in resistivity and fused quartzes at room-temperature by radio-frequency (RF) magnetron co-sputtering deposition method. Before deposition, the Si wafers and the fused quartzes were cleaned by the standard RCA and ultrasonic oscillation processes individually. The Si material with phosphorus doping concentration of ~1×10^{18} cm^{-3} and pure SiO_2 material were used as the sputtering targets. The sputtering power of Si (P_{Si}) for each GSRO period was increased from 30 to 110 W at a rate of 1 W/s and hold at 110 W for 1 nm thickness, then decreased from 110 to 30 W also at a rate of 1 W/s while that of SiO_2 (P_{SiO2}) was fixed at 20 W, as illustrated in Fig. 3-1.

Fig. 3-2(a) shows the fabrication process of the GSRO-ML thin films with 20 periods before and after annealing. Each GSRO period is composed of a highly SRO layer sandwiched between gradient SRO layers for a total thickness of 4 nm during deposition, and a super-high QD density is expected to be formed after annealing at 1100℃ for 1 hour. For electro-optical properties measurements, the annealed samples were etched by reactive ion etching (RIE) process with CHF_3 and O_2 gases to remove the top SiO_2 layers formed during annealing. After RIE process, the Al electrodes were deposited on the top and bottom surfaces of samples with 100 nm thicknesses by thermal evaporator, and a square electrode array with area of 0.8×0.8 mm^2 and side-to-side separation of 1 mm was used as the top electrode distribution for photo-response measurements. For comparison, a [SiO_2/SRO]-ML thin film with 20 periods was also fabricated, and the film structure before and after annealing is shown in Fig. 3-2(b). The SiO_2 thin-layers with 2 nm thickness and highly SRO thin-layers with 5 nm thickness was periodically deposited. The highly SRO thin-layers were co-sputtered by 110 W of P_{Si} and 10 W of P_{SiO2}. After deposition, a high-temperature annealing process was also performed at 1100℃ for 1 hour for Si QDs formation.

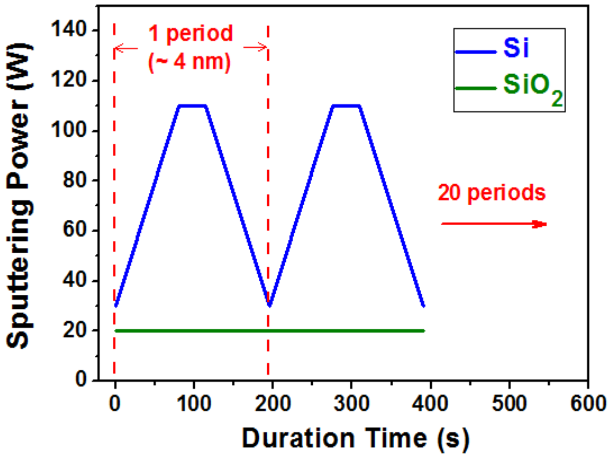

Fig. 3-1: Variations of the Si and SiO_2 sputtering powers during deposition for sample GSRO-ML.

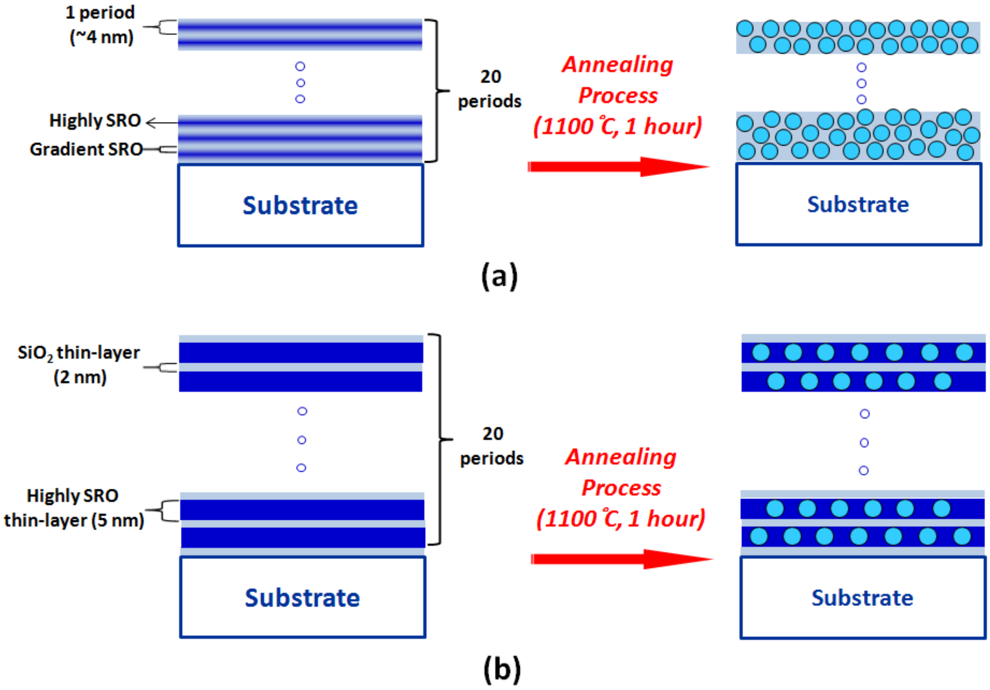

Fig. 3-2: Illustrations of film structures for samples (a) GSRO-ML and (b) [SiO_2/SRO]-ML before and after annealing.

3-2 Nano-Crystalline and Structural Properties

Raman spectrum measurement is a reliable and widely-used technique for examining the properties of nano-crystalline Si (nc-Si) materials [47, 48]. Fig. 3-3 shows the Raman spectra of samples GSRO-ML and [SiO_2/SRO]-ML, in which the observed peaks near 520 cm^{-1} represent the nc-Si formation. In general, the signal can be decomposed into three components including the peaks located at ~480, 500~510, and 510~520 cm^{-1}, which originate from the transverse optical (TO) modes of Si-Si vibrations in the amorphous- (a-Si), intermediate- (i-Si), and nano-crystalline Si (nc-Si) phases [47]. The curve-fitting results from Raman spectra are listed in Table 3-1. The similar FWHM values of nc-Si phase for both samples indicate the close average sizes of nc-Si [48]. However, sample GSRO-ML shows not only significantly larger nc-Si intensity but also higher Si crystal volume fraction ($f_{c\text{-}Si}$) than those of sample [SiO_2/SRO]-ML. This means using a GSRO-ML structure can lead to larger amount of nc-Si with better crystal quality. Hence, compared with the commonly-used [SiO_2/SRO]-ML structure, our proposed GSRO-ML structure can largely enhance the nc-Si formation while maintaining the control ability of nc-Si size for the Si QD thin films.

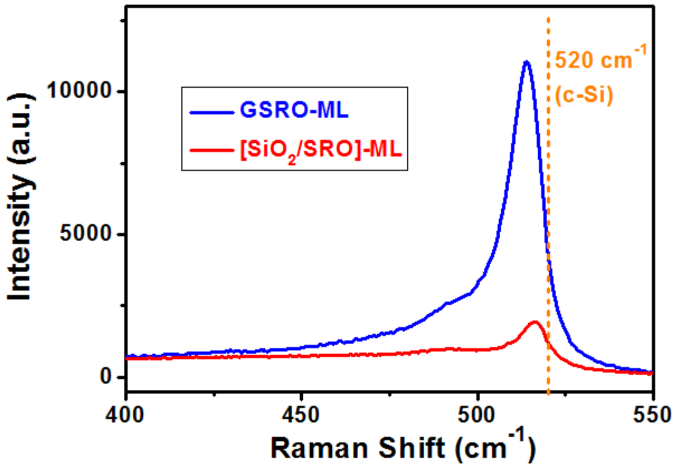

Fig. 3-3: Raman spectra of samples GSRO-ML and [SiO_2/SRO]-ML.

Table 3-1: Curve-fitting results from Raman spectra for the crystalline properties of samples GSRO-ML and [SiO_2/SRO]-ML.

Sample	**TO mode of nc-Si phase**			**Si crystal volume fraction ($f_{c\text{-}Si}$) (%)**
	Peak position (cm^{-1})	**FWHM (cm^{-1})**	**Integrated intensity per nanometer in thickness (a.u.)**	
GSRO-ML	514.0	9.8	1.4×10^2	73.0
[SiO_2/SRO]-ML	516.3	9.7	1.2×10^1	68.4

Figs. 3-4(a) and (b) show the high-resolution TEM images of samples [SiO_2/SRO]-ML and GSRO-ML. Most of Si QDs in sample [SiO_2/SRO]-ML are formed in SRO layers and separated by SiO_2 barrier layers. For sample GSRO-ML, a large number of Si QDs with closer separation is clearly observed, which indicates that a super-high density of Si QDs can be formed by using a GSRO-ML structure. Fig. 3-4(c) shows the corresponding QD size distributions from estimating 40 QDs in samples [SiO_2/SRO]-ML and GSRO-ML. Both samples reveal the similar QD size distributions, mainly from 4 to 6 nm, and the close average QD sizes of ~5.2 and ~4.9 nm. However, the calculated QD density of ~3×10^{12} cm^{-2} for sample GSRO-ML is significantly higher than that of ~9×10^{11} cm^{-2} for sample [SiO_2/SRO]-ML, which is close to the QD density calculated from the reports by G. Conibeer et al. and M. Zacharias et al. [10, 11]. Therefore, the Si QD thin film using a GSRO-ML structure shows excellent capabilities on not only the QD size control but also the super-high QD density formation, and such results are very helpful for SCs application integrating Si QDs.

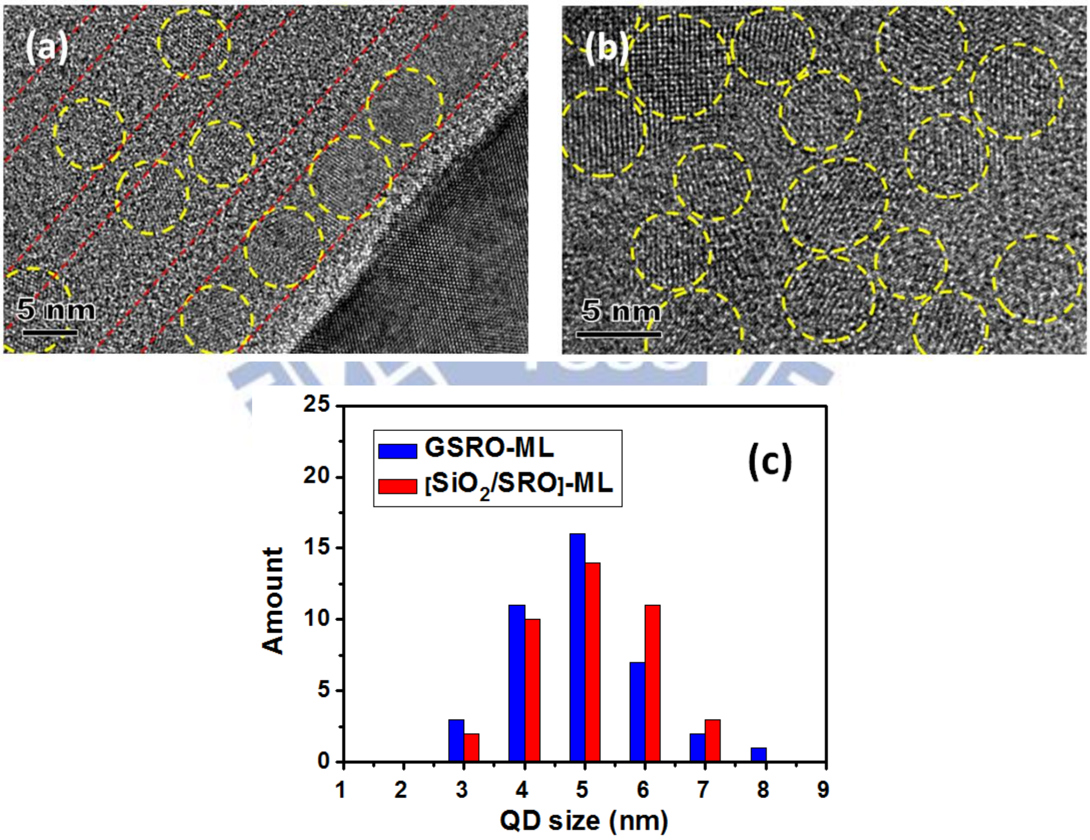

Fig. 3-4: High-resolution TEM images of samples (a) [SiO_2/SRO]-ML and (b) GSRO-ML. (c) The corresponding QD size distributions.

3-3 Photoluminescence Emission and Optical Absorption Properties

The effective bandgap and light emission properties of the Si QD thin films have been widely investigated by photoluminescence (PL) spectrum [49-51]. The main PL emissions are from the quantum confinement (PL_{QC}) effect accompanying with the carrier recombinations from the interface defect states between Si QDs and SiO_2 matrix ($PL_{D\text{-}interface}$) and the defect states in SiO_2 matrix ($PL_{D\text{-}SiO2}$) [49-51]. Fig. 3-5 shows the PL spectra and the fitting curves of samples GSRO-ML and [SiO_2/SRO]-ML, and the curve-fitting results are given in Table 3-2. The broad PL emission properties are observed in both samples, and they can be nicely decomposed into three components, contributed from PL_{QC}, $PL_{D\text{-}interface}$, and $PL_{D\text{-}SiO2}$. The effective bandgap obtained from the peak position of PL_{QC} in sample GSRO-ML is a little larger than that in sample [SiO_2/SRO]-ML, mainly owing to the slightly smaller average QD size [11], but not the closer QD separation, which will lead to an energy red shift [30]. In addition, sample GSRO-ML, with higher QD density, exhibits a considerably lower PL_{QC} intensity than that of sample [SiO_2/SRO]-ML. This indicates that more photo-generated carriers can transport through QDs rather than recombine inside QDs during PL spectrum measurement since the QD separation is significantly reduced. The increased $PL_{D\text{-}SiO2}$ in sample GSRO-ML is a reasonable result because the all Si-rich oxide matrix is used and more Si excess atoms will be left behind inside the SiO_2 matrix after Si QDs formation [51]. Since a suitable number of defect states inside SiO_2 matrix can improve the carrier transport efficiency for the Si QD thin films [28, 52], the Si QD thin film using a GSRO-ML structure is more advantageous for SCs application. Therefore, the PL measurement results of the Si QD thin film using the proposed GSRO-ML structure with super-high QD density and good QD size control reveal the better properties and the capability of effective bandgap engineering even though the Si QDs are closely formed.

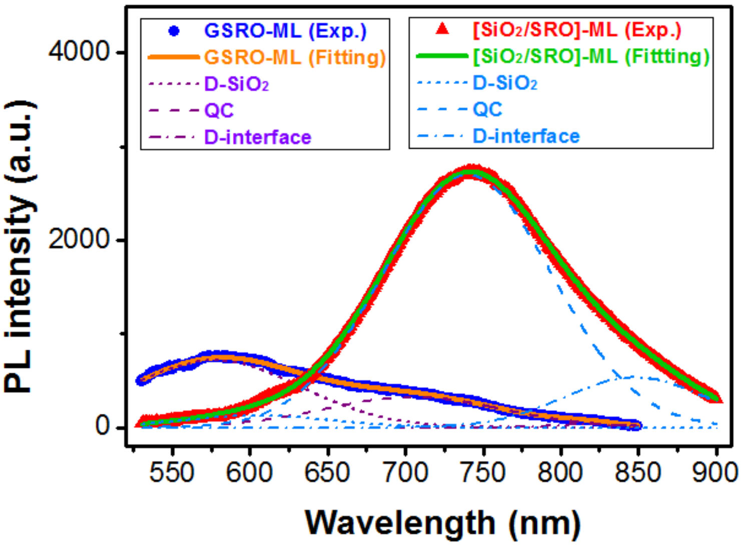

Fig. 3-5: PL spectra and the fitting curves of samples GSRO-ML and [SiO_2/SRO]-ML.

Table 3-2: Curve-fitting results from PL spectra of samples GSRO-ML and [SiO_2/SRO]-ML.

Sample	**Defect states in SiO_2 matrix (D-SiO_2)**		**Quantum confinement effect (QC)**		**Interface defect states (D-interface)**	
	Peak position	**Intensity (a.u.)**	**Peak position**	**Intensity (a.u.)**	**Peak position**	**Intensity (a.u.)**
GSRO-ML	2.15 eV (577 nm)	8.0×10^4	1.76 eV (705 nm)	4.6×10^4	1.52 eV (816 nm)	1.5×10^3
[SiO_2/SRO]-ML	2.05 eV (604 nm)	1.4×10^4	1.68 eV (740 nm)	3.7×10^5	1.46 eV (848 nm)	6.0×10^4

To further confirm the cause of the reduced PL_{QC} emission in sample GSRO-ML, Fig. 3-6 shows the I-V curves of samples GSRO-ML and [SiO_2/SRO]-ML with and without a 488 nm laser illumination, which is used for PL spectrum measurements. A much more obvious I_{SC} enhancement is observed in sample GSRO-ML than that in sample [SiO_2/SRO]-ML in the light I-V curves. This verifies that the reduced PL_{QC} emission in sample GSRO-ML is mainly caused by the better carrier transport properties resulting from the closer QD separation than that in sample [SiO_2/SRO]-ML.

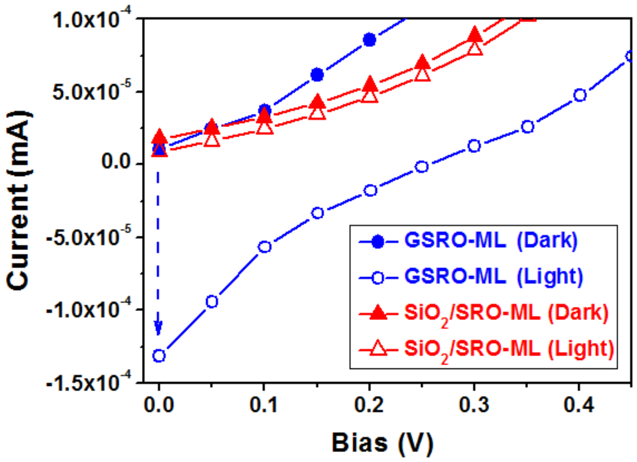

Fig. 3-6: I-V curves of samples GSRO-ML and [SiO_2/SRO]-ML with and without a 488 nm laser illumination.

In order to understand the optical absorption properties of samples GSRO-ML and [SiO_2/SRO]-ML, the absorption spectra are measured and shown in Fig. 3-7. The absorption coefficient of sample GSRO-ML is clearly larger than that of sample [SiO_2/SRO]-ML owing to the higher QD density. Inset of Fig. 3-7 shows the Tauc plot for indirect allowed transition. The optical bandgap ($E_{g,opt}$) can be evaluated by linear extrapolating the interception at the energy axis ($\alpha h\nu$=0) from the plot of $(\alpha h\nu)^{1/2}$ as a function of incident photon energy ($h\nu$), where α is the optical absorption coefficient [53]. The obtained $E_{g,opt}$ of samples GSRO-ML and [SiO_2/SRO]-ML are 1.96 and 1.83 eV, and the corresponding α values are 3.4×10^3 and 3.1×10^2 cm^{-1}. The slightly larger $E_{g,opt}$ of sample GSRO-ML than that of sample [SiO_2/SRO]-ML matches with the obtained results of effective bandgap from PL_{QC} emission, which is contributed from the little difference in average QD size. Furthermore, the α value of sample GSRO-ML is significantly improved to be over 10 times larger than that of sample [SiO_2/SRO]-ML and close to that of amorphous Si material [54]. This means the Si QD thin films using a GSRO-ML structure can contribute the better photo-responsive property and largely reduce the required film thickness for SC applications. Therefore, our proposed GSRO-ML structure makes the Si QD thin film more practical and potential for the commercial SCs development.

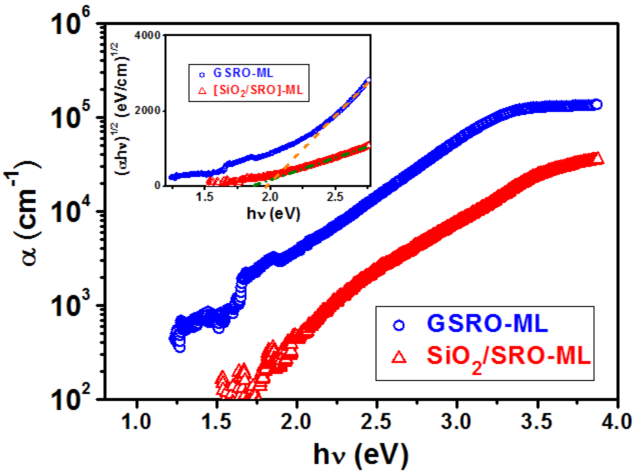

Fig. 3-7: Absorption spectra of samples GSRO-ML and [SiO_2/SRO]-ML. Inset shows the corresponding Tauc plots for indirect allowed transition.

3-4 Photovoltaic Properties and Carrier Transport Mechanism

Fig. 3-8 shows the illustration of the device structure for I-V measurements and the dark and light I-V curves of samples GSRO-ML and [SiO_2/SRO]-ML. Both samples reveal the rectification behavior as a diode. However, the better I-V characteristics including a lower turn-on voltage and a higher forward current are obtained in sample GSRO-ML. Inset of Fig. 3-8(b) shows the corresponding light I-V curves under a halogen lamp illumination with ~1 mW/cm^2 of power density. The V_{OC} and I_{SC} for sample GSRO-ML are 302 mV and 5.5×10^{-4} mA, significantly larger than 110 mV and 2.6×10^{-5} mA for sample [SiO_2/SRO]-ML. Hence, the PV properties of the Si QD thin film are efficiently enhanced by using the GSRO-ML structure.

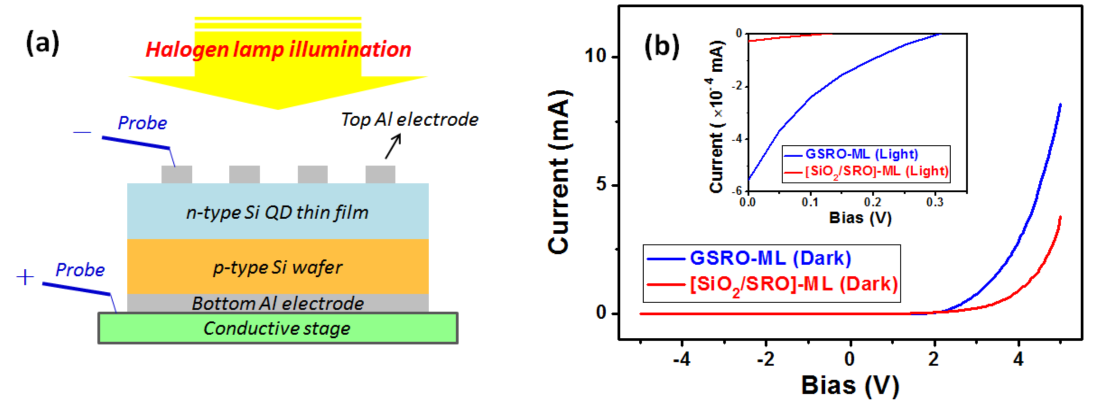

Fig. 3-8: (a) Illustration of the device structure for I-V measurements and (b) the dark I-V curves of samples GSRO-ML and [SiO_2/SRO]-ML. Inset shows the corresponding light I-V curves under a halogen lamp illumination.

To investigate the carrier transport mechanism, the dark forward I-V curves of samples [SiO_2/SRO]-ML and GSRO-ML are plotted on a log-log and shown in Fig. 3-9. For sample [SiO_2/SRO]-ML, the combination of the direct and phonon-assisted tunneling mechanisms is fitted with the experimental result, which is consistent with the conclusion from V. Osinniy et al. [55]. For sample GSRO-ML, instead of the direct and phonon-assisted tunneling mechanisms, the two-diode mode is more appropriate to describe its forward current [56]. The current increases linearly with the bias in low bias region (region I, $V < 0.3$ V), exponentially with the bias in the intermediate bias region (region II, V = 0.3~1.5 V), and deviates from exponential behavior in the higher bias region (region III, $V > 1.5$ V). The clearly distinct conductive regions indicate a corresponding change in the dominating carrier transport mechanism. The two-diode mode had also been observed by S. Park et al. from the heavily P-doped Si QD thin films integrated with B-doped Si wafer [56]. The linear relationship between log I and log V in region I indicates the presence of a parallel current path due to a shunt resistor in parallel to the junction. In region II, a feature of the current exponentially increasing with bias is dominated by the space-charge region recombination mechanism. In region III, the cause of the I-V characteristics deviated from the ideal behavior is still uncertain but possibly due to the trapping states distribution. From Fig. 3-8(b), the improved PV properties observed in sample GSRO-ML represent that the space-charge region recombination mechanism is a more suitable carrier transport mechanism for SC application integrating Si QDs owing to the largely enhanced tunneling probability or the mini-band formation resulting from the quite close distribution of Si QDs in sample GSRO-ML [28, 30, 52]. Besides, since the Si QD thin film utilizing the heavily-doped [SiO_2/SRO]-ML structure can possess a better carrier transport property than the generally-doped one [21], we believe it is most feasible to achieve even better PV properties by using a heavily-doped GSRO-ML structure.

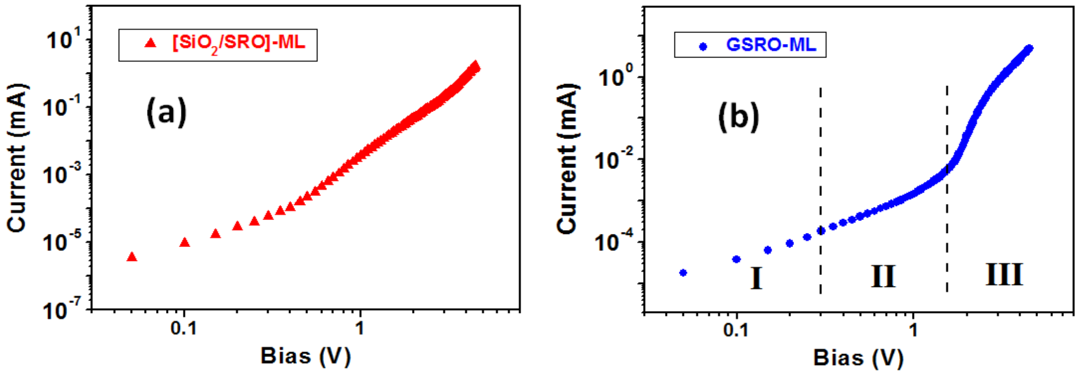

Fig. 3-9: Dark forward I-V curves in log-log scale for samples (a) [SiO_2/SRO]-ML and (b) GSRO-ML.

The temperature-dependent dark I-V curves of samples [SiO_2/SRO]-ML and GSRO-ML are also examined and shown as Fig. 3-10 for further confirmation of the carrier transport mechanism. Two kinds of transport mechanisms in sample [SiO_2/SRO]-ML are gradually discriminated by increasing temperature, as shown in Fig. 3-10(a). Such temperature-dependent I-V characteristics are resulted from the direct and phonon-assisted tunneling mechanisms [55, 57]. For sample GSRO-ML, the temperature-dependent I-V curves in region II can be well-fitted in a standard diode equation, $I(V,T)=I_s(T)[\exp(BV)-1]$, where I_s is the reverse saturation current and parameter B is a coefficient dependent or independent on temperature decided by the dominant carrier transport mechanism [56]. The linearly temperature-dependent B confirms that the carrier transport mechanism is dominated by the space-charge region recombination mechanism [56]. The temperature-dependent ideality factors are larger than 2 due to the trapping defect states or the current crowding effect usually observed in the Si nano-structured thin films [58, 59]. Therefore, from the temperature-dependent I-V measurements, we confirm the different carrier transport mechanisms between samples [SiO_2/SRO]-ML and GSRO-ML. The super-high density Si QD thin film achieved using the proposed GSRO-ML structure can truly improve the carrier transport efficiency through the space-charge region recombination mechanism.

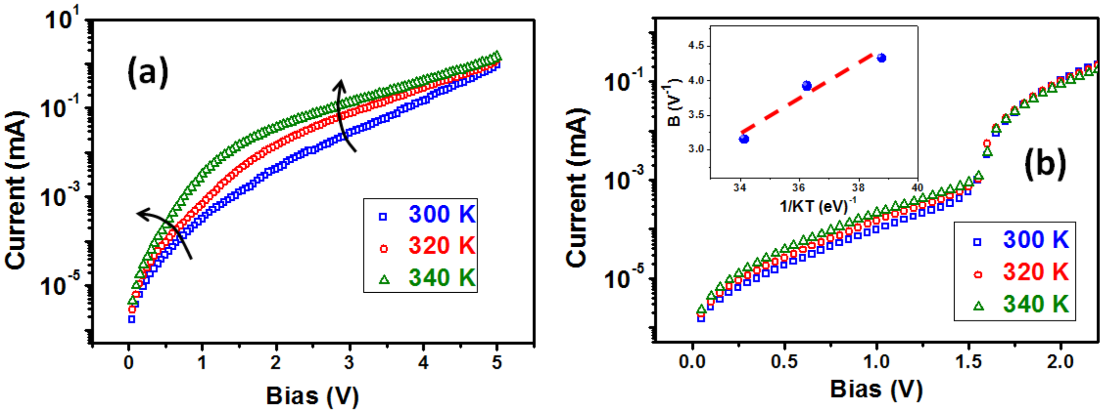

Fig. 3-10: Temperature-dependent dark I-V curves of samples (a) [SiO_2/SRO]-ML and (b) GSRO-ML. Inset of (b) shows the parameter B in region II.

3-5 Summary

In chapter 3, we propose a novel deposition structure, GSRO-ML, to realize Si QD thin films with enhanced PV properties. By using a GSRO-ML structure, the super-high density Si QD thin film with good QD size control is demonstrated. Compared with a [SiO_2/SRO]-ML structure, sample GSRO-ML has improved carrier transport efficiency and larger optical absorption coefficient resulted from the formation of QDs with significantly higher density. The over 10 times better optical absorption means the required film thickness for SC application can be greatly reduced. As a result, considerable enhancements on electro-optical properties including the rectification, I_{SC}, and V_{OC} are obtained. Besides, instead of the combination of the direct and phonon-assisted tunneling mechanisms as observed in sample [SiO_2/SRO]-ML, the two-diode mode is found in sample GSRO-ML even though only a generally-doped concentration is used. Therefore, the high-efficiency Si-based SCs integrating Si QDs can be most definitely expected using this GSRO-ML structure.

Chapter 4

Si QD Thin Films Utilizing ZnO Matrix Material

In chapter 4, in order to develop a novel Si QD's matrix material, ZnO, the [ZnO/Si] multilayer (ML) thin films under different annealing process were fabricated since the annealing condition can obviously influence the properties of Si QDs and ZnO matrix. The nano-structural, optical, and electrical properties of the Si QD embedded ZnO thin films were examined and discussed.

4-1 [ZnO/Si] Multilayer Thin Films Annealed by Rapid Thermal Annealing

4-1.1 Sample Fabrication

In section 4-1, the [ZnO/Si] ML thin films with 24 bilayers were deposited on p-type Si(100) wafers or fused quartzes at room-temperature by radio-frequency (RF) magnetron sputtering method. The sputtering power of Si (P_{Si}) is varied from 25 (S25) to 110 W (S110) while that of ZnO was fixed at 75 W. The effective thicknesses of each ZnO and Si thin-layers were fixed at 5 and 3 nm, respectively. After deposition, the [ZnO/Si] ML thin films were annealed by a rapid thermal annealing (RTA) process at 1000℃ for 50 seconds in N_2 environment.

4-1.2 Nano-Crystalline Properties

To confirm the nano-crystalline Si (nc-Si) QDs formation, Raman spectra measurements, a well-known and credible technique for examining the nc-Si properties [47, 60], were performed. Fig. 4-1(a) shows the Raman spectra of the annealed [ZnO/Si] ML thin films under different P_{Si} and its inset shows the curve-fitting result of Raman spectrum for sample S110. The fitting curve, which is decomposed into four components with peaks located at 436.1, 480.0, 508.3, and 519.7 cm^{-1}, shows an excellent match with the measured data. The peaks at 480.0, 508.3, and 519.7 cm^{-1} are usually observed in the nc-Si QD, and they are contributed from the transverse-optical (TO) modes of Si-Si vibrations in the amorphous (a-Si), intermediate (i-Si), and nc-Si phases of Si, where the i-Si phase is caused by grain boundaries or smaller crystallites [47]. The full-width at half-maximum (FWHM) of nc-Si phase is 7.4 cm^{-1}, corresponding to nc-Si size about 4 nm [60]. The peak at 436.1 cm^{-1} comes from the E_2(high) mode of ZnO. The lower peak position than 439 cm^{-1} of bulk ZnO is attributed to the presence of intrinsic defects in the ZnO nano-clusters [61]. The peak near 520 cm^{-1} is not observed in sample S25 and significantly increases from sample S75 to S110. Besides, sample S110 shows not only the largest Si crystalline intensity but also a great Si crystal volume fraction (f_c) of 88%, where $f_{c\text{-}Si}$ is estimated from the sum of the integrated intensities of nc-Si and i-Si phases divided by the total sum of the integrated intensities of nc-Si, i-Si, and a-Si phases $((I_{i\text{-}Si}+I_{nc\text{-}Si})/(I_{a\text{-}Si}+I_{i\text{-}Si}+I_{nc\text{-}Si})\times 100\%)$ [62].

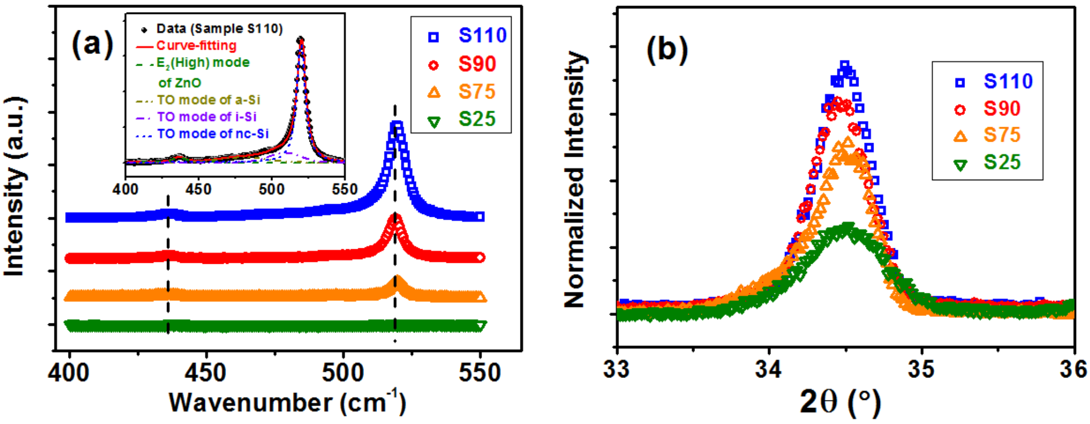

Fig. 4-1: (a) Raman spectra and (b) XRD patterns of the annealed [ZnO/Si] ML thin films under different P_{Si}. Inset of (a) shows the curve-fitting result of Raman spectrum for sample S110.

The crystalline property of ZnO matrix has strong influences on the optical and electrical properties of ZnO thin films [34]. Fig. 4-1(b) shows the X-ray Diffraction (XRD) patterns of the annealed [ZnO/Si] ML thin films under different P_{Si} for the examination of the c-axis (0002) preferred orientation of ZnO matrix. The [ZnO/Si] ML thin films exhibit a narrower FWHM and higher intensity when increasing P_{Si}. This means a better crystallization of ZnO matrix can be obtained with a higher P_{Si}. Hence, the results in Raman spectra and XRD patterns indicate that a high enough P_{Si} is necessary for the formation of nc-Si embedded in ZnO matrix and the increased P_{Si} can improve the crystalline properties of both nc-Si and ZnO matrix.

4-1.3 Formation Mechanism

In order to understand the formation mechanism, we analyze the atomic force microscope (AFM) images of the ZnO single-layer with a 5 nm thickness and the [ZnO/Si] single-bilayer under different P_{Si} after deposition, as shown in Fig. 4-2. Significant variations on the surface morphologies are observed. The AFM image of sample S25 shows a smaller root-mean-square (RMS) surface roughness than that of the ZnO single-layer, and the deposited Si layer can be seen as a thin layer-like. However, the AFM images of samples S75, S90, and S110 show larger RMS surface roughnesses than that of ZnO single-layer and clear formation of a-Si nano-clusters. Moreover, the RMS surface roughness increases with increasing P_{Si} and the density of nano-clusters in samples S90 and S110 can be estimated to be 3.1×10^{10} and 1.9×10^{10} cm^{-2}. The similar results are also obtained in the [ZnO/Si] double-bilayers. Since an a-Si nano-film needs a higher crystallization temperature of 1100℃ than that for a-Si nano-clusters [63], the nc-Si is hard to efficiently form in sample S25 during annealing. The more obvious formation of a-Si nano-clusters with increasing P_{Si} indicates that a higher P_{Si} can remarkably assist the sputtered Si atoms gaining more kinetic energy to self-aggregate as a-Si nano-clusters during deposition. Therefore, nc-Si QDs can be formed more easily during annealing. This observation is in good agreement with the Raman results. The peak intensity of the nc-Si is greatly enhanced with increasing P_{Si}. Furthermore, because each ZnO thin-layer is separated by the a-Si thin-layer in sample S25, the crystallization of ZnO matrix is impeded during annealing. Hence, a lower quality of ZnO crystallization is obtained in sample S25.

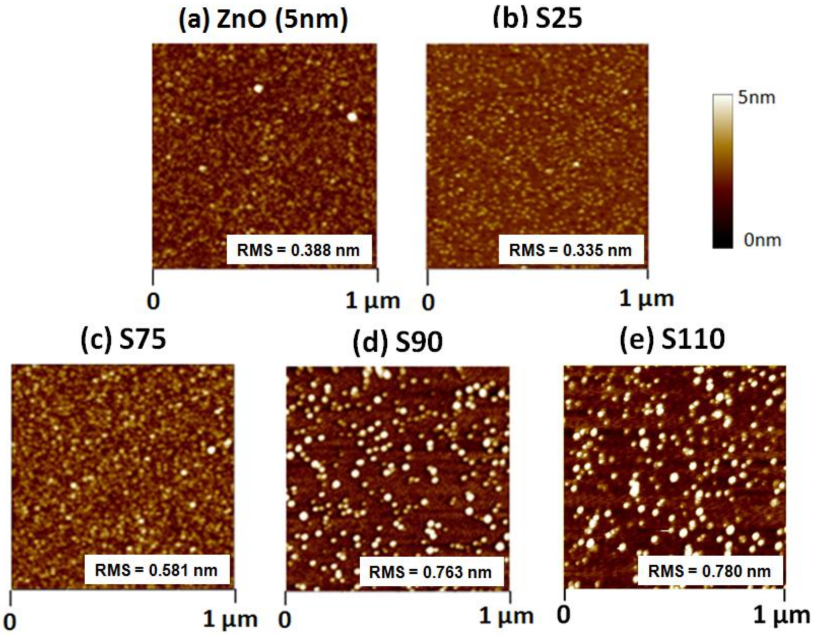

Fig. 4-2: AFM images of (a) the ZnO single-layer with a 5 nm thickness and the [ZnO/Si] single-bilayer thin films under (b) 25, (c) 75, (d) 90, and (e) 110 W of P_{Si} after deposition.

The as-deposited and after-annealing cross-sectional transmission electron microscope (TEM) images of sample S110 are shown in Fig. 4-3. In Figs. 4-3(a) and (b), we can observe the obvious ML structure with a slightly rough morphology and the formation of a-Si nano-clusters with a size distribution of 3~5 nm separated by ZnO thin-layers after deposition. The slightly rough morphology is different from the ML structures using Si-based dielectric materials as matrix [64]. This result is reasonable since ZnO is easy to crystallize during deposition [34]. We can adjust the morphology of each ZnO thin-layer by tuning the ZnO sputtering power or the working pressure during deposition. The observed size distribution of a-Si nano-clusters is highly consistent with the examined height of a-Si nano-clusters in AFM image and the estimated size of nc-Si about 4 nm in Raman spectrum for sample S110, and such size is suitable for various electro-optical devices using the quantum-confinement effect. From Fig. 4-3(c), the ML structure can still be clearly seen after annealing and a high-density of nano-crystalline clusters with a size distribution of 2~6 nm can be observed from the zoom-in HRTEM image shown in Fig. 4-3(d). Combined with the Raman and XRD results, these nano-crystalline clusters are the nc-Si QDs embedded in crystalline ZnO matrix. Therefore, we can conclude that a high P_{Si} can assist the formation of self-aggregated a-Si nano-clusters on ZnO layers during deposition, and such result is advantageous to form the nc-Si QDs embedded in crystalline ZnO matrix during annealing, as illustrated in Fig. 4-4. Thus, we demonstrate that the good crystallization of nc-Si QDs and ZnO matrix can be simultaneously achieved with a high enough P_{Si} for the nc-Si QDs embedded ZnO thin films.

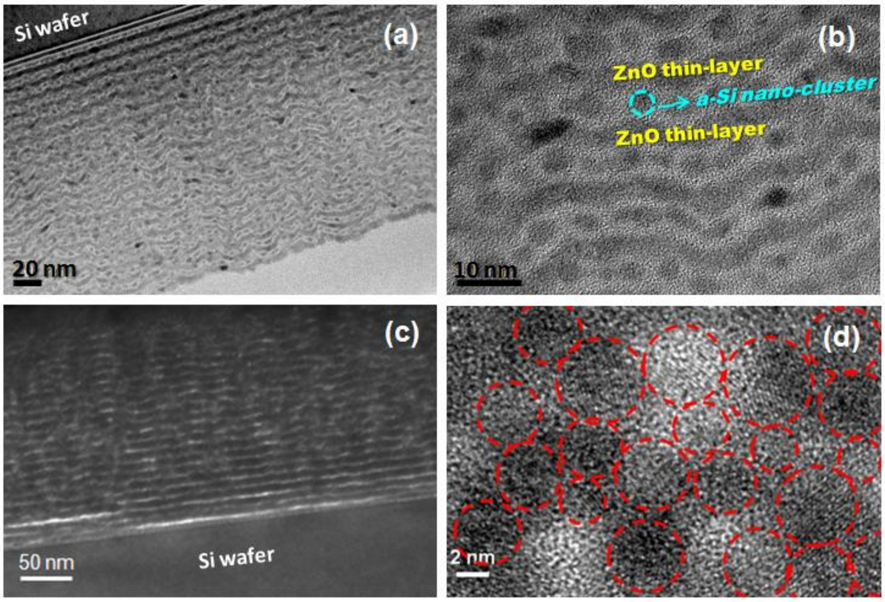

Fig. 4-3: The overall and zoom-in cross-sectional TEM images of the [ZnO/Si] ML thin film. (a) and (b) are as-deposited, and (c) and (d) are after annealing for sample S110.

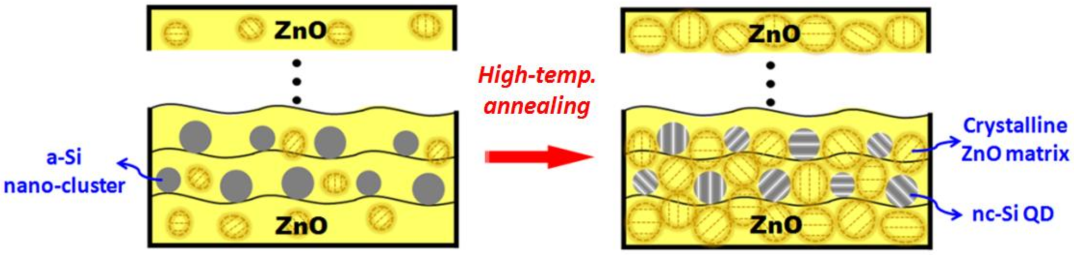

Fig. 4-4: Illustration of the formation of nc-Si QDs embedded in the crystalline ZnO matrix with a high enough P_{Si} by using a [ZnO/Si] ML structure.

4-1.4 Summary of Section 4-1

In section 4-1, we had successfully fabricated the nc-Si QDs embedded in ZnO thin films and demonstrated their formation by using a [ZnO/Si] ML structure and annealing process. The sample with P_{Si} of 110 W shows a large $f_{c\text{-}Si}$ of 88% and a highly uniform size about 4 nm of nc-Si QDs. Our results indicate that an obvious self-aggregation of the sputtered Si atoms as nano-clusters with a high enough P_{Si} during deposition is essential and helpful for the nc-Si QDs formation and the better crystallization of ZnO matrix during annealing. Therefore, we demonstrate the feasibility of fabricating nc-Si QDs embedded in crystalline ZnO thin films.

4-2 [ZnO/Si] ML Thin Films Annealed under a Shorter Duration by Furnace Annealing

In section 4-2, the [ZnO/Si] ML thin films were annealed at a shorter duration by furnace annealing (FA), a slower temperature variation process, for the nc-Si QD embedded ZnO thin films. The sample fabrication and characteristics analyses were investigated and discussed below.

4-2.1 Sample Fabrication

The [ZnO/Si] ML thin films with 20 bilayers were deposited on p-type Si(100) wafers or fused quartzes by sputtering process. The sputtering powers of ZnO and Si were fixed at 75 W and 110 W, and the effective thicknesses of each ZnO and Si layers were fixed at 5 and 3 nm respectively. After deposition, the [ZnO/Si] ML thin films were annealed in N_2 environment for 5 minutes by FA under different T_{ann} from 700℃ (FA-700) to 1000℃ (FA-1000) with 100℃ increment for the investigation on Si QDs formation with high crystallinity.

4-2.2 Nano-Crystalline Properties

Raman spectrum measurement, a reliable technique for examining the crystalline properties of nano-scaled Si materials [47, 60], is utilized to confirm the nc-Si QDs formation in ZnO thin films after FA. The curve-fitting result of Raman spectrum for sample FA-1000 is shown in Fig. 4-5(a). In addition to the transverse optical (TO) modes of Si-Si vibrations in the a-, i-, and nc-Si phases located at 480.0, 504.6, and 513.2 cm^{-1}, which are usually observed in the nc-Si QD thin films [47], the contribution of E_2(high) mode of ZnO matrix located at 436.2 cm^{-1} is also taken into account in this curve-fitting process [61]. The fitting curve composed of these four components shows an excellent match with the experimental data and an obvious nc-Si signal. Raman spectra of the [ZnO/Si] ML thin films under different T_{ann} are shown in Fig. 4-5(b). The intensity of nc-Si significantly increases with increasing T_{ann} while that of a-Si decreases. The parameters of the curve-fitting results in Raman spectra for nc-Si, and the calculated $f_{c\text{-}Si}$ are listed in Table 4-1. Sample FA-1000 shows not only the largest integrated intensity but also the narrowest FWHM for nc-Si. The narrower FWHM means a larger Si crystal size, and the corresponding size in sample FA-1000 can be estimated to be about 3 nm in diameter [48, 60]. In addition, the largest $f_{c\text{-}Si}$ of 76.8 % is obtained from sample FA-1000. Hence, our results show that T_{ann} has a great effect on the crystallization of a-Si nano-clusters. Since the crystalline property of ZnO matrix has strong influences on the optical and electrical properties of the ZnO thin films [65], the XRD pattern of sample FA-1000 is examined and shown as inset of Fig. 4-5(b). The ZnO(0002) orientation located at 34.45° is clearly observed in sample FA-1000. In other words, the high crystallinity of Si nano-clusters can form in the crystalline ZnO matrix by utilizing a [ZnO/Si] ML deposition structure with T_{ann} of 1000℃ for a short annealing duration time of 5 minutes by FA.

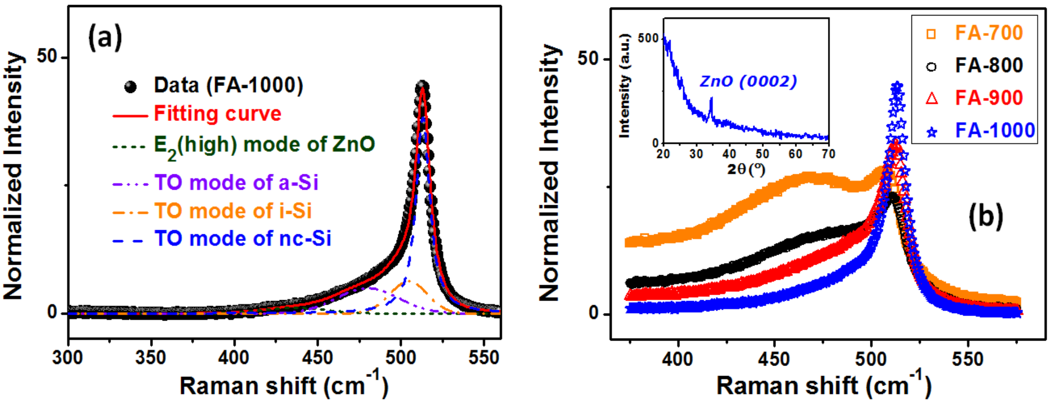

Fig. 4-5: (a) The curve-fitting result of Raman spectrum for sample FA-1000. (b) Raman spectra of the [ZnO/Si] ML thin films under different T_{ann}. Inset shows the XRD pattern for sample FA-1000.

Table 4-1: Parameters of the curve-fitting results in Raman spectra for nc-Si phase and the calculated crystalline volume fractions of Si ($f_{c\text{-}Si}$) under different T_{ann}.

Sample ID	**TO mode of nc-Si phase**			**Crystalline volume fraction of Si ($f_{c\text{-}Si}$) (%)**
	Peak position (cm^{-1})	**FWHM (cm^{-1})**	**Integrated Intensity (a.u.)**	
FA-700	/	/	/	25.0
FA-800	511.8	12.0	107.4	32.8
FA-900	512.6	11.9	338.5	58.9
FA-1000	513.2	10.0	583.2	76.8

Figs. 4-6(a) and (b) shows the cross-sectional TEM images of the as-deposited and 1000℃-annealed [ZnO/Si] ML thin films for further understanding of the nano-structural properties. The [ZnO/Si] ML structure can be clearly observed after deposition from inset of Fig. 4-6(a) and is well maintained after annealing shown as inset of Fig. 4-6(b). The nano-scaled rough morphology different from that of the ML structures using Si-based dielectric materials as matrix [64] originates from the slight crystallization of ZnO thin-layers during deposition [66]. From Fig. 4-6(a), we can see the formations of a-Si nano-clusters with a size distribution of 3~5 nm separated by ZnO thin-layers after deposition. And a large number of nano-crystalline clusters marked in red dashed circles are found after annealing from Fig. 4-6(b). Combined with the Raman and XRD results, these nano-crystalline clusters are composed of the nc-Si QDs embedded in the crystalline ZnO matrix. Moreover, the observed size distribution of a-Si nano-clusters is well consistent with the examined height of nano-clusters in AFM image and the estimated average crystalline size of Si in Raman spectrum for sample FA-1000, and such size is proper to produce the quantum confinement effect for electro-optical devices integrating nc-Si QDs [16, 24, 67]. Therefore, we verify that the ZnO thin film with the suitable size of nc-Si QDs can be realized after FA.

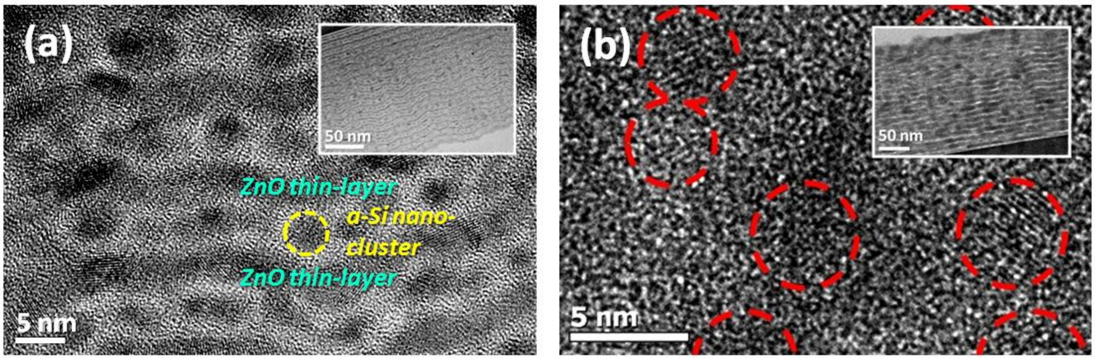

Fig. 4-6: Cross-sectional TEM images of the (a) as-deposited and (b) 1000℃-annealed (sample FA-1000) [ZnO/Si] ML thin films. Insets show the corresponding overall images.

4-2.3 Optical Properties and Sub-bandgap Formation

The optical properties of the ZnO thin film with nc-Si QDs are also investigated and discussed. Fig. 4-7 shows the PL spectra of sample FA-1000 and pure ZnO thin film with equal ZnO thickness of 105 nm under an identical annealing condition as a reference sample. The visible PL emission (PL$_{\mathrm{VIS}}$) with a wide FWHM is observed in the pure ZnO thin film. Similar results have been reported and shown this PL$_{\mathrm{VIS}}$ is from the contribution of the native defects in ZnO, which can be efficiently controlled by various post-annealing methods [68, 69]. Hence, the increased PL$_{\mathrm{VIS}}$ in sample FA-1000 can be mainly inferred from the higher native defect density in ZnO matrix since it has a smaller crystalline size than that in pure ZnO thin film. In addition to the increased PL$_{\mathrm{VIS}}$, the PL spectrum accompanies increased near-infrared emission (PL$_{\mathrm{NIR}}$) and an unusual peak (PL$_{\mathrm{unusual}}$) located at 685 nm (1.81 eV), which have not been reported in pure or doped ZnO materials [68, 69], for sample FA-1000. This PL$_{\mathrm{unusual}}$ may be contributed from the nc-Si QDs embedded in the ZnO matrix with wide bandgap. Because of the quantum confinement effect [53], an effective bandgap of nc-Si QD larger than the bandgap of bulk crystalline-Si (1.12 eV) is formed. Therefore, the obvious PL$_{\mathrm{NIR}}$ may be primarily resulted from the interface states between nc-Si QDs and ZnO matrix. Similar results have also been observed for nc-Si

QDs embedded in SiO_2 matrix [50, 70]. For the T_{ann} lower than 1000℃, the PL_{VIS} and PL_{NIR} clearly dominate the PL emission properties and no obvious $PL_{unusual}$ peak is observed. This indicates the native defects in ZnO matrix and the interface states between nc-Si QDs and ZnO matrix are excessively formed because of the lower crystal quality of Si QDs and ZnO matrix under lower T_{ann}.

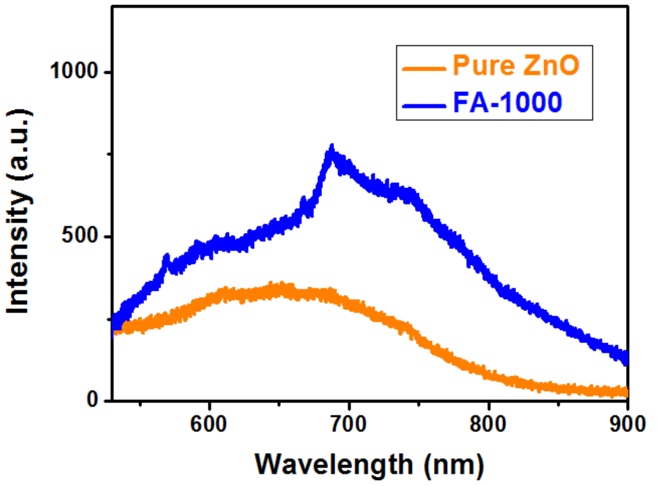

Fig. 4-7: PL spectra of sample FA-1000 and pure ZnO thin film after annealing at 1000℃.

To confirm the contributions of nc-Si QDs in PL spectrum and their impact on the optical properties of ZnO thin film with nc-Si QDs, the ultraviolet/visible/near-infrared (UV-VIS-NIR) spectra were examined. Figs. 4-8(a) and (b) show the light transmission, reflection, and absorption spectra of sample FA-1000 and pure ZnO thin film for comparison. For sample FA-1000, a high transmittance (T) in the long-wavelength (long-λ) range of 650 to 1000 nm and a high absorption in the short-λ range under 380 nm similar to general ZnO thin film are observed, and the T is higher than that of pure ZnO thin film owing to the reduced reflectance (R). The average R of sample FA-1000 (~9.5%) is significantly lower than that of pure ZnO thin film (~22.0%) in the measured λ range of 320~1000 nm. The sharp R peak occurred at the absorption edge of 380 nm in pure ZnO thin film originates from excitonic resonant emission, which is usually observed in the high-temperature annealed or epitaxial ZnO thin films [71, 72]. The T of sample FA-1000 obviously reduces with decreasing λ in the middle-λ range of 380 to 650 nm. At the same time, an increased absorbance (A) compared to pure ZnO thin film is observed in the corresponding λ range. The increase of light absorption causes the decrease of light transmission in the middle-λ range because of the presnece of nc-Si QDs. To further verify the contributions of nc-Si QDs, Fig. 4-8(c) shows the PL spectrum and Tauc plot for the indirect allowed transition since the optical transition process in nc-Si QD system is dominated by a phonon-assisted mechanism [53]. The average indirect optical bandgap ($E_{g,opt.}$) can be evaluated by linear extrapolating the interception at the energy axis ($\alpha h\nu = 0$) from the plot of $(\alpha h\nu)^{1/2}$ as a function of incident photon energy ($h\nu$), where α is the optical absorption coefficient. The evaluated indirect $E_{g,opt}$ for sample FA-1000 is 1.86 eV, which quite matches the $PL_{unusual}$ peak energy (1.81 eV). Thus, we show that the nc-Si QDs embedded in ZnO matrix induce a sub-bandgap formation and in turn contribute the $PL_{unusual}$ and significant light absorption enhancement in the middle-λ range. Other than Si-based dielectric materials [8, 73], we successfully demonstrate the ability of sub-bandgap formation in ZnO material utilizing nc-Si QDs. Moreover, the $E_{g,opt.}$ of ZnO matrix can be obtained from the Tauc plot for direct allowed transition shown as inset of Fig. 4-8(c). The bandgap of 3.34 eV well agrees with that of general ZnO thin films [74]. These measurement results indicate that the ZnO matrix in sample FA-1000 still reserves its essential and advantageous optical properties even though the nc-Si QDs are embedded [74]. The realization of high crystallinity of Si QDs embedded in the crystalline ZnO matrix with a meaningful sub-bandgap provides a new and potential composite material for the development of future electro-optical devices.

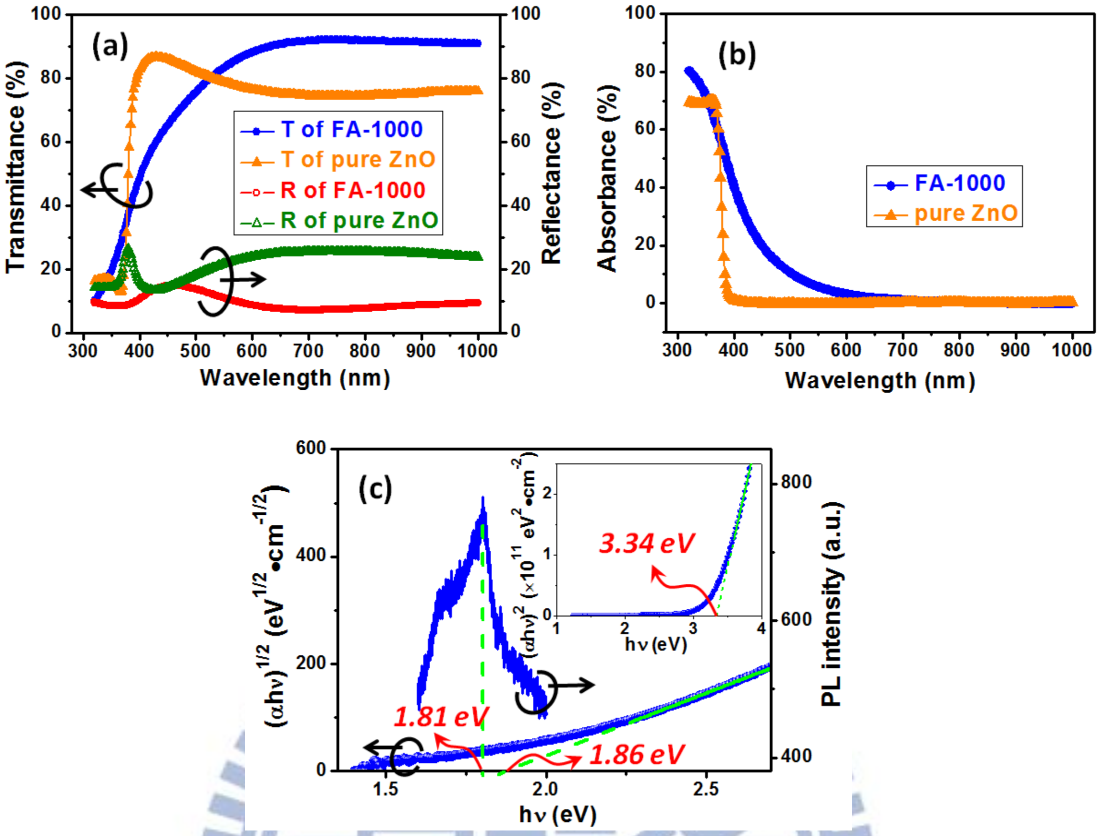

Fig. 4-8: (a) Transmission, reflection, and (b) absorption spectra of sample FA-1000 and pure ZnO thin film on quartzes. (c) PL spectrum and Tauc plot for indirect allowed transition of sample FA-1000. Inset shows the Tauc plot for direct allowed transition of sample FA-1000.

4-2.4 Summary of Section 4-2

In section 4-2, we had successfully fabricated the nc-Si QD embedded ZnO thin films under a shorter duration time of 5 minutes by FA. Our results indicate that 1000℃ of T_{ann} can result in highest crystallinity of Si QDs embedded in crystalline ZnO matrix. Though embedded with nc-Si QDs, the optical properties of ZnO thin film can be preserved in the long- and short-λ ranges. In the middle-λ range, the significantly enhanced light absorption owing to nc-Si QDs is obtained. In addition, an optical sub-bandgap of 1.86 eV closes to the unusual PL emission peak located at 1.81 eV is observed in sample FA-1000. These results represent the sub-bandgap formation in ZnO thin film by utilizing nc-Si QDs while maintaining the essential optical properties of ZnO matrix.

4-3 [ZnO/Si] ML Thin Films Annealed under a Longer Duration by Furnace Annealing

In section 4-3, the [ZnO/Si] ML thin films annealed at a longer duration were performed by FA, and the sample fabrication and experiment results are shown and discussed below.

4-3.1 Sample Fabrication

The [ZnO/Si] ML thin films with 20 bilayers were deposited on p-type Si(100) wafers or fused quartzes by sputtering. The sputtering powers of ZnO and Si were fixed at 75 W and 110 W, and the effective thicknesses of each ZnO and Si layer were fixed at 5 and 3 nm respectively. After deposition, the [ZnO/Si] ML thin films were annealed at 500, 600, 700, and 800℃ for 30 minutes in N_2 environment by FA.

4-3.2 Nano-Crystalline Properties

In order to investigate the crystalline properties of the Si QDs embedded in ZnO thin films annealed at a longer duration under different T_{ann}, Raman spectra were measured and shown in Fig. 4-9. The corresponding $f_{c\text{-}Si}$ values obtained from fitting the curves are shown as inset of Fig. 4-9 [47]. The nc-Si phase is formed in ZnO matrix and significantly increased by increasing T_{ann} when T_{ann} is higher than 600℃. It indicates the higher T_{ann} under a longer duration can largely enhance the crystalline quality of Si QDs embedded in ZnO matrix. Besides, the required T_{ann} for the significant nc-Si formation, using a [ZnO/Si] ML structure, can be obviously decreased by increasing the annealing duration.

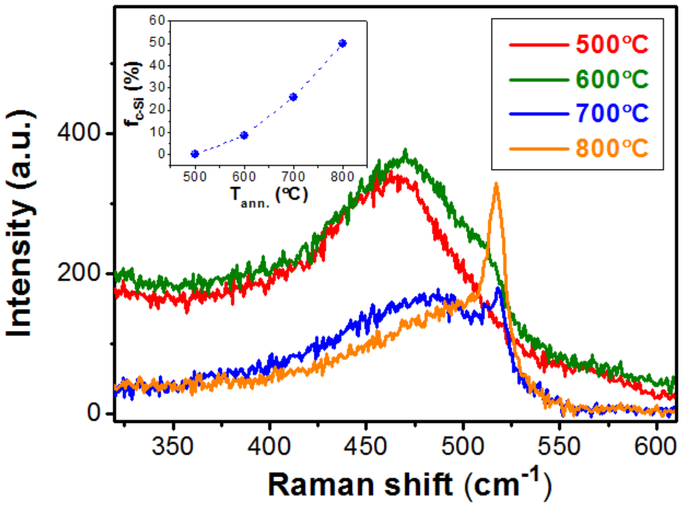

Fig. 4-9: Raman spectra of the Si QD embedded ZnO thin films under different T_{ann}. Inset shows the corresponding crystalline volume fractions of Si ($f_{c\text{-}Si}$).

Since the crystalline properties of ZnO matrix can influence its optical and electrical properties [65], the XRD patterns of the Si QD embedded ZnO thin films annealed at different temperatures were examined and shown in Fig. 4-10(a), fine-scanned from 30° to 40°. A main diffraction signal is observed at ~34.5° for all the samples. As shown in Fig. 4-10(b) and its inset, this signal can be decomposed into two components in Gaussian form with peaks located at ~34.3° and ~36.3°, which are contributed from (002) and (101) orientations of ZnO [75]. In Fig. 4-10(a), the crystallization intensity of ZnO matrix is slightly reduced when increasing T_{ann}. This may due to the increased interior film stress resulted from phase transformation of a- to nc-Si QDs. From the results of Raman and XRD measurements, we show that the nc-Si QDs embedded in crystalline ZnO matrix can be achieved by a T_{ann} higher than 600℃.

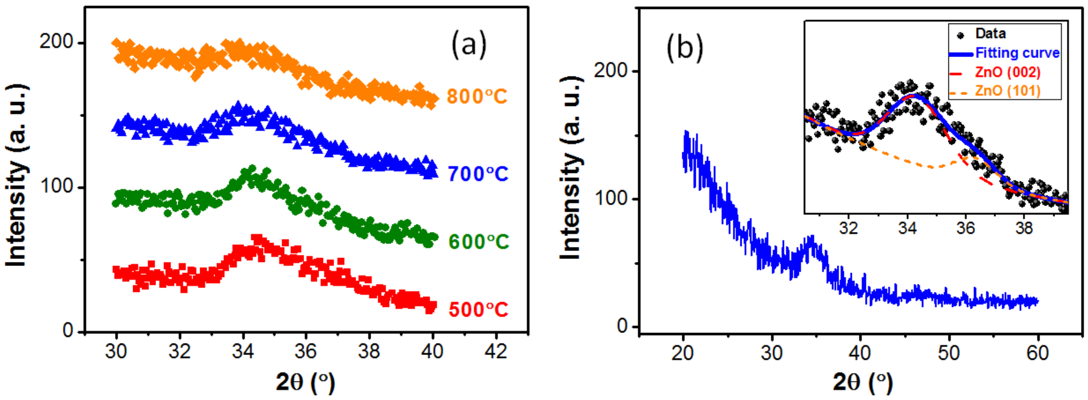

Fig. 4-10: (a) XRD patterns fine-scanned from 30° to 40° of the Si QD embedded ZnO thin films under different T_{ann}. (b) Full XRD pattern of the Si QD embedded ZnO thin film annealed at 700℃. Inset of (b) shows the curve-fitting result for the main diffraction signal.

4-3.3 Optical Transmittance Improvement

The optical transmittance spectra of the Si QD embedded ZnO thin films under different T_{ann} are shown in Fig. 4-11. The transmittance in the long-λ range (> 600 nm) clearly increases when increasing T_{ann}. Since higher T_{ann} can obviously enhance the crystallization of Si QDs, the improved optical transmittance in the long-λ range can be attributed to the decreased absorbance from a-Si QDs due to the increased $f_{c\text{-}Si}$ of Si QDs [8]. It is worthy to note that high transmittance of ~90% in the long-λ range under a T_{ann} higher than 700℃ can be achieved and is close to those using the traditional matrix materials [8]. From above results, it is clear that better crystallization of Si QDs in ZnO matrix is required to decrease the absorption from a-Si QDs and thus efficiently reduce the optical loss in the long-λ range for better optoelectronic device performance. We find that a high enough $f_{c\text{-}Si}$ for the Si QDs embedded ZnO thin film is critical to significantly improve the optical properties.

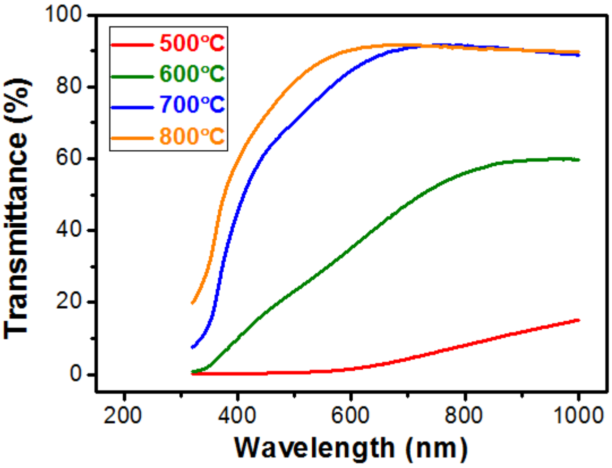

Fig. 4-11: Optical transmittance spectra of the Si QD embedded ZnO thin films under different T_{ann}.

4-3.4 Local Film Prominences

The images of the Si QD embedded ZnO thin films after annealing were examined by SEM. The local film prominences are observed when T_{ann} is higher than 600℃. Fig. 4-12(a) shows the cross-sectional SEM image of sample annealed at 700℃. The local film prominence density and diameter in average are estimated and shown in Fig. 4-12(b). The prominence density increases from 5.5 to 7.6 ones per $10\times10\ \mu m^2$ when increasing T_{ann} from 600 to 800℃ with close average diameter of ~2 μm. According to Raman spectra, the phase transformation of a- to nc-Si QDs happens when T_{ann} is larger 600℃ and $f_{c\text{-}Si}$ also increases with increasing T_{ann} from 600 to 800℃. This strong correlation between $f_{c\text{-}Si}$ and prominence density means the volume variation from the phase transformation of a- to nc-Si QDs embedded in ZnO matrix during annealing can produce an interior film stress and lead to the occurrence of local film prominences. Moreover, the local film prominence density of the annealed thin films by using FA with lower temperature and longer duration can be significantly improved than that with higher annealing temperature and shorter duration or the RTA process.

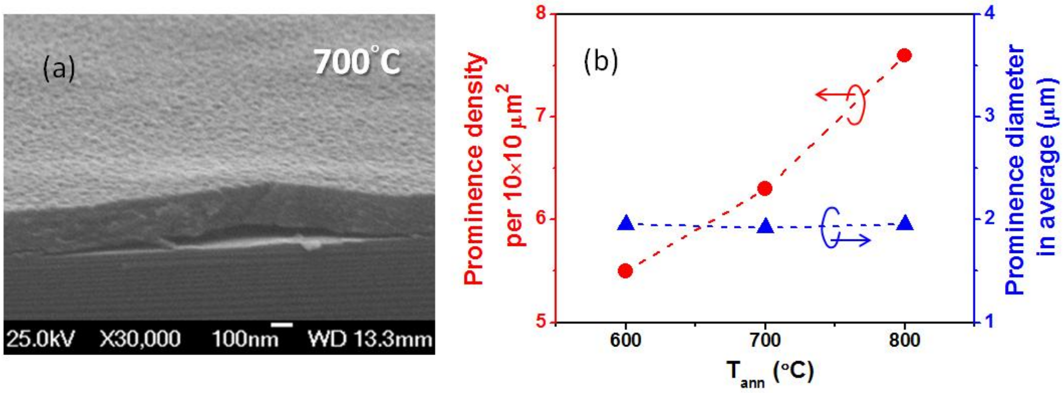

Fig. 4-12: (a) Cross-sectional SEM image and (b) local film prominence density and diameter in average for the Si QD embedded ZnO thin films after annealing.

4-3.5 Electrical Properties and Carrier Transport Mechanism

To understand the electrical properties of the Si QD embedded ZnO thin films, the resistivity (ρ) is calculated from the slope of I-V curve under a high forward bias region of 4~5 V. When increasing T_{ann}, the ρ can be reduced by the improved crystalline quality of Si QDs but also raised by the increased film prominence density and degraded crystalline quality of ZnO matrix. Fig. 4-13(a) shows the obtained ρ under different T_{ann}, which slightly increases when increasing T_{ann} from 500 to 700°C but still keeps at a low resistivity of ~10^4 Ω-cm, significantly lower than that (~10^8 Ω-cm) of the intrinsic Si QDs embedded in SiO_2 matrix [20, 76]. It is evident that using ZnO as matrix can overcome the issue of highly-resistive nature of the traditional Si-based dielectric matrix materials, and 10^4 times improvement of ρ is obtained. The ρ largely increases for sample annealed at 800°C, which may resulted from the interior film stress and excess film prominences produced during annealing. Hence, we can conclude that annealing at 700°C is a more suitable annealing condition to have better crystallization of Si QDs in crystalline ZnO matrix, low ρ, and high transmittance in the long-λ range. The logarithmic I-V curve of sample annealed at 700°C is shown in Fig. 4-13(b), and its inset shows the linear I-V curves of the Si QD embedded in ZnO and SiO_2 thin films. It clearly exhibits not only a good rectification ratio of 3.4×10^3 at ±5V but also a low turn-on voltage (V_t) of 0.48 V, which agrees with the reported results of the n-ZnO/p-Si heterojunction (HJ) diode [77, 78]. Besides, the V_t of using ZnO matrix is also clearly lower than that of using SiO_2 matrix. Hence, even though the Si QDs are embedded in ZnO matrix, we show the fabricated ZnO thin film on p-Si can still possess good p-n HJ diode behavior with large rectification ratio and low V_t.

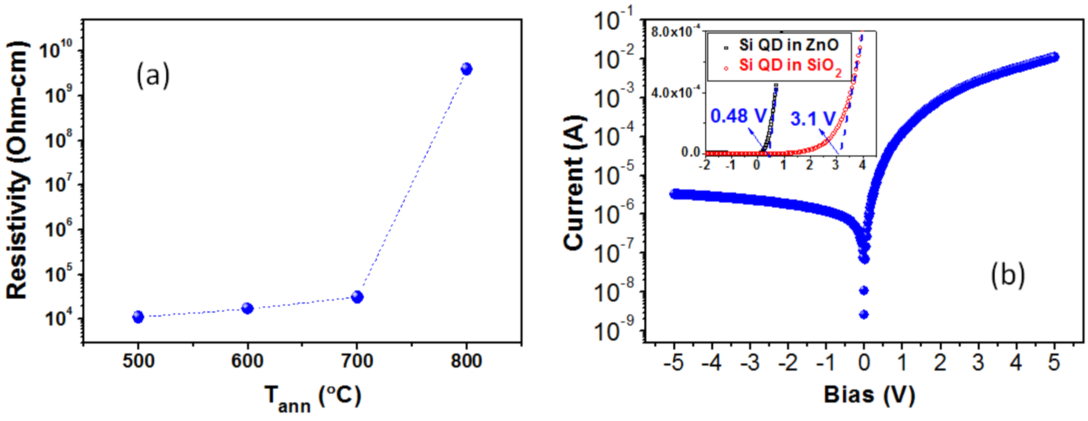

Fig. 4-13: (a) Resistivity of the Si QD embedded ZnO thin films under different T_{ann}. (b) Logarithmic I-V curve of sample annealed at 700°C. Inset of (b) shows the linear I-V curves of the Si QD embedded in ZnO and SiO_2 thin films.

To investigate the carrier transport mechanism, the temperature-dependent forward I-V curves of sample annealed at 700°C are examined and shown in Fig. 4-14(a). The I-V curves exhibit the typical temperature dependence of a p-n junction diode. The current clearly increases as we raise the measurement temperature (T_{meas}). In the low bias region (smaller than ~0.5 V), the currents can be well-fitted to be proportional to $\sim V^{1.2}$ for different T_{meas}, which slightly deviates from the ohmic behavior. This means the surface states and/or an inherent insulating SiO_2 thin layer at the interface of n-ZnO matrix/p-Si substrate has influences on the transport of carriers [79]. In the high bias region (larger than ~0.5 V), the forward currents can be well expressed by $I(V,T)=I_s(T)[\exp(BV)-1]$, where I_s is the reverse saturation current and parameter B is a coefficient dependent or independent on temperature decided by the dominant carrier transport mechanism [79, 80]. The fitted results for parameter B are shown in Fig. 4-14(b), which reveals that the parameter B is almost invariant for different T_{meas}. This independence of T_{meas} indicates the carrier transport is dominated by the multi-step tunneling mechanism, which had been reported by N. Zebbar et al. and Dhananjay et al. for the n-ZnO/p-Si HJ diode [79, 81]. The multi-step tunneling process usually occurs at the HJ region of n-ZnO matrix and p-Si substrate, which is attributed to the recombination of electrons, tunneling from ZnO into the empty gap states in p-Si substrate, and holes, tunneling through the HJ barrier from p-Si substrate to n-ZnO matrix between the empty states [79, 81]. Hence, our results show the carriers in the Si QD embedded ZnO thin film mainly transport via ZnO matrix but not through Si QDs with direct, resonant, or phonon-assisted tunneling mechanisms, as reported for Si QDs embedded in the traditional matrix materials [55, 82]. According to the multi-step tunneling mechanism, the temperature dependence of I_s is given by the relation, $I_s \propto \exp(-E_a/kT)$, where E_a is the activation energy, k is the Boltzmann's constant, and T is the absolute temperature [79, 81]. Fig. 4-14(c) shows the Arrhenius plot of $\ln(I_s)$ versus 1000/T. A linear relationship is clearly observed, which further confirms that the dominated carrier transport process is the multi-step tunneling mechanism [77, 79-81]. The E_a of around 0.37 eV obtained from Arrhenius plot is a little larger than those of the reported n-ZnO/p-Si HJ diodes, which are usually smaller than 0.3 eV [77, 79-81]. This means the thermally-activated carriers are partially contributed from the embedded Si QDs since the intrinsic Si QDs can possess E_a larger than 0.4 eV [20, 83]. Thus, we can conclude that the Si QDs embedded in ZnO matrix also contribute the carriers, and those carriers will partially escape from Si QDs into ZnO matrix and transport inside. The largely improved resistivity suggests that the carriers transporting in ZnO matrix can bring to a much better transport efficiency than those tunneling through barriers in the traditional matrix materials. With the unique carrier transport mechanism and better electrical properties, we deeply believe the Si QD thin films utilizing ZnO as the matrix material have more potential for SCs application.

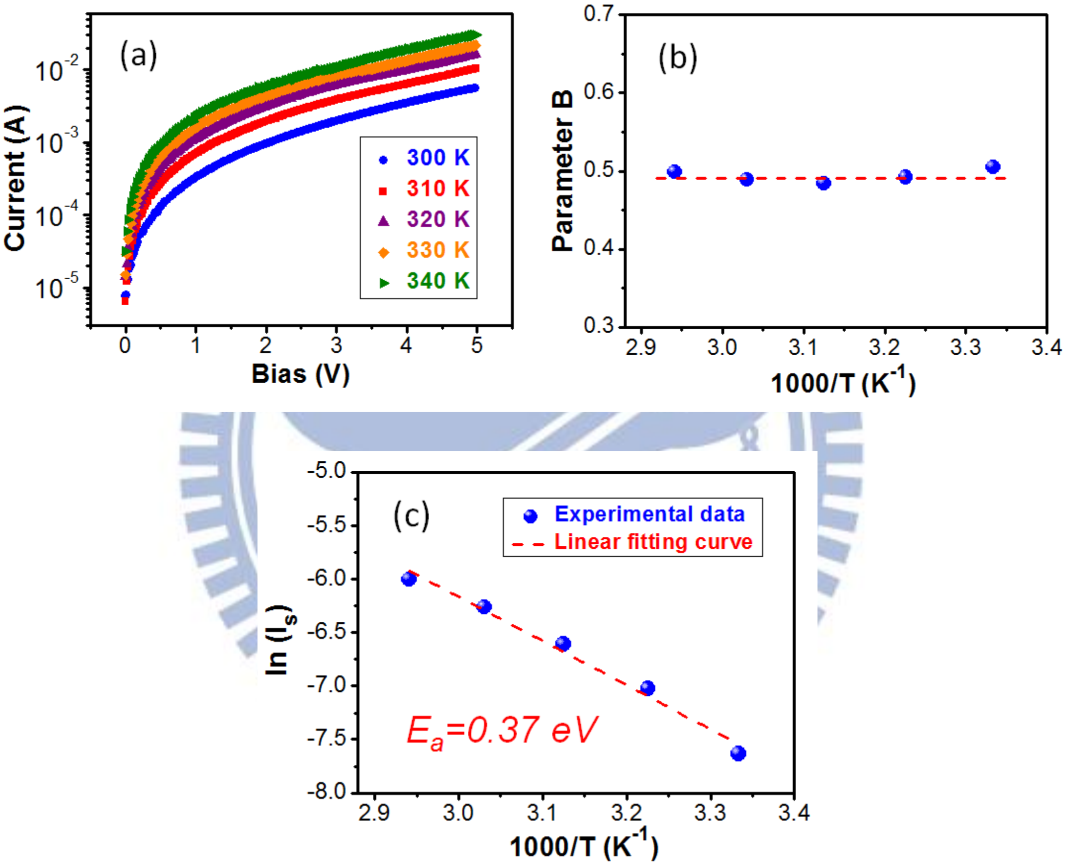

Fig. 4-14: (a) Forward I-V curves for different measurement temperatures, (b) the parameter B, and (c) Arrhenius plot of ln(I_s) versus 1000/T for the Si QD embedded ZnO thin film annealed at 700℃.

4-3.6 Summary of Section 4-3

In section 4-3, we had successfully fabricated the nc-Si QD embedded ZnO thin film under a lower T_{ann} by increasing the annealing duration. Our results indicate the optical transmittance can be largely enhanced by increasing T_{ann} owing to the phase transformation of a- to nc-Si QDs embedded in ZnO matrix, and up to ~90% in the long-λ range under a T_{ann} higher than 700℃ is obtained. The Si QD embedded ZnO thin film annealed at 700℃ exhibits good diode behavior with large rectification ratio of ~10^3 at ±5V and significantly lower resistivity than that using the SiO_2 matrix material (10^4 times improvement). From temperature-dependent I-V curves, we find that the carriers transport mainly via ZnO matrix, not through Si QDs, which is dominated by the multi-step tunneling mechanism as in the n-ZnO/p-Si HJ diode. The unique transport mechanism differing from those using the traditional Si-based dielectric matrix materials can lead to the much better carrier transport efficiency and electrical properties. Therefore, it has been demonstrated that the Si QD thin films using ZnO matrix material have great potential for SCs application.

4-4 Summary

In chapter 4, we had demonstrated the feasibility of embedding nc-Si QDs in crystalline ZnO matrix by sputtering and RTA or FA processes. Our results indicate that an obvious self-aggregation of the sputtered Si atoms as nano-clusters with a high enough P_{Si} during deposition is essential and helpful for the nc-Si QDs formation and the better crystallization of ZnO matrix during annealing. Though embedded with nc-Si QDs, our results confirm the sub-bandgap formation in ZnO thin film by utilizing nc-Si QDs while maintaining the essential optical properties of ZnO matrix. The results also indicate the optical transmittance can be largely enhanced by increasing T_{ann} owing to the phase transformation of a- to nc-Si QDs embedded in ZnO matrix. The Si QD embedded ZnO thin films exhibits good diode behavior with large rectification ratio and significantly lower resistivity than that using the SiO_2 matrix material. Besides, we find that the carriers transport mainly via ZnO matrix, not through Si QDs, which is dominated by the multi-step tunneling mechanism as in the n-ZnO/p-Si HJ diode. The unique transport mechanism differing from those using the traditional Si-based dielectric matrix materials can lead to the much better carrier transport efficiency and electrical properties. Therefore, we believe this novel composite material integrating ZnO thin film with nc-Si QDs has great potential for future SCs and other optoelectronic devices applications.

Chapter 5

Conclusion and Future Works

5-1 Conclusion

In order to efficiently enhance the photovoltaic (PV) properties of the Si QD thin films, we propose to develop the novel Si QD thin films by utilizing a gradient Si-rich oxide multilayer (GSRO-ML) structure for further QD separation reduction and integrating with ZnO matrix material for better carrier transport path.

In the developments of utilizing a GSRO-ML structure, the formation of the super-high density Si QD thin films with good QD size control had been demonstrated. Compared with a [SiO_2/SRO]-ML structure, sample GSRO-ML has the improved carrier transport efficiency and larger optical absorption coefficient resulted from the higher QD density formation. As a result, considerable enhancements on PV properties are obtained. Besides, instead of the combination of the direct and phonon-assisted tunneling mechanisms as observed in sample [SiO_2/SRO]-ML, the two-diode mode is found in sample GSRO-ML even though only a generally-doped concentration is used.

In the developments of integrating ZnO matrix material, we had successfully demonstrated the feasibility of embedding nc-Si QDs in ZnO matrix. Our results indicate that an obvious self-aggregation of the sputtered Si atoms as nano-clusters with a high enough P_{Si} during deposition is essential and helpful for the Si QDs formation and the better crystallization of ZnO matrix during annealing. In the optical properties, the sub-bandgap formation in ZnO thin film by utilizing Si QDs is observed while maintaining the essential optical properties of ZnO matrix. In the electrical properties, we demonstrate that the carriers transport mainly via ZnO matrix, not through Si QDs, which is dominated by the multi-step tunneling mechanism as in the n-ZnO/p-Si HJ diode, and the unique transport mechanism differing from those using the traditional Si-based dielectric matrix materials can lead to much better carrier transport efficiency.

According to these results, we had successfully demonstrated that the proposed novel Si QD thin films, utilizing a GSRO-ML structure and integrating with ZnO matrix material, have great potential for SCs application, and the high-efficiency Si-based SCs integrating Si QDs can be deeply expected by utilizing the novel Si QD thin films in the future.

5-2 Future Works

5-2.1 All Si QD Thin Film Solar Cells Utilizing a GSRO-ML Structure

To obtain the high efficiency Si-based tandem SCs integrating Si QDs, the heavily doped p-i-n all Si QD thin film SCs will be developed by utilizing our proposed GSRO-ML structure, as shown in Fig. 5-1. In the beginning of this development, we develop the heavily B- and P-doped Si QD thin films on n- and p-type Si wafers to confirm the better conditions individually. So far, the heavily B-doped Si QD thin films utilizing a GSRO-ML structure had been successfully fabricated by co-sputtering Si, SiO_2, and B targets. The preliminary cell's performances in the heavily B-doped Si QD thin films were obtained for 432 mV of open-circuit voltage, 25.8 mA/cm^2 of short-circuit current density, 38.7% of fill factor, and 4.37% of conversion efficiency. On the other hand, the heavily P-doped Si QD thin films had also been developed by diffusion process, and so far, the PV properties can be obviously enhanced. Hence, it represents the diffusion process is indeed a feasible method for the development of heavily P-doped Si QD thin films. More details for the preliminary results of the heavily doped Si QD thin films are also shown and discussed in Appendix. In the future, we will further enhance the performances of the B- and P-doped Si QD thin films, and then, the integration of p-i-n Si QD thin films will be developed for the high efficiency all Si QD thin film SCs.

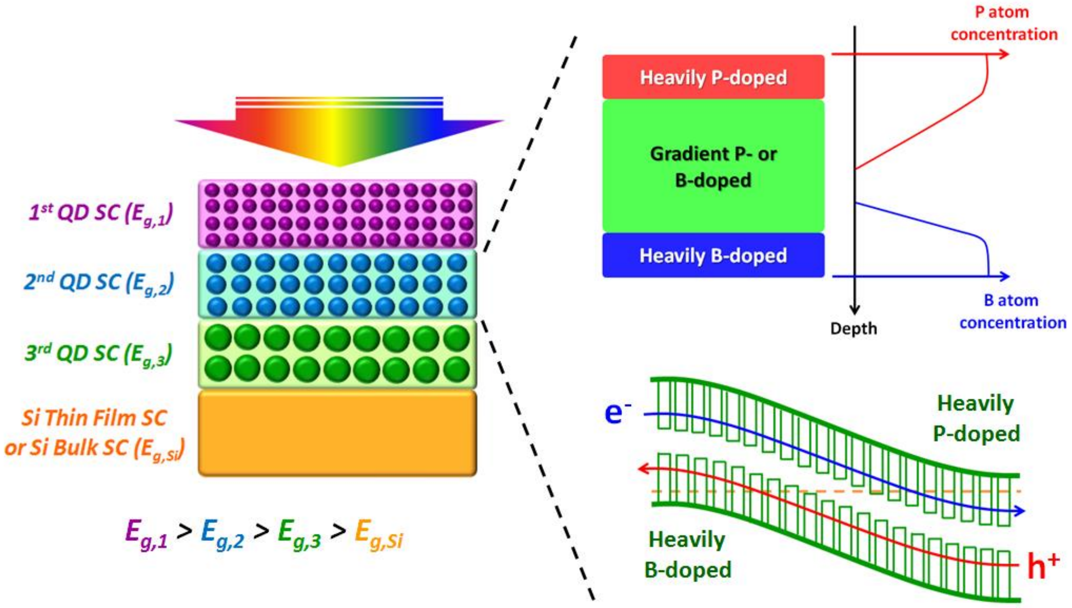

Fig. 5-1: Illustration of device structure and band diagram for the single- and multi-junction Si-based tandem SCs integrating Si QDs.

5-2.2 Si QD Embedded ZnO p-n Homojunction Devices

So far, we had successfully demonstrated the feasibility of embedding nc-Si QDs in ZnO matrix by sputtering and annealing processes. The sub-bandgap formation from Si QDs, the significantly lower resistivity, and the unique carrier transport mechanism had also been confirmed by utilizing ZnO matrix material. In the future works, the Si QD embedded ZnO p-n homo-junction devices will be developed since the homo-junction device’s structure can further enhance the electro-optical properties of the Si QD thin films.

Appendix

Developments of Heavily B- and P-doped Si QD Thin Films

A-1 Heavily B-doped Si QD Thin Films

To further enhance the cells' performances, the heavily B-doped Si QD thin films have been being developed. The heavily B-doped Si QD thin films under different B sputtering powers (P_B) are deposited on n-type Si(100) wafers during co-sputtering process. Fig. A-1 shows the hole concentration, mobility, and resistivity of samples under different P_B, it clearly indicates the B-doped concentration can great influence the electrical properties of the Si QD thin films, and an over-doping concentration will obviously degrade the cell's performances. Therefore, the B-doped concentration is required to be optimized for the good electrical properties of the p-type Si QD thin films.

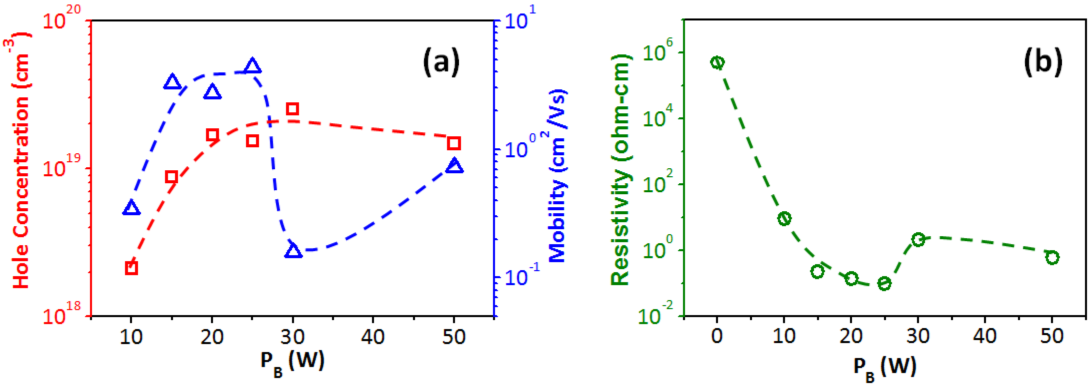

Fig. A-1: (a) Hole concentration and mobility and (b) resistivity of the heavily B-doped Si QD thin films on n-type Si wafers under different B sputtering powers.

Fig. A-2 shows the solar simulator (AM 1.5G) illuminated I-V curves of the heavily B-doped Si QD thin films under different P_B on n-type Si with 0.4×0.5 cm^2 of device's size, and the corresponding parameters, including the open-circuit voltage

(V_{OC}), short-circuit current density (J_{SC}), fill factor (F.F.), and conversion efficiency (η), are shown in Fig. A-3. The V_{OC} is slightly decreased when the P_B is increased from 10 to 25 W, and decreased more when the P_B is increased from 25 to 50 W. However, the J_{SC} and F.F. under P_B of 25 W has the better results for 25.8 mA/cm^2 and 38.7 % individually and lead to the higher η for 4.37 %. In addition, the V_{OC} decreased with increasing B-doped concentration had been demonstrated due to the B atoms over-diffusion during annealing, and it had been efficiently improved by inserting the lowly B-doped GSRO layers with suitable periods. The lower F.F. is considered as more defects in the grain boundaries due to the super-high QD density formation; however, it could be efficiently passivated by a low-temperature annealing process with forming gas. In these results, it clearly represents the cell's performances can be largely enhanced by using a heavily B-doped GSRO-ML structure for the p-type Si QD thin films.

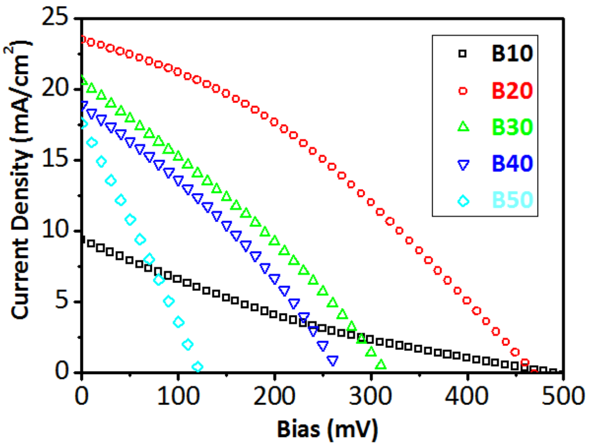

Fig. A-2: Solar simulator (AM 1.5G) illuminated I-V curves of the heavily B-doped Si QD thin films on n-type Si wafers under different B sputtering powers.

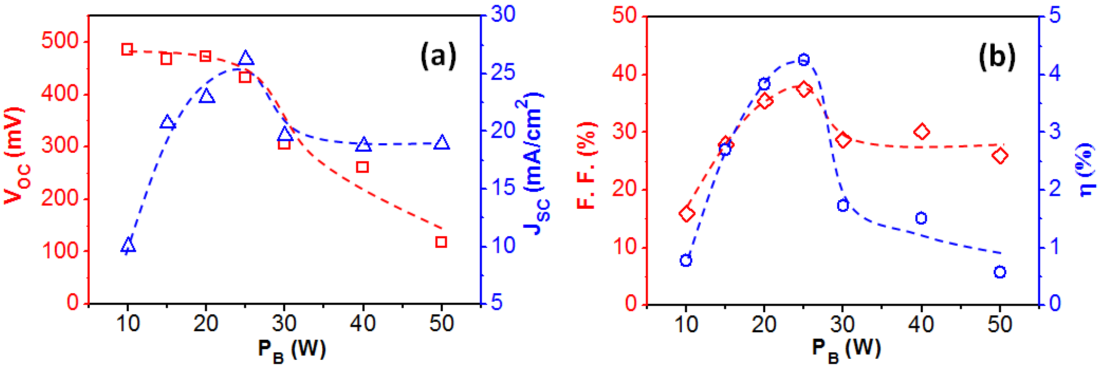

Fig. A-3: Parameters of (a) V_{OC} and J_{SC} and (b) F.F. and η of the heavily B-doped Si QD thin films on n-type Si wafers under different B sputtering powers.

The optical properties of the heavily B-doped Si QD thin films under different nucleation layer (NL) thicknesses were examined for the confirmation of bandgap engineering utilizing a GSRO-ML structure. The thicker NL thickness is expected to form the larger QD size and lead to the smaller effective bandgap due to quantum confinement effect. Fig. A-4 shows the absorption coefficient spectra under different NL thickness and the corresponding optical bandgaps ($E_{g,opt.}$) from Tauc's plot. The red-shift effect in the band-edge absorption and the corresponding $E_{g,opt.}$ is obviously observed while increasing the NL thickness. It represents that the bandgap engineering can be well achieved by tuning the NL thickness in a GSRO-ML structure for the Si QD thin films.

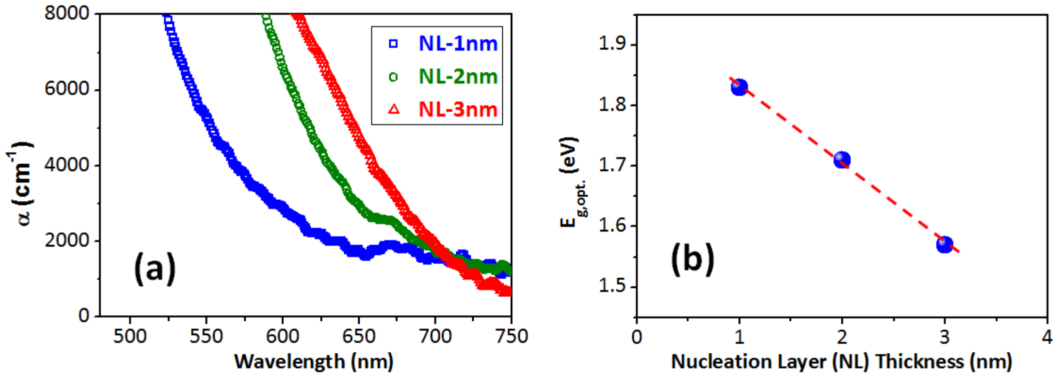

Fig. A-4: (a) Absorption coefficient spectra and (b) the corresponding optical bandgaps of the heavily B-doped Si QD thin films on n-type Si wafers under different nucleation layer thicknesses.

To further confirm the Si QDs' contributions, the internal quantum efficiency (IQE) of the B-doped Si QD thin films under different NL thicknesses on n-type Si were performed as shown in Fig. A-5. The red-shifted IQE responses are clearly observed in the short-wavelength range while increasing the NL thicknesses. To combine the results of optical absorption and IQE response, it demonstrates the Si QD thin films using a heavily B-doped GSRO-ML can achieve the bandgap engineering and contribute the significant photo-responsive properties.

In the next works, we will focus on increasing the GSRO-ML periods, optimizing the doping concentration and distribution, and combining the anti-reflection structure to further enhance the QDs' contribution and cell's performances.

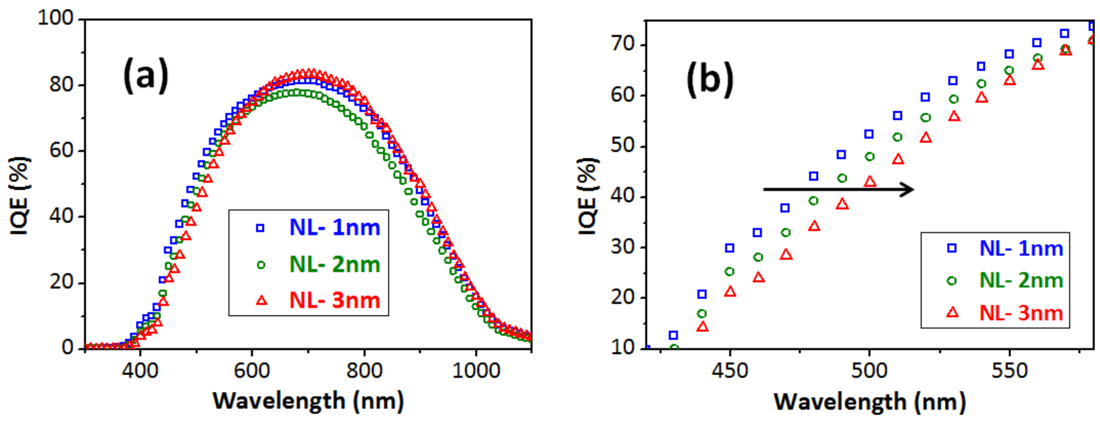

Fig. A-5: (a) Full and (b) magnified internal quantum efficiency spectra of the heavily B-doped Si QD thin films on n-type Si wafers under different nucleation layer thicknesses.

A-2 Heavily P-doped Si QD Thin Films

To obtain the heavily P-doped Si QD thin films, the P atoms diffusion process by post-annealing has been being developed since the P_2O_3 target is hard to be well made. For the heavily P-doped Si QD thin films, the lowly P-doped GSRO-ML thin films are deposited by co-sputtering the lowly P-doped (~1×10^{18} cm^{-3}) Si and pure SiO_2 targets, and then, the as-deposited samples are annealed at 1100℃ for the Si QDs formation. After annealing, the $POCl_3$ films are deposited on the Si QD thin films and annealed at 850℃ by furnace for the P atoms diffusion. Finally, the residual $POCl_3$ films are removed by a wet-etched process. So far, the PV properties of the P-doped Si QD thin films by diffusion process are obviously better than those of the lowly P-doped Si QD thin films. Hence, it represents the P atoms diffusion process is indeed a feasible method for the heavily P-doped Si QD thin films development.

A-3 Summary

The heavily B- and P-doped Si QD thin films have been developed, and the preliminary results reveal the feasible and great potential on PV properties. Next, more enhancements for the Si QD thin films on Si wafers will be studied. In the future works, the heavily B- and P-doped Si QD thin films will be integrated for the high efficiency all Si QD thin film SCs, and we deeply believe the third generation SCs can be achieved by the Si-based tandem SCs integrating the super-high density of Si QDs utilizing our proposed GSRO-ML structure.

References

[1] German Solar Industry Association, *http://www.solarwirtschaft.de/en.html*

[2] EuPD Research, *http://www.eupd-research.com/*

[3] John Wiley & Sons, Inc, *http://as.wiley.com/WileyCDA/Section/index.html*

[4] National Center for Photovoltaics (NCPV), National Renewable Energy Laboratory (NREL), *http://www.nrel.gov/ncpv/*

[5] M. A. Green, "Third generation photovoltaics: ultra-high conversion efficiency at low cost, " *Prog. Photovolt: Res. Appl.* **9**, 123 (2001)

[6] Wikipedia, Sunlight, *http://en.wikipedia.org/wiki/Sunlight*

[7] C. S. Garoufalis and A. D. Zdetsis, "High level ab initio calculations of the optical gap of small silicon quantum dots," *Phys. Rev. Lett.* **87,** 276402 (2001)

[8] S. Mirabella, R. Agosta, G. Franzò, I. Crupi, M. Miritello, R. L. Savio, M. A. D. Stefano, S. D. Marco, F. Simone, and A. Terrasi, "Light absorption in silicon quantum dots embedded in silica," *J. Appl. Phys.* **106,** 103505 (2009)

[9] Z. Kang, Y. Liu, C. H. A. Tsang, D. D. D. Ma, X. Fan, N. B. Wong, and S. T. Lee, "Water-soluble silicon quantum dots with wavelength-tunable photo-luminescence," *Adv. Mater.* **21**, 661 (2009)

[10] G. Conibeer, M. A. Green, R. Corkish, Y. Cho, E. C. Cho, C. W. Jiang, T. Fangsuwannarak, E. Pink, Y. Huang, T. Puzzer, T. Trupke, B. Richards, A. Shalav, and K. L. Lin, "Silicon nanostructures for third generation photovoltaic solar cells," *Thin Solid Films* **511/512,** 654 (2006)

[11] M. Zacharias, J. Heitmann, R. Scholz, U. Kahler, M. Schmidt, and J. Blasing, "Size-controlled highly luminescent silicon nanocrystals: A SiO/SiO_2 superlattice approach," *Appl. Phys. Lett.* **80,** 661 (2002)

[12] M. V. Wolkin, J. Jorne, P. M. Fauchet, G. Allan, and C. Delerue, "Electronic states and luminescence in porous silicon quantum dots: The role of oxygen," *Phys. Rev. Lett.* **82**, 197 (1999)

[13] G. Conibeer, M. A. Green, E. C. Cho, D. König, Y. H. Cho, T. Fangsuwannarak, G. Scardera, E. Pink, Y. Huang, T. Puzzer, S. Huang, D. Song, C. Flynn, S. Park, X. Hao, and D. Mansfield, "Silicon quantum dot nanostructures for tandem photovoltaic cells," *Thin Solid Films* **516,** 6748 (2008)

[14] G. Scardera, T. Puzzer, D. McGrouther, E. Pink, T. Fangsuwannarak, G. Conibeer, and M. A. Green, "Investigating large area fabrication of silicon quantum dots in a nitride matrix for photovoltaic applications," *IEEE Photovoltaic Energy Conversion* **1**, 122 (2006)

[15] D. Song, E. C. Cho, G. Conibeer, C. Flynn, Y. Huang, and M. A. Green, "Structural, electrical and photovoltaic characterization of Si nanocrystals embedded SiC matrix and Si nanocrystals/c-Si heterojunction devices," *Sol. Energy Mater. Sol. Cells* **92**, 474 (2008)

[16] E. C. Cho, S. Park, X. Hao, D. Song, G. Conibeer, S. C. Park, and M. A. Green, "Silicon quantum dot/crystalline silicon solar cells," *Nanotechnology* **19**, 245201 (2008)

[17] C. Feser, J. Lacombe, K. V. Maydell, and C. Agert, "A simulation study towards a new concept for realization of thin film triple junction solar cells based on group IV elements," *Prog. Photovolt: Res. Appl.* **20**, 74 (2012)

[18] X. J. Hao, E. C.Cho, C. Flynn, Y. S. Shen, S. C. Park, G. Conibeer, and M. A. Green, "Synthesis and characterization of boron-doped Si quantum dots for all-Si quantum dot tandem solar cells," *Sol. Energy Mater. Sol. Cells* **93**, 273 (2009)

[19] X. J. Hao, E. C. Cho, G. Scardera, E. Bellet-Amalric, D. Bellet, Y. S. Shen, S. Huang, Y. D. Huang, G. Conibeer, and M. A. Green, "Effects of phosphorus doping on structural and optical properties of silicon nanocrystals in a SiO_2 matrix," *Thin Solid Films* **517,** 5646 (2009)

[20] X. J. Hao, E. C. Cho, G. Scardera, Y. S. Shen, E. Bellet-Amalric, D. Bellet, G. Conibeer, and M. A. Green, "Phosphorus-doped silicon quantum dots for all-silicon quantum dot tandem solar cells," *Sol. Energy Mater. Sol. Cells* **93**, 1524 (2009)

[21] S. H. Hong, J. H. Park, D. H. Shin, C. O. Kim, S. H. Choi, and K. J. Kim, "Doping- and size-dependent photovoltaic properties of p-type Si-quantum-dot heterojunction solar cells: correlation with photoluminescence," *Appl. Phys. Lett.* **97,** 072108 (2010)

[22] G. Conibeer, M. A. Green, D. Konig, I. Perez-Wurfl, S. Huang, X. Hao, D. Di, L. Shi, S. Shrestha, B. Puthen-Veetil, Y. So, B. Zhang, and Z. Wan, "Silicon quantum dot based solar cells: addressing the issues of doping, voltage and current transport," *Prog. Photovolt: Res. Appl.* **19,** 813 (2010)

[23] H. Bartzsch, D. Glöß, P. Frach, M. Gittner, E. Schultheiß, W. Brode, and J. Hartung, "Electrical insulation properties of sputter-deposited SiO_2, Si_3N_4 and Al_2O_3 films at room temperature and 400℃," *Phys. Status Solidi A* **206,** 514 (2009)

[24] B. H. Lai, C. H. Cheng, and G. R. Lin, "Multicolor ITO/SiO_x/p-Si/Al light emitting diodes with improved emission efficiency by small Si quantum dots," *IEEE J. Quantum Electron.* **47**, 698 (2011)

[25] C. H. Cheng, Y. C. Lien, C. L. Wu, and G. R. Lin, "Mutlicolor electro-luminescent Si quantum dots embedded in SiO_x thin film MOSLED with 2.4% external quantum efficiency," *Opt. Express* **21**, 391 (2013)

[26] J. M. Shieh, W. C. Yu, J. Y. Huang, C. K. Wang, B. T. Dai, H. Y. Jhan, C. W. Hsu, H. C. Kuo, F. L. Yang, and C. L. Pan, "Near-infrared silicon quantum dots metal-oxide-semiconductor field-effect transistor photodetector," *Appl. Phys. Lett.* **94**, 241108 (2009)

[27] Y. C. Lien,J. M. Shieh, W. H. Huang, C. H. Tu, C. Wang, C. H. Shen, B. T. Dai, C. L. Pan, C. M. Hu, and F. L. Yang, "Fast programming metal-gate Si quantum dot nonvolatile memory using green nanosecond laser spike annealing," *Appl. Phys. Lett.* **100**, 143501 (2012)

[28] C. W. Jiang, M. A. Green, E. C. Cho, and G. Conibeer, "Resonant tunneling through defects in an insulator: Modeling and solar cell applications," *J. Appl. Phys.* **96,** 5006 (2004)

[29] M. A. Green, E. C. Cho, Y. Cho, Y. Huang, E. Pink, T. Trupke, A. Lin, T. Fangsuwannarak, T. Puzzer, G. Conibeer, and R. Corkish, "All-silicon tandem cells based on "artificial" semiconductor synthesised using silicon quantum dots in a dielectric matrix," *Proceedings of the 20th European Photovoltaic Solar Energy Conference and Exhibition*, pp. 3-6, Barcelona, Spain (2005)

[30] J. W. Luo, P. Stradins, and A. Zunger, "Matrix-embedded silicon quantum dots for photovoltaic applications: A theoretical study of critical factors," *Energy Environ. Sci.* **4,** 2546 (2011)

[31] C. F. Lin, W. T. Tseng, and M. S. Feng, "Formation and characteristics of silicon nanocrystals in plasma-enhanced chemical-vapor-deposited silicon-rich oxide," *J. Appl. Phys.* **87,** 2808 (2000)

[32] T. W. Kim, C. H. Cho, B. H. Kim, and S. J. Park, "Quantum confinement effect in crystalline silicon quantum dots in silicon nitride grown using SiH_4 and NH_3," *Appl. Phys. Lett.* **88,** 123102 (2006)

[33] K. Y. Kuo, S. W. Hsu, P. R. Huang, W. L. Chuang, C. C. Liu, and P. T. Lee, "Optical properties and sub-bandgap formation of nano-crystalline Si quantum dots embedded ZnO thin film," *Opt. Express* **20,** 10470 (2012)

[34] Ü. Özgür, Y. I. Alivov, C. Liu, A. Teke, M. A. Reshnikov, S. Dogan, V. Avrutin, S. J. Cho, and H. Morkoç, “A comprehensive review of ZnO materials and devices,” *J. Appl. Phys.* **98**, 041301 (2005)

[35] Wikipedia, RCA, *http://en.wikipedia.org/wiki/RCA_clean*

[36] Colorado School of Mines, *http://inside.mines.edu/fs_home/cwolden/chen435/clean.htm*

[37] Wikipedia, Ultrasonic Cleaning, *http://en.wikipedia.org/wiki/Ultrasonic_cleaning*

[38] Wikipedia, Reactive Ion Etching, *http://en.wikipedia.org/wiki/Reactive-ion_etching*

[39] Wikimedia Commons, Thermal Evaporation, *https://commons.wikimedia.org/wiki/File:Fig.6_(a)_Vapor_thermal_Evaporation_.JPG*

[40] The Prashant Kamat Laboratory, *University of Notre Dame, http://www3.nd.edu/~kamat lab/facilities_spectroscopy.html*

[41] A. Rastelli, S. Kiravittaya, L. Wang, C. Bauer, and O.G. Schmidt, “Micro-photo-luminescence spectroscopy of hierarchically self-assembled quantum dots,” *Physica E* **32**, 29 (2006)

[42] M. F. Toney, T. C. Huang, S. Brennan, and Z. Rek, “X-ray depth profiling of iron oxide thin film,” *J. Mater. Res.* **3**, 351 (1988)

[43] Arizona State University, *http://www.public.asu.edu/~laserweb/woodbury/classes/chm467/bioanalytical/spectroscopy/absflr.html*

[44] Wikipedia, Atomic Force Microscopy, *http://en.wikipedia.org/wiki/Atomic_force_microscopy*

[45] Wikipedia, Transmission Electron Microscopy, *http://en.wikipedia.org/wiki/Transmission_electron_microscopy*

[46] C. F. Lin, M. Zhang, S. W. Liu, T. L. Chiu, and J. H. Lee, “High photoelectric conversion efficiency of metal phthalocyanine/fullerene heterojunction photovoltaic device,” *Int. J. Mol. Sci.* **12**, 505 (2011)

[47] Q. Cheng, E. Tam, S. Xu, and K. Ostrikov, “Si quantum dots embedded in an amorphous SiC matrix: nanophase control by non-equilibrium plasma hydrogenation,” *Nanoscale* **2,** 594 (2010)

[48] G. Viera, S. Huet, and L. Boufendi “Crystal size and temperature measurements in nanostructured silicon using Raman spectroscopy,” *J. Appl. Phys.* **90,** 4175 (2001)

[49] K. S. Min, K. V. Shcheglov, C. M. Yang, H. A. Atwater, M. L. Brongersma, and A. Polman, “Defect-related versus excitonic visible light emission from ion beam synthesized Si nanocrystals in SiO_2,” *Appl. Phys. Lett.* **69,** 2033 (1996)

[50] X. Wen, L. V. Dao, P. Hannaford, E. C. Cho, Y. H. Cho, and M. A. Green, “Excitation dependence of photoluminescence in silicon quantum dots,” *New J. Phys.* **9,** 337 (2007)

[51] X. Wen, L. V. Dao, and P. Hannaford, “Temperature dependence of photoluminescence in silicon quantum dots,” *J. Phys. D: Appl. Phys.* **40,** 3573 (2007)

[52] M. A. Green, E. C. Cho, Y. Cho, Y. Huang, E. Pink, T. Trupke, A. Lin, T. Fangsuwannarak, T. Puzzer, G. Conibeer, and R. Corkish, “All-silicon tandem cells based on “artificial” semiconductor synthesised using silicon quantumdots in a dielectric matrix,” *Proceedings of the 20th European Photovoltaic Solar Energy Conference and Exhibition*, pp. 3-6, Barcelona, Spain (2005)

[53] C. Meier, A. Gondorf, S. Lüttjohann, A. Lorke, and H. Wiggers, “Silicon nanoparticles: absorption, emission, and the nature of the electronic bandgap,” *J. Appl. Phys.* **101,** 103112 (2007)

[54] N. Yoshida, Y. Shimizu, T. Honda, T. Yokoi, and S. Nonomura, “A study of absorption coefficient spectra in a-Si:H films near the transition from amorphous to crystalline phase measured by resonant photothermal bending spectroscopy,” *J. Non-Cryst. Solids* **354,** 2164 (2008)

[55] V. Osinniy, S. Lysgaard, V. Kolkovsky, V. Pankratov, and A. N. Larsen, “Vertical charge-carrier transport in Si nanocrystal/SiO_2 multilayer structures,” *Nanotechnology* **20,** 195201 (2009)

[56] S. Park, E. Cho, D. Song, G. Conibeer, and M. A. Green, “n-Type silicon quantum dots and p-type crystalline silicon heteroface solar cells,” *Sol. Energy Mater. Sol. Cells* **93,** 684 (2009)

[57] H. Wong and H. Iwai, “On the scaling issues and high-k replacement of ultrathin gate dielectrics for nanoscale MOS transistors,” *Microelectron. Eng.* **83,** 1867 (2006)

[58] H. W. Lau, O. K. Tan, and D. A. Trigg, “Charge injection and tunneling mechanism of solid state reaction silicon nanocrystal film,” *Appl. Phys. Lett.* **89,** 113119 (2006)

[59] I. Perez-Wurfl, X. Hao, A. Gentle, D. H. Kim, G. Conibeer, and M. A. Green, “Si nanocrystal p-i-n diodes fabricated on quartz substrates for third generation solar cell applications,” *Appl. Phys. Lett.* **95,** 153506 (2009)

[60] G. Faraci, S. Gibilisco, P. Russo, A. R. Pennisi, G. Compagnini, S. Battiato, R. Puglisi, and S. L. Rosa, “Si/SiO_2 core shell clusters probed by Raman spectroscopy,” *Eur. Phys. J. B* **46**, 457 (2005)

[61] K. A. Alim, V. A. Fonoberov, and A. A. Balandin, “Origin of the optical phonon frequency shifts in ZnO quantum dots,” *Appl. Phys. Lett.* **86**,053103 (2005)

[62] Q. J. Cheng, S. Xu, and K. Ostrikov, “Structural evolution of nanocrystalline silicon thin films synthesized in high-density, low-temperature reactive plasmas,” *Nanotechnology* **20**, 215606 (2009)

[63] M. Zacharias, J. Blasing, P. Veit, L. Tsybeskov, K. Hirschman, and P. M. Fauchet, “Thermal crystallization of amorphous Si/SiO_2 superlattices,” *Appl. Phys. Lett.* **74**, 2614 (1999)

[64] E. C. Cho, M. A. Green, G. Conibeer, D. Song, Y. H. Cho, G. Scardera, S. Huang, S. Park, X. J. Hao, Y. Huang, and L. V. Dao, “Silicon quantum dots in a dielectric matrix for all-silicon tandem solar cells,” *Adv. OptoElectron.* **2007**, 69578 (2007)

[65] J. B. You, X. W. Zhang, Y. M. Fan, Z. G. Yin, P. F. Cai, and N. F. Chen, “Effect of deposition conditions on optical and electrical properties of ZnO films prepared by pulsed laser deposition,” *Appl. Surf. Sci.* **197-198**, 363 (2002)

[66] D. H. Kim, H. Jeon, G. Kim, S. Hwangboe, V. P. Verma, W. Choi, and M. Jeon, “Comparison of the optical properties of undoped and Ga-doped ZnO thin films deposited using RF magnetron sputtering at room temperature,” *Opt. Commun.* **281**, 2120 (2008)

[67] J. M. Shieh, W. C. Yu, J. Y. Huang, C. K. Wang, B. T. Dai, H. Y. Jhan, C. W. Hsu, H. C. Kuo, F. L. Yang, and C. L. Pan, “Near-infrared silicon quantum dots metal-oxide-semiconductor field-effect transistor photodetector,” *Appl. Phys. Lett.* **94**, 241108 (2009)

[68] Y. G. Wang, S. P. Lau, H. W. Lee, S. F. Yu, B. K. Tay, X. H. Zhang, and H. H. Hng, “Photoluminescence study of ZnO films prepared by thermal oxidation of Zn metallic films in air,” *J. Appl. Phys.* **94**, 354 (2003)

[69] S. Fujihara, Y. Ogawa, and A. Kasai, “Tunable visible photoluminescence from ZnO thin films through Mg-doping and annealing,” *Chem. Mater.* **16**, 2965 (2004)

[70] X. X. Wang, J. G. Zhang, L. Ding, B. W. Cheng, W. K. Ge, J. Z. Yu, and Q. M. Wang, “Origin and evolution of photoluminescence from Si nanocrystals embedded in a SiO_2 matrix,” *Phys. Rev. B* **72**, 195313 (2005)

[71] Y. C. Liu, S. K. Tung, and J. H. Hsieh, "Influence of annealing on optical properties and surface structure of ZnO thin films," *J. Cryst. Growth* **287**, 105 (2006)

[72] Y. P. Chan, J. H. Lin, C. C. Hsu, and W. F. Hsieh, "Near-resonant high order nonlinear absorption of ZnO thin films," *Opt. Express* **16**, 19900 (2008)

[73] Z. Ma, X. Liao, G. Kong, and J. Chu, "Absorption spectra of nanocrystalline silicon embedded in SiO_2 matrix," *Appl. Phys. Lett.* **75**, 1857 (1999)

[74] L. W. Lai and C. T. Lee, "Investigation of optical and electrical properties of ZnO thin films," *Mater. Chem. Phys.* **110**, 393 (2008)

[75] K. B. Sundaram and A. Khan, "Characterization and optimization of zinc oxide films by r.f. magnetron sputtering," *Thin Solid Films* **295,** 87 (1997)

[76] D. Di, H. Xu, I. Perez-Wurfl, M. A. Green, and G. Conibeer, "Improved nanocrystal formation, quantum confinement and carrier transport properties of doped Si quantum dot superlattices for third generation photovoltaics," *Prog. Photovolt.: Res. Appl.* doi: 10.1002/pip.1230 (2011)

[77] J. D. Lee, C. Y. Park, H. S. Kim, J. J. Lee, and Y. G. Choo, "A study of conduction of ZnO film/p-Si heterojunction fabricated by photoinduced electrodeposition under illumination" *J. Phys. D: Appl. Phys.* **43,** 365403 (2010)

[78] S. Mridha and D. Basak, "Ultraviolet and visible photoresponse properties of n-ZnO/p-Si heterojunction," *J. Appl. Phys.* **101,** 083102 (2007)

[79] N. Zebbar, Y. Kheireddine, K. Mokeddem, A. Hafdallah, M. Kechouane, and M. S. Aida, "Structural, optical and electrical properties of n-ZnO/p-Si heterojunction prepared by ultrasonic spray," *Mater. Sci. Semicond. Process* **14,** 229 (2011)

[80] Y. Zhang, J. Xu, B. Lin, Z. Fu, S. Zhong, C. Liu, and Z. Zhang, "Fabrication and electrical characterization of nanocrystalline [ZnO/Si] heterojunctions," *Appl. Surf. Sci.* **252,** 3449 (2006)

[81] Dhananjay, J. Nagaraju, and S. B. Krupanidhi, “Investigations on zinc oxide thin films grown on Si (100) by thermal oxidation,” *Mater. Sci. Eng. B* **137,** 126 (2007)

[82] B. P. Veettil, “Modelling and characterization of carrier transport through nanostructures,” *PhD thesis,* University of New South Wales, School of Photovoltaic and Renewable Energy Engineering (2012)

[83] T. Fangsuwannarak, “Electronic and optical characterisations of silicon quantum dots and its applications in solar cells,” *PhD thesis,* University of New South Wales, Centre of Excellence for Advanced Silicon Photovoltaics and Photonics (2007)

Brief Biography

Kuang-Yang Kuo received his M. S. degree from the Department of Physics, National Cheng Kung University (NCKU) in 2007. During 2008-2013, he is advised by Prof. Po-Tsung Lee and works for his PhD degree in Institute of Electro-Optical Engineering, National Chiao Tung University (NCTU). During this period, he has published many international journals and conferences. His research interests are focused on the novel materials and nanostructures for solar cells application.

International Journal and Letter Articles

1. **Kuang-Yang Kuo**, Pin-Ruei Huang, and Po-Tsung Lee, "Super-high density Si quantum dot thin film utilizing a gradient Si-rich oxide multilayer structure," *Nanotechnology* **24**, 195701 (2013).

   (SCI IF: 3.842; Physics, Applied, Rank Factor: 17/127)

   (Highlighted in *Nanotechweb.org (July 2013)*)

2. **Kuang-Yang Kuo**, Shu-Wei Hsu, Pin-Ruei Huang, Wen-Ling Chuang, Chuan-Cheng Liu, and Po-Tsung Lee, "Optical properties and sub-bandgap formation of nano-crystalline Si quantum dots embedded ZnO thin film," *Opt. Express* **20**, pp. 10470-10475 (2012). (Cited: 5/0)

   (SCI IF: 3.546, Optics, Rank Factor: 4/79)

   (Selected for *Virtual Feature Issue: Quantum Dots for Photonic Applications (QD)* of Optical Materials Express)

3. **Kuang-Yang Kuo**, Shu-Wei Hsu, Wen-Ling Chuang, and Po-Tsung Lee, "Formation of nano-crystalline Si quantum dots embedded in ZnO thin films using a ZnO/Si multilayer structure," *Mater. Lett.* **68**, pp. 463-465 (2012).

   (SCI IF: 2.224, Materials Science, Multidisciplinary, Rank Factor: 55/239)

International Conference Articles

1. **Kuang-Yang Kuo**, Pin-Ruei Haung, You-Jheng Chen, and Po-Tsung Lee, "Super-high Density Si Quantum Dot Thin Film for Photovoltaic Properties Enhancement," Tul3-2, *CLEO-PR&OECC/PS 2013*, Kyoto, Japan (2013).

   (Oral Presentation)

2. **Kuang-Yang Kuo**, Shu-Wei Hsu, Pin-Ruei Huang, Wen-Ling Chuang, Chuan-Cheng Liu, and Po-Tsung Lee, **"**Sub-Bandgap Formation in ZnO Thin Films with Embedded Si Quantum Dots,**"** PYBSV, *E-MRS'12*, Strasbourg, France (2012).

   (Oral Presentation)

3. **Kuang-Yang Kuo**, Shu-Wei Hsu, Wen-Ling Chuang, and Po-Tsung Lee, "Study on the Nano-Crystalline Si Embedded ZnO Thin Films for Solar Cell Application," EH-D-729, *37th IEEE PVSC*, Seattle, Washington, USA (2011).

   (Poster Presentation)

Domestic Conference Articles

1. You-Jheng Chen, Pin-Ruei Haung, **Kuang-Yang Kuo**, and Po-Tsung Lee, "Super-High Density Si Quantum Dot Thin Film Using a Gradient Si-Rich Oxide Multilayer Structure," OI-SA-MD2-(5)-4, *OPTIC'12*, Taipei, Taiwan (2012).

2. Pin-Ruei Huang, Yi-Heng Tsai, **Kuang-Yang Kuo**, and Po-Tsung Lee, "Enhancement on Electro-optical Characteristics of Si Quatum Dots Thin Film Using Lowly-Si-Rich Oxide Barrier Layers," I-SA-IX 6-2, *IPC'11*, Tainan, Taiwan (2011).

3. Chuan-Cheng Liu, Shu-Wei Hsu, **Kuang-Yang Kuo**, and Po-Tsung Lee, "Crystalline and Photo-Responsive Characteristics of Nano-crystalline Si Quantum Dot Embedded ZnO Thin Film," I-FR-IX 5-1, *IPC'11*, Tainan, Taiwan (2011).

4. Wen-Ling Chuang, Shu-Wei Hsu, **Kuang-Yang Kuo**, and Po-Tsung Lee, "Optical and Electrical Characteristics of Nano-Crystalline Si Embedded in the ZnO Matrix," OPT9-P-098, *OPT'10*, Tainan, Taiwan (2010).

5. Shu-Wei Hsu, Wen-Ling Chuang, **Kuang-Yang Kuo**, and Po-Tsung Lee, “Morphologic effect on the formation of nano-crystalline Si embedded in the ZnO matrix,” OPT9-O-15, *OPT’10*, Tainan, Taiwan (2010).

6. **Kung-Yang Kuo**, Tzu-Yueh Chang, and Po-Tsung Lee, “Study of Co-sputtering Si-doped ZnO Thin Films,” IO107, *OPT’09*, Taipei, Taiwan (2009).

7. Hsin-Yu Lee, Yi-Shian Max Lin, **Kuang-Yang Kuo**, Tzu-Yueh Chang, and Po-Tsung Lee, “Post-Annealing Temperature Effect on the Optical and Electrical Properties of the Nano-Structured Si/SiO_2 Multilayer,” Fri-P2-042, *ISSCT’08*, Taipei, Taiwan (2008).